



MARMARA UNIVERSITY

FACULTY OF ENGINEERING



SEMI-ACTIVE CONTROL OF JET ENGINE VIBRATIONS BY SQUEEZE FILM DAMPERS

AYBERK OKAN ACAR, İSMAİL HAKKI ŞENTÜRK

GRADUATION PROJECT REPORT

Department of Mechanical Engineering

Supervisor

Assoc. Prof. Dr. İ. Sina Kuseyri

ISTANBUL, 2025



MARMARA UNIVERSITY

FACULTY OF ENGINEERING



Semi-Active Control of Jet Engine Vibrations by Squeeze Film Dampers

by

Ayberk Okan Acar, İsmail Hakkı Şentürk

July 8, 2025, İstanbul

SUBMITTED TO THE DEPARTMENT OF MECHANICAL ENGINEERING IN
PARTIAL FULFILLMENT OF THE REQUIREMENTS FOR THE DEGREE

OF

BACHELOR OF SCIENCE

AT

MARMARA UNIVERSITY

The author(s) hereby grant(s) to Marmara University permission to reproduce and to distribute publicly paper and electronic copies of this document in whole or in part and declare that the prepared document does not in anyway include copying of previous work on the subject or the use of ideas, concepts, words, or structures regarding the subject without appropriate acknowledgement of the source material.

Signature of Author(s) Ayberk Okan Acar, İsmail Hakkı Şentürk
Department of Mechanical Engineering

Certified By Assoc.Prof. İbrahim Sina Kuseyri
Project Supervisor, Department of Mechanical Engineering

Accepted By Prof. Dr. Bülent Eki
Head of the Department of Mechanical Engineering

ACKNOWLEDGEMENT

First of all, we would like to thank our supervisor Assoc. Prof. Dr.İbrahim Sina Kuseyri for the valuable guidance and advice on preparing this thesis and giving us moral and material support.

July 2025

Ayberk Okan Acar, İsmail Hakkı Şentürk

CONTENTS

1) INTRODUCTION	1
2) THE SQUEEZE FILM DAMPER.....	2
2.1) Literature Review.....	2
2.2) SFD Assembly and Operation.....	7
2.3) Semi Active Control of Engine Vibrations	9
3) THE JET ENGINE	13
4) THEORITICAL BACKGROUND.....	16
4.1) Rotor System.....	16
4.2) Bearings	25
4.2.1) Hydrodynamic Bearings	25
4.2.2) The Squeeze Film Damper.....	27
4.3) Active Sealing Ring System.....	32
5) THE SIMULINK MODEL AND MODEL PARAMETERS.....	35
5.1) Model Parameters	35
5.1.1) Rotor Dimensions	36
5.1.2) Bearing Parameters	40
5.1.3) Seal Ring and Servo Valve Parameters	40
5.2) The Open Loop System.....	41
5.3) Controller Design.....	52
6) SIMULATION RESULTS	54
6.1) Jeffcott Rotor.....	54
6.1.1) Jeffcott Model Open Loop Simulation.....	54
6.1.2) Controller Tuning.....	56
6.1.3) Jeffcott Model Closed Loop Simulation	60
6.2) FE Rotor.....	64
6.2.1) FEM Model Open Loop Simulation	64
6.2.2) FEM Model Closed Loop Simulation.....	70
7) RESULTS AND DISCUSSION	77
8) REFERENCES	79

APPENDIX A : ADDITIONAL DIAGRAMS	81
APPENDIX B : MATLAB CODES	84

LIST OF FIGURES

Figure 2.1 Schematic of SFD used by S.Cooper.[21].....	2
Figure 2.2 Damping change with operation speed (a) Low viscosity (b) high viscosity. [22].....	5
Figure 2.3 SFD test rig Texas A&M Uni., Andres et al. [10].	6
Figure 2.4 Squirrel cage damper configuration used in high-speed rotors. [23].....	7
Figure 2.5 A manufactured version of the schematic.	7
Figure 2.6 (a) Fingering and (b) foamy liquid during high rpm operation in open ended SFDs [11].	8
Figure 2.7 Gaseous and vapor cavitation in SFD operation.	9
Figure 2.8 Schematic of the active SFD, El-Shafei. [7].	10
Figure 2.9 Schematic of a SFD assembly in a jet engine [13].	12
Figure 2.10 Bearing locations and lubrication system in a Rolls Royce Trent engine [13].	12
Figure 3.1 Comparison between working cycles of jet engines and piston engines [13]	13
Figure 3.2 Main bearings and modules for Pratt&Whitney PW4168/4170 variants.[26]	14
Figure 4.1 Single mass Jeffcott rotor [19]	16
Figure 4.2 Jeffcott rotor amplitude plot [19].	18
Figure 4.3 Jeffcott rotor on flexible supports [14].....	18
Figure 4.4 Lumped jet rotor model.....	20
Figure 4.5 Basic FEM building block for rotor simulations [14].	20
Figure 4.6 Film pressure in a hydrodynamic bearing. [20]	25
Figure 4.7 Squeeze film pressure in three configurations. (a) the lubricant is squeezed between two plates. (b) lubricant pressure in open ended bearing with a center groove. (c) lubricant pressure in sealed bearing with a center groove [11].....	26
Figure 4.8 View of journal coordinates.[23].....	27
Figure 4.9 The circular centered orbit.	29
Figure 4.10 Eccentricity dependent coefficients normalized by static coefficients.	32
Figure 4.11 Seal ring position schematic.....	33
Figure 4.12 End pressure in squeeze films (a) open ended, (b) sealed [11].	33
Figure 4.13 FBD of the seal ring	34

Figure 5.1 Pratt&Whitney PW 4000 engine dimensions [27].....	36
Figure 5.2 FE model with 11 elements.....	39
Figure 5.3 Open loop system block diagram.....	41
Figure 5.4 Jeffcott rotor open loop system block diagram.....	42
Figure 5.5 Servo valve and seal dynamics system subsystem.....	43
Figure 5.6 Uncavitated SFD coefficient calculation subsystem.....	44
Figure 5.7. Imbalance with disturbance.	44
Figure 5.8 Decoupled Jeffcott rotor subsystem.....	45
Figure 5.9 Dimensionless journal eccentricity block diagram calculation.....	46
Figure 5.10 Building blocks for the FE model.....	47
Figure 5.11 First node without disk or SFD.	48
Figure 5.12 Internal node with compressor.	49
Figure 5.13 Final node with SFD	50
Figure 5.14 The 11 node HP spool model.	51
Figure 5.15 Controller implemented servo valve seal ring subsystem.....	53
Figure 6.1 Dimensionless journal eccentricity during engine run up.....	54
Figure 6.2 Disk orbit radius during engine run up.	55
Figure 6.3 Mode shapes for SD and LD configurations.....	55
Figure 6.4 The transmitted load during run up.....	56
Figure 6.5 Servo-valve current for various controller gains.....	57
Figure 6.6 Journal and seal position over run up with control.	57
Figure 6.7 Controller disturbance reaction.	58
Figure 6.8 Controller output current for different gains.....	59
Figure 6.9 Closed loop Jeffcott rotor model journal eccentricity.....	60
Figure 6.10 Controlled Jeffcott rotor disk radius	60
Figure 6.11 Servo valve current over run up.	61
Figure 6.12 Controller rotor mode shapes.....	61
Figure 6.13 Transmitted load over run up.	62
Figure 6.14 Journal eccentricity in disturbance test.	62

Figure 6.15 Disk orbit change after disturbance.....	63
Figure 6.16 Controller output current change with disturbance.....	63
Figure 6.17 FE model open loop journal eccentricity for SD and LD modes.....	64
Figure 6.18 Disk orbit difference for SD and LD modes.....	65
Figure 6.19 LD mode shapes.....	65
Figure 6.20 SD mode shapes	66
Figure 6.21 Transmitted force difference in LD an SD modes.	67
Figure 6.22 LRV plot for the SD mode.	68
Figure 6.23 LRV plot for LD mode.	69
Figure 6.24 Controlled FE model rotor journal eccentricity.	70
Figure 6.25 Controlled motor first mode shape.....	71
Figure 6.26 Closed loop compressor disk radius.....	71
Figure 6.27 Controlled rotor second mode shape.....	72
Figure 6.28 Close loop transmitted load at journals.....	72
Figure 6.29 Closed loop system controller output current.	73
Figure 6.30 LRV plot of the closed loop system.	74
Figure 6.31 Sigmoid function for simulating deceleration and steady state.	75
Figure 6.32 Journal position for run up and disturbance.....	75
Figure 6.33 Closed loop disk radius for run up and subsequent disturbance.	76
Figure A.1 Sigmoid function block diagram.	81
Figure A.2 Unbalance force for FE model.	81
Figure A.3 FE model	82
Figure A. 4 Colorized SFD schematic	83

ABBREVIATIONS

3D	: Three Dimensional
2D	: Two Dimensional
CCO	: Circular Centered Orbit
CO	: Centered Orbit
DOF	: Degree of Freedom
SFD	: Squeeze Film Damper
FEM	: Finite Element Method
FE	: Finite Element
HP	: High Pressure
LD	: Long Damper
LP	: Low Pressure
LRV	: Lateral Rotor Vibrations,
PI	: Proportional-Integral
PID	: Proportional-Integral-Derivative
SAE	: Society of Automobile Engineers
SD	: Short Damper

SYMBOLS

a	: Seal position
A_r	: Radial Acceleration
A_j	: Journal Surface Area
c	: Clearance
C^*	: Zero Amplitude SFD Damping Coefficient
C_s	: Seal Ring Damping Coefficient
$C_{rr}, C_{rt}, C_{tt}, C_{tr}$: r-t Damping Coefficients
$C_{xx}, C_{xy}, C_{yx}, C_{yy}$: x-y Damping Coefficients
D	: SFD Diameter
$D_{shaft,o}, D_{shaft,I}$: Hollow Shaft Inner and Outer Diameter
$D_{disk,c}, D_{disk,t}$: Compressor and Turbine disk Diameter
ϵ	: Dimensionless Journal Eccentricity
e	: Disk Center of Mass Eccentricity
e_j	: Journal Eccentricity
E_i	: Element Young Modulus
F_r, F_t	: r-t Fluid Film Forces
F_x, F_y	: x-y Fluid Film Force
$f_{x(t)}, f_{y(t)}$: x-y Imbalance Force
F_l	: Lubricant Pressure Force on the Seal Ring
F_p	: Servo Valve Pressure Force on the Seal Ring
G	: Gyroscopic Coefficient, ωI_P
$[G]_i^{(s)}$: Gyroscopic Matrix

K^*	: Stiffness Matrix Factor $2E_i I_i / L_i^3$
K_θ	: Rotational Stiffness
K_1, K_2, K_3	: Stiffness Matrix Common Elements
K_{cp}, K_{ci}	: Controller Gains
K_g	: Geometric Bearing Ratio
K_i	: Servo Valve Gain
$[K]_l$: Stiffness Matrix
L	: Fluid Film Length
L_{shaft}	: Shaft Length
L_i	: Element Length
λ	: Dimensionless Seal Position
h	: Fluid Film
i	: Servo Valve Current
I	: Area Moment of Inertia
I_{pi}	: Element Polar Inertia
I_{ti}	: Element Transverse Inertia
m_1, m_2, m_3	: Lumped Masses for Jeffcott Rotor
$m_{d,c}, m_{d,t}$: Compressor and Turbine Disk Mass
M^*	: Zero amplitude Fluid Inertia
$[M]_{i1}$: Element Mass Matrix
$M(s)$: Element Mass
m_s	: Seal Ring Mass
$M_{rr}, M_{rt}, M_{tt}, M_{tr}$: r-t Fluid Inertia Coefficients
$M_{xx}, M_{xy}, M_{yx}, M_{yy}$: x-y Fluid Inertia Coefficients

μ	: Dynamic Viscosity
t	: Time Step
$t_{\text{disk,t}}, t_{\text{disk,c}}$: Disk Thickness
θ_{xi}, θ_{yi}	: Gyroscopic coordinates
p	: Servo Valve Pressure
ρ	: Lubricant Density
ρ_{steel}	: Material Density
Re_s	: Fluid Film Reynolds Coefficient
$\{q\}$: Generalized Coordinates
ω	: Spin Speed
ω_p	: Servo Valve Natural Frequency
V_t	: Tangential Speed
x_i, y_i	: Generalized Node Coordinates
ζ_p	: Servo Valve Damping Coefficient

ABSTRACT

Semi-Active Control of Jet Engine Vibrations by Squeeze Film Dampers

Passive control of rotor vibrations in aircraft rotors has been successfully done by implementing squeeze film dampers to traditional roller and thrust bearings for the last 50 years. Recently, trends have gone into designing smaller bearings that enable enough vibration attenuation at higher speeds enabling reduced rotor weight. However, a subject that has seen not much attention is the semi active control of damping in squeeze film dampers by means of actuated sealing pistons. To test the applicability of semi active control by PI control, we built FE and Jeffcott rotor models based on the HP spool of the Pratt&Whitney PW4168/4170 jet engine using MATLAB Simulink. PI controller gains are tuned based on Jeffcott rotor model simulation outcomes and applied to the more complex FE model that is supported by the same semi-active squeeze film dampers. The engine run up simulations and disturbance applied at a steady state orbit show that compared to its passive counterparts the semi-active SFD can attenuate vibration at the critical speed and lower force transmissibility away from critical speeds.

1) INTRODUCTION

The high-performance modern rotors of today are the result of 150 years of hand in hand work between the scientific community and various industries such as airplane, automotive and energy. During the last century the requirements from power transmission elements have increased in areas such as energy production, speed, reliability, lifetime, and safety. Therefore, the design step of modern rotating machinery compared to its past counterpart plays a more critical role. For this reason, research and development of new methods to monitor and combat failure causing phenomena has great importance. The vast subject matter however limits a solution to be applied to all range of applications due to size, speed, and risk assessment.

One of the main research areas regarding failure is the control of rotor vibrations by passive or active elements. An important advancement made for gas turbines is the passive squeeze film damper that has been successfully implemented to aircraft engines since the 1970s [21]. The SFD presents itself as a modification done to the ball bearing. The squeeze film lays between the centering spring held roller bearing housing and an outer ring. Benefits of SFDs in critical machinery include lower vibration amplitude during operation and at critical speeds, lower transmissibility to the fatigue prone structural components, simple alignment, and lower power loss through friction [1]-[12]. These advantages interest both the scientific community and the industry. They are uncommon compared to roller and journal bearings and are generally utilized as a last resort for problematic machinery.

The semi-active SFD on the other hand has not seen that much interest. In this report the case of semi-active vibration control for aircraft engines using an active squeeze film damper that houses movable seal rings is examined. The semi-active bearing utilizes both the ‘short’ and ‘long’ damper modes to combat vibration at critical speeds compared to passive SFDs that are designed for sealed or open-ended bearing end condition. The overall aim of the semi-active SFD is to optimize unbalance response, vibration amplitude, transmissibility, and disturbance rejection during operation.

2) THE SQUEEZE FILM DAMPER

2.1) Literature Review

SFDs are critical elements in vibration attenuation for aircraft engines. For this reason, over the last five decades a vast literature has been formed by researchers who examined various aspects of their behavior. Their development has coincided with aircraft industries need of a means of rotor vibration control. Traditional aircraft engines (internal combustion) only employed radial roller and thrust bearings to support the rotor load [21]. In the first jet engines of Hans von Ohain and Frank Whittle, the vibration caused by higher speed of the rotor due to lack of damping in roller bearings was identified as an issue. After the war U.S Army, Royal Airforce and commercial engine developers were interested in methods to combat this problem.

In 1963, a technical report discussing experiments on effects of oil films for the control of rotor vibrations was published by a Rolls Royce engineer named S.Cooper. While testing new methods to combat rotor instabilities on the jet engine, Cooper realized that even the light touch of hand was enough to limit the amplitude of vibration to an acceptable degree [15],[21]. Considering this, he developed a hybrid bearing scheme that utilized a thin lubricant film (larger film thickness compared to a hydrodynamic bearings) placed between the whirling ball bearing outer race and a metallic shell to add damping to ball bearings as shown in Figure 2.1. He named the new bearing squeeze film damper.

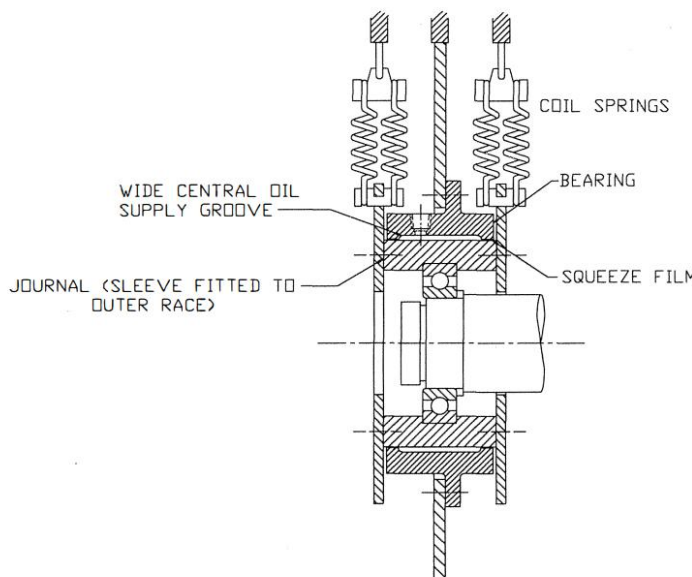


Figure 2.1 Schematic of SFD used by S.Cooper.[21].

The benefits of this novel approach was quickly realized and in the following fifteen years various models for explaining SFD behavior were developed. Initial model by Cooper explained squeeze film damping by using the classical Reynolds equation. Thomsen et al. (1974) [1] investigated the range of damping in a simple SFD by varying unbalance, radial clearance and viscosity. Using a maximum eccentricity of 25% of the clearance, they found no significant relation between imbalance force and damping. Additionally, they found a correlation between classical lubrication-based theory and their experiment. However, the values predicted by the theory were off at some clearances which indicated an unknown nonlinearity.

John M. Vance et al. (1975) [2] examined Reynolds equation-based long bearing approximations in SFDs experimentally for circular centered orbits. They found that the sealed end condition was better explained by the long bearing approximation. However, the values predicted by theory were only accurate for central orbit. Even then the measured peak magnitude disagreed with the theory indicating the CCO based Reynolds equation has some additional mechanism.

Edgar J. Gunter et al. (1975) [3] investigated the steady state response of the SFD using short bearing approximation and developed force coefficients based on the small circular whirl for cavitating and the uncavitated dampers. The cavitation was implemented by using the pi-film theory which proposed that the cavitating film will rupture under tension. The inclusion of cavitation in the equations was a step forward, because at actual supply pressures used in airplane motors, the pressure drop at high clearance orbits was enough for cavitation to occur. Their three-mass flexible rotor simulation (Jeffcott rotor) showed that proper SFDs can improve stability and unbalance response. Two years later (1977) [4], examining the SFD design for aircraft engines, they identified that when eccentricity passes half of the bearing clearance, the damping coefficient generated by the film will be high enough to increase transmissibility. Experiments with intentionally bad designed SFD showed a jump phenomenon at 16500 rpm, indicating a design limit in maximum eccentricity for predictable behavior.

Classical lubrication theory-based models relied on simplifications that neglected groove geometry, fluid inertia, and air ingestion and the development of actual SFDs for airplanes relied on heavily experiments [21]. Eventually, the feedback from industry and subsequent experiments showed that many SFDs worked outside the recommended regime yet stayed operational. This

resulted in a need for a better model. John M. Vance et al. (1987) [5] reviewed recent experiments on CCO SFDs and built a test rig that would enable examination of fluid forces independent of the rotor dynamics. They concluded with increasing Reynolds' number ($Re>1$), fluid inertia effects became significant, causing an added mass effect. Furthermore, they added a set of linearized inertia equations to the previously constructed model in 1975.

John M. Vance et al. (1987) [6] later derived a new set linearized force coefficients for short and long damper modes that accounted for inertia effects for the first time in literature. The derivation considered small amplitude motions about a static eccentricity from the bearing center. The relation between journal eccentricity and inertia effects were well predicted by the model for $Re<20$ and static eccentricity up to 60% of clearance. Further examinations showed that the actual coefficients were between the values predicted by pi-film and uncavitated damper models ([23]). However, the experiments showed the pi-film theory over predicted the nonlinearity of the SFD. With CCO and static eccentricity coefficients explained, research effort moved on to quantifying groove geometry, supply pressure, cavitation, air ingestion, seal types, squirrel cage, centering spring, and other possible parameters affecting SFD behavior. The development of SFD up to 1995 is summarized by Zeidan et al (1996) [21].

After 2000s SFD research showed great advancement. Diaz et al (2001) [10] proposed a bubbly mixture model based on modified Reynolds equation that explains air ingestion and air entrapment shown by fast operating SFDs. Their approach was based on the success of the modified Reynold model had in journal bearings. During experiments they supplied a circular orbiting SFD with controlled lubricant/air mixture. The measured damping drop in low bubbly lubricant supply was well predicted by the model. As a result, the modified theory replaced the previous cavitation model. However, as the modified model based CFD solutions take a considerable amount of time, popular rotordynamic software's such as DYROBES still continue to use pi-film based linearized equations. [25]

Quantifying the relation between damping and temperature is important due to viscosity drop with increasing temperature. In steady state conditions, the average film temperature is found by measuring the supplied and discharged lubricant temperatures [18]. H. Zhou et. al. (2023) [22], examined variation of temperature in bubbly liquid model using a 3D CFD model. They found that

vibration energy absorption during operation increased the lubricant temperature yielding a lower vaporization pressure. This lowered vaporization pressure and pulled cavitation forward. However, as some of the heat energy was transferred to cavitation at power pressure zones the temperature rise slowed. Comparing low viscosity and high viscosity lubricants they found that the higher vaporization pressure of the latter yielded a higher temperature profile, increasing the variability of damping of the film. Overall, the damping reduced by 1.4% for the low viscosity oil, and 15.9% for the high viscosity oil as shown in Figure 2.2 below.

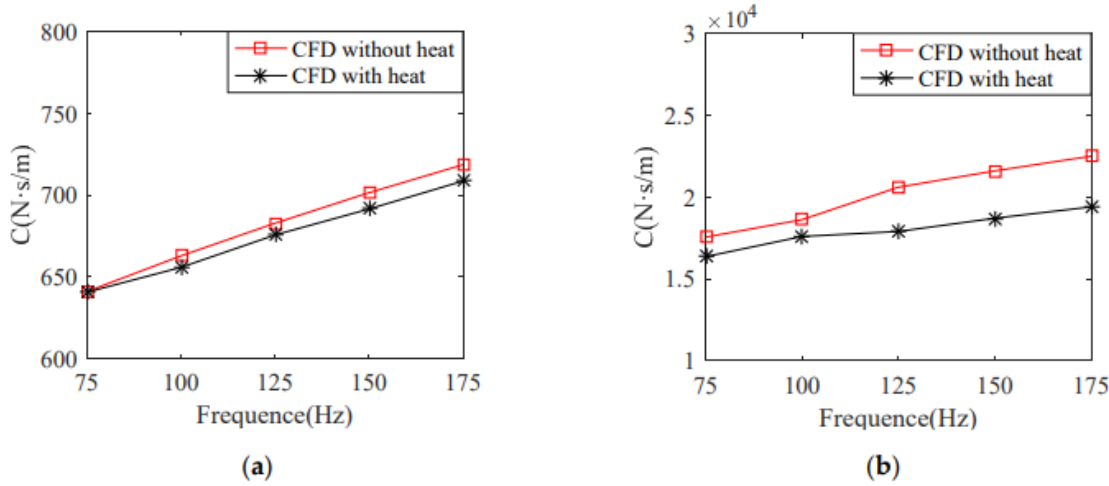


Figure 2.2 Damping change with operation speed (a) Low viscosity (b) high viscosity. [22].

In 2008, with the support of the airplane industry, an SFD laboratory was built in Texas A&M University to examine geometrical properties of SFDs. Two presentations by San Andres et. al. (2016) [11],[12] summarize the results of 8 years of experimentation. In conclusion they report:

- a) SFDs do not have a centering stiffness as opposed to journal bearings.
- b) Damping and inertia coefficients are nearly isotropic
- c) For most whirl types cross coupling coefficients are negligible.
- d) SFDs generate damping force coefficients that nearly remain constant as the amplitude of journal motion increases to 70% percent of the clearance. Unlike the simplified model suggests the experimental force coefficients generated by SFD do not show a strong nonlinearity with the static eccentricity or whirl amplitude. Additionally, the shape of the whirl motion has little effect on force generation, experiments show SFDs being linear elements.

- e) Deep groove configuration results in large added mass coefficients. Contrary to popular explanations grooves do not isolate the adjacent film lands nor ensure uniform flow.
- f) The lubricant supply level is more important than the number of supply holes, as 1,2-, and 3-hole assemblies show negligible difference.
- g) A sealed damper produces more significant damping.

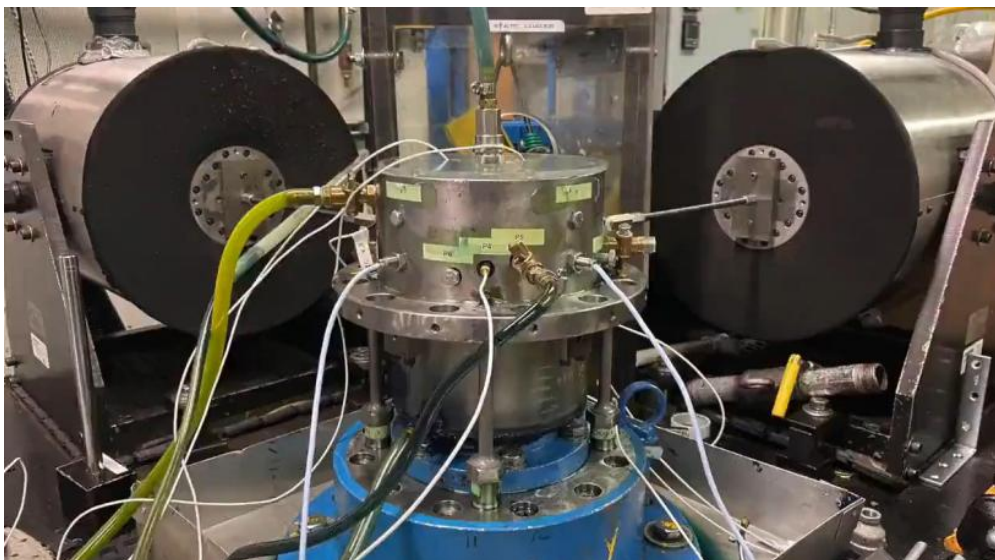


Figure 2.3 SFD test rig Texas A&M Uni., Andres et al. [10].

2.2) SFD Assembly and Operation

San Andres (2010) [23] reports technical issues and industry practices used in SFD design. Practical SFDs are supported with squirrel cages that both prevent the journal rotation and apply a centering stiffness. Manufacturers in U.S. incorporate squirrel cages as shown in the schematic in Figure 2.4; an actual version is shown in Figure 2.5 [11].

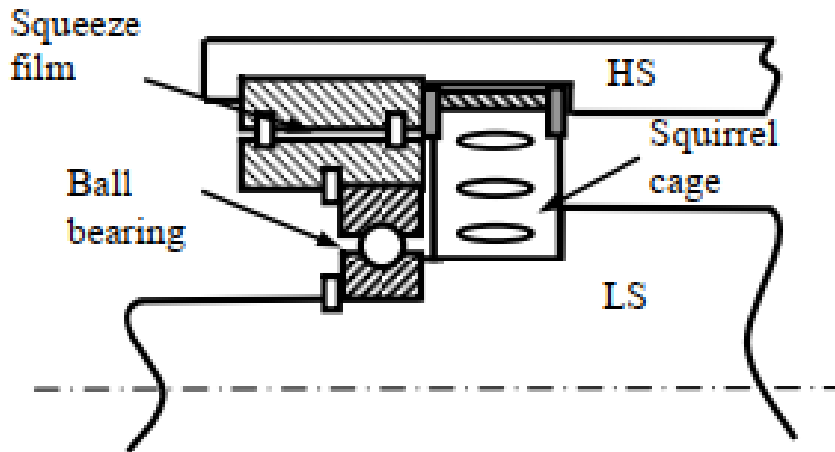


Figure 2.4 Squirrel cage damper configuration used in high-speed rotors. [23].



Figure 2.5 A manufactured version of the schematic.

The damping and inertia forces generated by the SFD predicted by the models, change during operation. This causes the imbalance response characteristic, rotor critical speed, and stability to vary. For this reason, aside from the CFD+FEM approach, there are two methods for analyzing rotor-SFD assembly parameters. The first method examines the imbalance response obtained from the CCO model, and the second method examines the rotor critical speed using coefficients derived from a static equilibrium. The CCO and static equilibrium model linearized force coefficients are derived in [6]. Use of inertia coefficients with damping is important because experiments show that even though the total mass of the fluid in the clearance is insignificant (i.e. a few grams), at high speeds it can generate the same magnitude of force as the rotor mass ([23]).

The reason behind the increased inertia effects compared to journal bearings is not just the higher operating speeds. The clearance in SFD is an order of magnitude larger compared to hydrodynamic bearings (0.1mm-0.3 mm). An unwanted outcome of this is air ingestion, and cavitation to be more pronounced in open ended SFDs. In case of air ingestion, the increased whirl amplitude at critical speed creates a larger suction force after film rupture causing ambient air to fill the gap [11],[23]. The repetition of this during high amplitude orbits forms low pressure zones (see Figure 2.6). In regions where pressure gets lower than the vapor and dissolved gas pressures of the lubricant, cavitation occurs. As the lubricant is already air ingested, the outcoming liquid shows a foamy structure. In sealed dampers the air ingestion does not occur, and cavitation tends to be rarer.

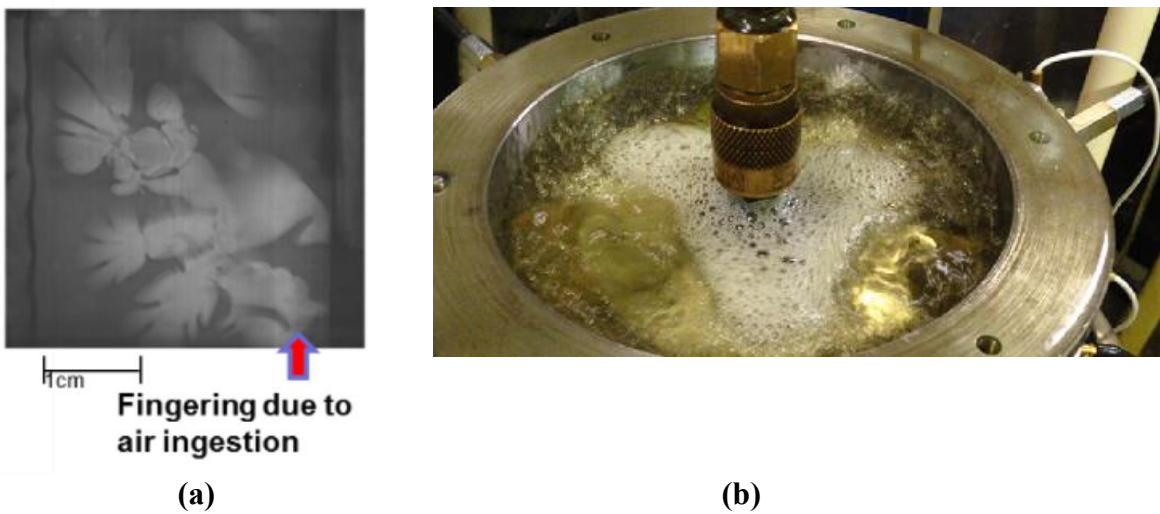


Figure 2.6 (a) Fingering and (b) foamy liquid during high rpm operation in open ended SFDs [11].

Experiments on SFDs generally are usually performed between 0 to 250 Hz (12000 rpm). As the rotor speeds up, the magnitude of the negative pressure decreases due to whirling amplitude. The vapor pressure for dissolved air and lubricant itself are different. Therefore, cavitation of dissolved gas in the lubricant and of the lubricant begin at different stages as shown in schema below.

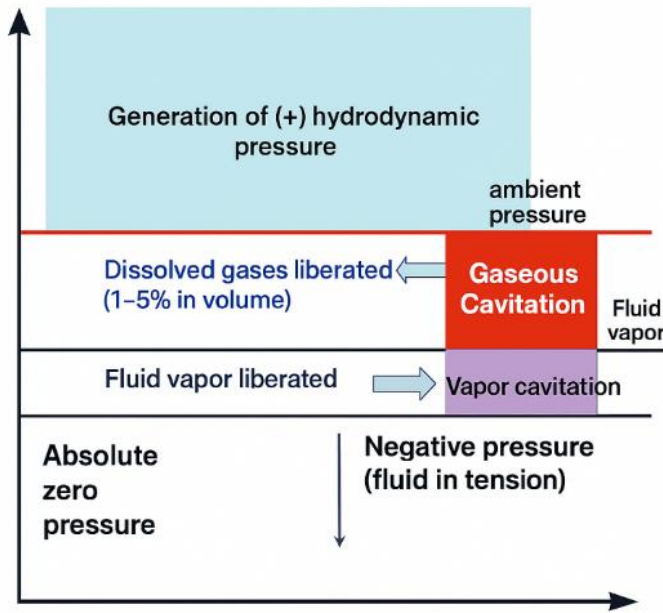


Figure 2.7 Gaseous and vapor cavitation in SFD operation.

For most journal designs, normal operation conditions do not produce enough pressure drop for vapor cavitation to occur. Air entrapment on the other hand is a common issue for open ended SFDs.

2.3) Semi Active Control of Engine Vibrations

SFD are passive vibration control elements. However, their short and long damper behavior depending on the sealing condition made the idea of controlling rotor vibrations through an active SFD logical. This concept was first examined by Burrows et al (1984). A. El-Shafei, after working on SFD modelling in his master's thesis (1988), published a series of papers that examined Jeffcott rotor-SFD model for CCO in short and long dampers. Realizing active control was possible, in 1991 [7] he published an active bearing model incorporating long and short damper into a Jeffcott rotor. Manually controlled experiments showed a lowered amplitude vibration at critical speed

when long damper configuration was used. The SFD used by El-Shafei is shown in Figure 2.8. Continuing to work on the concept, in same year (1991) El-Shafei patented a ‘Hybrid Squeeze Damper’ for active control of rotor vibrations where he described a pressure pump movable seal ring assembly (U.S. Patent 5,058,452).

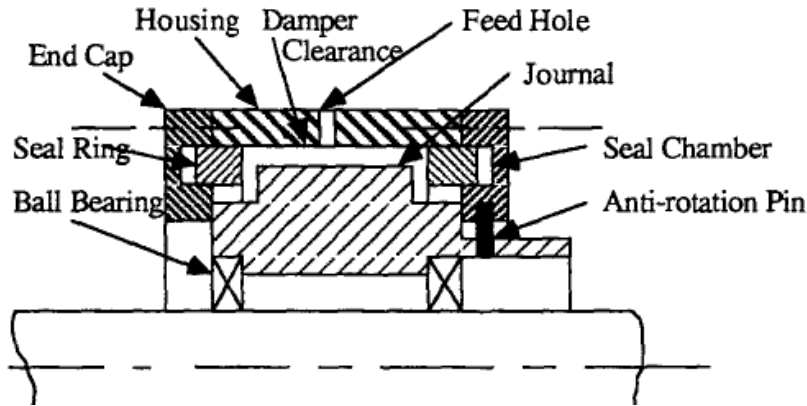


Figure 2.8 Schematic of the active SFD, El-Shafei. [7].

The subject became a long-term project at Cairo University. A five-year project report starting from 1992 is given by El-Shafei et al. (1997) [9]. Over the years they tested 7 controller schemes starting from the basic on-off controller. El-Shafei et al. (1995) [8], presented a concept experiment rig with governing equations. The model neglected cavitation and was based on CCO for simplification. Arguing that the rotor critical speeds would be known beforehand, they first tested an on-off controller for control. The damping change on short to long damper mode was modelled using a damper finiteness measure defined as the ratio of seal position and static clearance. The closed-loop simulations showed a great reduction in vibration amplitude at critical speeds when the long damper mode was used.

In his master’s thesis J.P Hathout (1995) [9] using the groundwork laid by the on-off controller design, investigated the possibility of applying PI, PI-GS, LQR, and MRAC controllers to the HSFD. The finite damper model allowed damping coefficients at changing seal position to be found. For the simplified rotor bearing system, active control improved vibration attenuation and transmissibility during start up and coast down. The PI controller was designed for journal eccentricity feedback. Control parameters were selected so that the system would avoid long damper mode at normal operation and short damper mode at critical speeds.

Hathout showed the PI controller was more adaptable compared to the on-off controller. However, a chattering effect was identified during the transient run-up and disturbance rejection. Noting this, a gain scheduling scheme was added which avoided chattering. Hathout's thesis provided theoretical basis for later experiments conducted at Cairo University. The result lists advanced control methods to better fit HSFD as during experiments P and PI controllers exhibited chattering. The comparison between control algorithms is given in Table 2.1.

Table 2.1 Comparison of various controllers used in HSFD.

	On/Off	P	PI	GS-PI	MRAC
Qualitative Review	Follows objectives	Chattering Saturation	Chattering Saturation	Well behaved Saturation	Well behaved Reference based
Robustness	Preselected	Gain Sensitive	Gain Sensitive	Good	Sensitive due to reference basing
Disturbance Rejection	Unable to reject	Possible but chatters	Possible but chatters	Excellent	Excellent
Sudden Unbalance	Unable		Good	Good	Good
Controller Effort		High	High	Good	Good

In summary, SFDs enable safe passage through critical speeds during start-up and coast down, decreasing fatigue conditions to occur. They are placed in line with other bearings to optimize damping to a level where it would not be too stiff or too light. For this reason, they are designed on a case basis rather than being mass-produced. Recent trends in aircraft design move toward more compact rotors with reduced weight (especially in combat jets). Thus, SFD size is regarded as bottleneck for advancement [10],[11],[18]. However, the benefit of active control for reducing rotor vibrations is also shown in [7]-[9]. Therefore, a localized application of semi active or active bearings can be recommended for increasing redundancy.

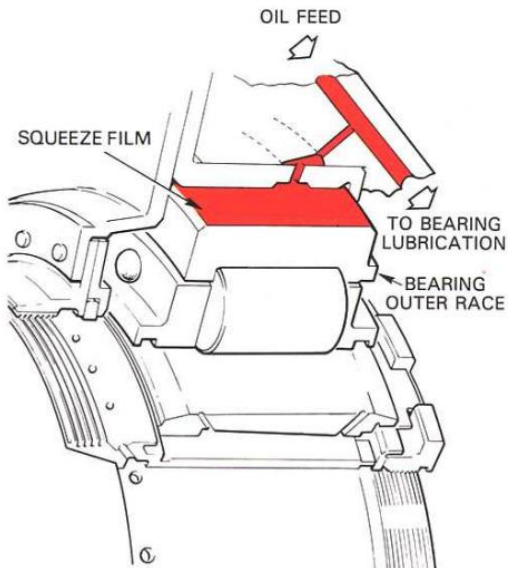


Figure 2.9 Schematic of a SFD assembly in a jet engine [13].

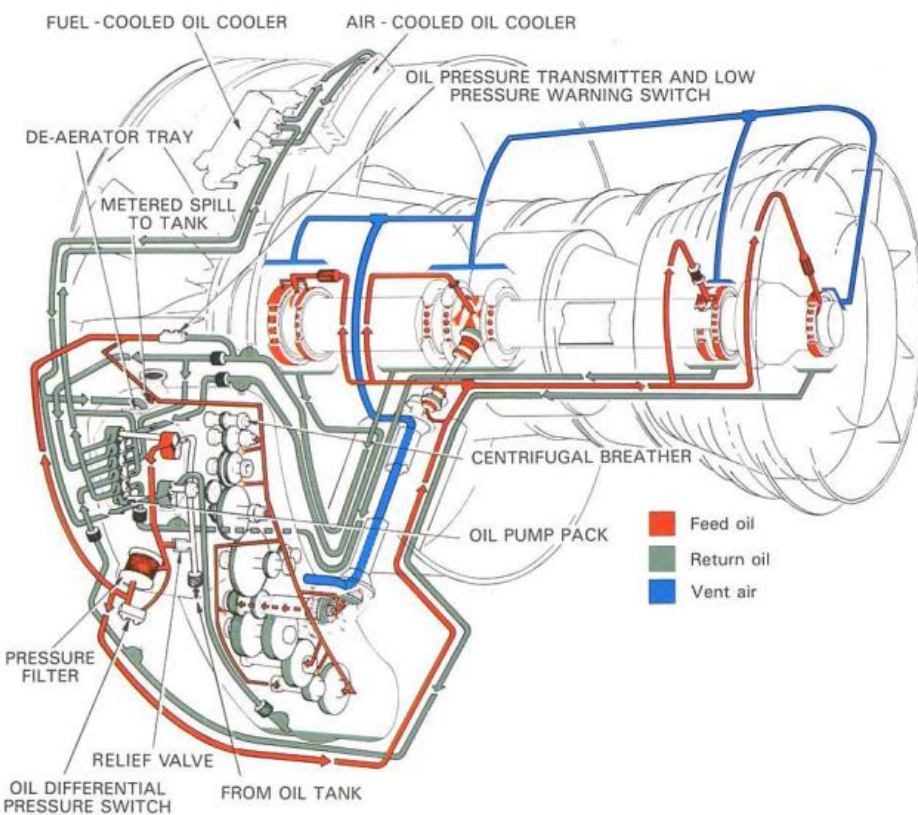


Figure 2.10 Bearing locations and lubrication system in a Rolls Royce Trent engine [13].

3) THE JET ENGINE

Jet engines that are used in airplanes are composed of various intertwined subsystems optimized to achieve safety, efficiency and sustainability while generating the thrust force required during flight. Due to size, maneuverability, and operation requirements in commercial and military aircraft, there are many different engine configurations. However, the fundamental heat engine principle is the same. In a jet engine intake, compression, ignition, and exhaust cycles operate in parallel enabling continuous thrust generation as shown in the Figure 3.1 below.

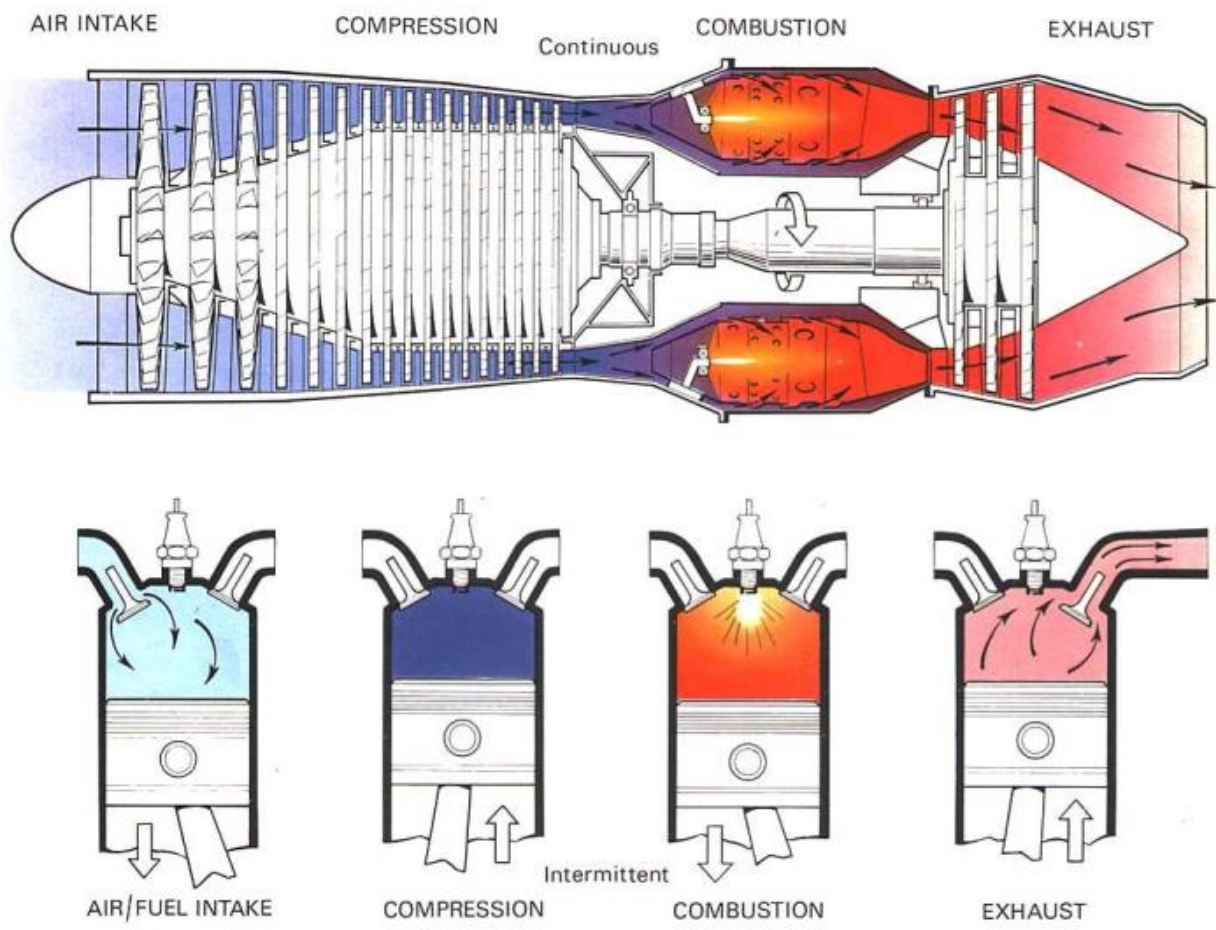


Figure 3.1 Comparison between working cycles of jet engines and piston engines [13]

In the intake cycle, a regulating fan or duct leads the atmospheric air into the engine. The compressor section that is made of several stages of blades (the compression ratio is between 1 and 2 on each subsequent stage) then compresses, heats, and regulates the atmospheric air. The compressed air enters the combustion chamber where its volume is increased by chemical energy

of the fuel. After the expansion and before the exhaust, a small series stages that make up the turbine further expands and regulates exiting air flow. The volume change between the incoming and the outgoing air generates the required thrust force [13].

The bearing load on a jet rotor is mainly composed of compressor blades, turbine blades, and the connecting hollow shaft which can have a single or a multi spool configuration. Generally, the compressor section houses multiple stages of blades that get smaller in each stage and turbine section houses a smaller number of stages of blades that get larger in each stage [13] This overall rotor architecture is designed so that the airflow, material limits (temperature, stress), and thrust is optimized. The figure below shows sections and bearing locations of an Airbus A330 engine.

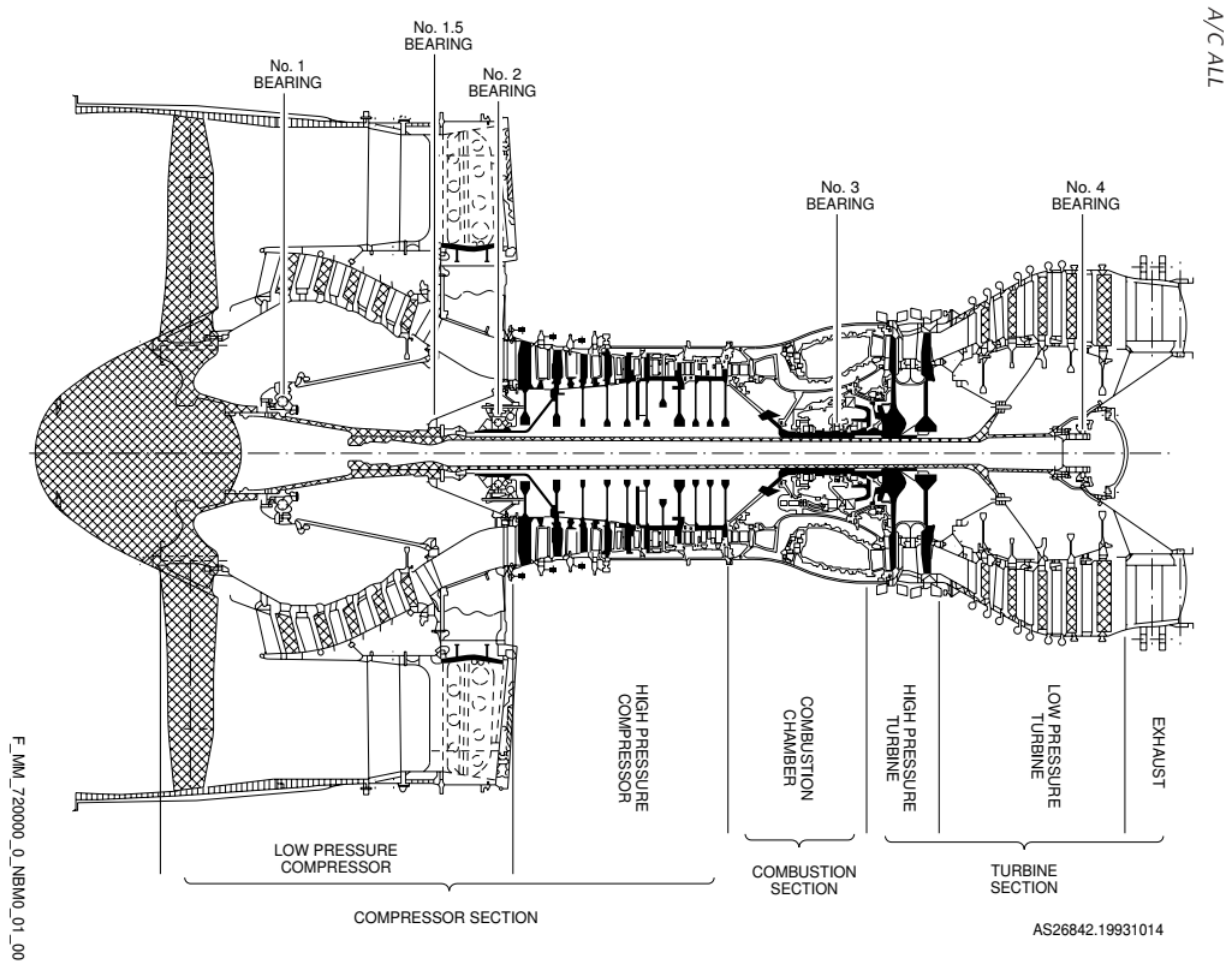


Figure 3.2 Main bearings and modules for Pratt&Whitney PW4168/4170 variants.[26]

In the figure the blacked section signifies that the rotor is composed of 2 concentric spools that can spin at different speeds. Furthermore, it is shown that each spool is carried by different sets of bearings. Namely, the LP section is carried by bearings 1, 1.5, and 4; the HP section is carried by bearings 2 and 3. The critical section is of the rotor where most of the load is present is the HP section [13]. Therefore, for these types of engines bearing 2, bearing 3, or both bearing 2 and bearing 3 can be selected as SFDs to attenuate the excessive vibration using fluid film damping [13].

In this project we used semi-active bearings at both locations on a rotor model based on the Pratt&Whitney PW4168/4170, HP spool. However, considering increased bearing size for the semi-active SFD compared to passive configurations, placing it only at the bearing 2 location can be a better design practice, due to combustion chamber laying in parallel with the bearing 3.

Material selection in jet engines is done considering the strength to density ratios and fatigue [13]. The blades on the HP section are imposed with harsher operating conditions. For this reason, HP compressor stages are composed of titanium alloy blades and HP turbine stages are composed of nickel allow blades. Since the overall blade dimensions, material and weights are not disclosed to the public, we followed an estimation route (see Chap.5). The shaft is hollow and made of high strength steel ($\sim 8 \text{ g/cm}^3$). On Figure 3.2, for the HP spool, 10 compressor stages and 2 turbine stages are shown. Compared to HP compressor blades, the HP turbine blades are both denser ($\sim 4.4 \text{ g/cm}^3$ vs $\sim 8.5 \text{ g/cm}^3$) and are considerably larger. [25],[26]. Therefore, the disk mass for the turbine must be greater than the compressor disk mass. The center of mass lies between bearing 2 and bearing 3 (near bearing 3). For this reason, modelling the compressor stages as a lumped mass between bearings (closer to bearing 3) and turbine as a overhung disk is a simplified but realistic approach.

4) THEORITICAL BACKGROUND

4.1) Rotor System

Rotors are standard power transmission elements that are used throughout the mechanical engineering discipline. A rotor is defined as the combination of the shaft and all the components that are mounted on it including the disk, coupling, blades, fan, gears, etc. These components affect the behavior of the shaft in 3D space. Rotor vibrations are generally classified as lateral and torsional rotor vibrations. Lateral rotor vibrations occur in rotors spin axis as deflection and torsional rotor vibrations occur as relative angular movement on rotors centerline. For systems with a single rotor generally only the LRV is a concern [16].

Historically, rotors that were powered by the steam engines in the 19th century operated below the first critical speed. Steady operation beyond the first critical speed was deemed impossible by W. A. Rankine and his refusal was widely accepted by engineers until DeLaval demonstrated this notion was not correct in 1895[2] experimentally. In 1919 Jeffcott introduced the first correct lateral rotor vibration model to showcase how a rotor behaves beyond its first critical speed. The rotor modelled by Jeffcott is named after him. It consists of a single disk mounted on a symmetric shaft supported by simple supports. The mass of the disk and the shaft are assumed to be lumped on the shaft center. The imbalance of the disk causes an outward force due to centrifugal effect. Therefore, the model describes how the disk center held by shaft stiffness whirls on a plane perpendicular to the shaft axis. The Jeffcott rotor is shown in Figure 4.1.

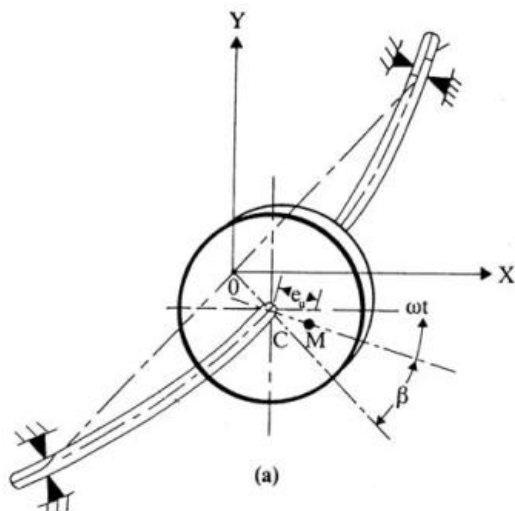


Figure 4.1 Single mass Jeffcott rotor [19]

The unbalance force $M\omega^2$ is a radially outward force. Using the angle ωt the unbalance force can be broken into two components lying on x and y axes. The equation of motion for the disk is:

$$M\ddot{x} + C\dot{x} + Kx = M\omega^2 \cos(\omega t) \quad (4.1)$$

$$M\ddot{y} + C\dot{y} + Ky = M\omega^2 \sin(\omega t) \quad (4.2)$$

Where M is equivalent mass, C is damping applied to the shaft center, and K is shafts stiffness. The system of equations can be written in matrix form as:

$$[M]\{\ddot{q}\} + [C]\{\dot{q}\} + [K]\{q\} = \{f(t)\} \quad (4.3)$$

The equivalent mass at disk eccentricity is usually taken as $M = 0.5m_{shaft} + m_{disk}$ [19]. The Jeffcott rotor is a simply supported beam with a force (concentrated mass) applied at the middle. Therefore, the shaft stiffness can be written using the well-known deflection formulas [18].

$$y_{max} = \frac{FL^3}{48EI} \quad (4.4)$$

Where E is Young's modulus of elasticity, I is shafts moment of inertia, and L is shafts length. Assuming linearity on small deflections, the Hooke's law state $F = k\delta$.

$$K = \frac{48EI}{L^3} \quad (4.5)$$

The rotor amplitude for a spin speed is given by the following equation:

$$A(\omega) = \frac{M\omega^2}{\sqrt{(K-M\omega^2)+(C\omega)^2}} \quad (4.6)$$

In contrast to a standard mass spring damper actuated by a sinusoidal force ($F\sin(\omega t)$), rotating mass system has a $M\omega^2$ term on the numerator. This difference shows itself as a nonzero steady state amplitude like an asymptote where the disk position reaches after the critical speed. The figure below shows an exemplary bode plot for the Jeffcott rotor amplitude [19].

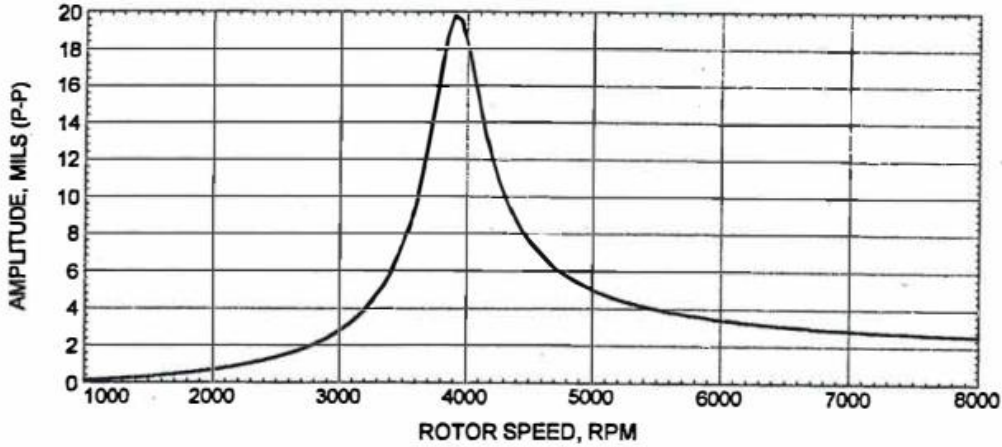


Figure 4.2 Jeffcott rotor amplitude plot [19].

The damping and stiffness of the bearings also influence LRVs. Their effect can be implemented by using an equivalent stiffness and damping approach or considering a 3-mass system as shown below. The general model for an off centered disk position is 8DOF due to the gyroscopic effect with $(x_1, y_1, x_2, y_2, \theta_x, \theta_y, x_3, y_3)$ as the coordinate vector. This system can be simplified using a symmetric model. In the simplified version the 8-element q vector becomes (x_1, y_1, x_2, y_2) . Notating effective journal mass $m_1 = m_3 = m_b$, effective disk mass $m_2 = M$, journal center D, and disk center J the equations of motion for the journal center and the disk center can be derived.

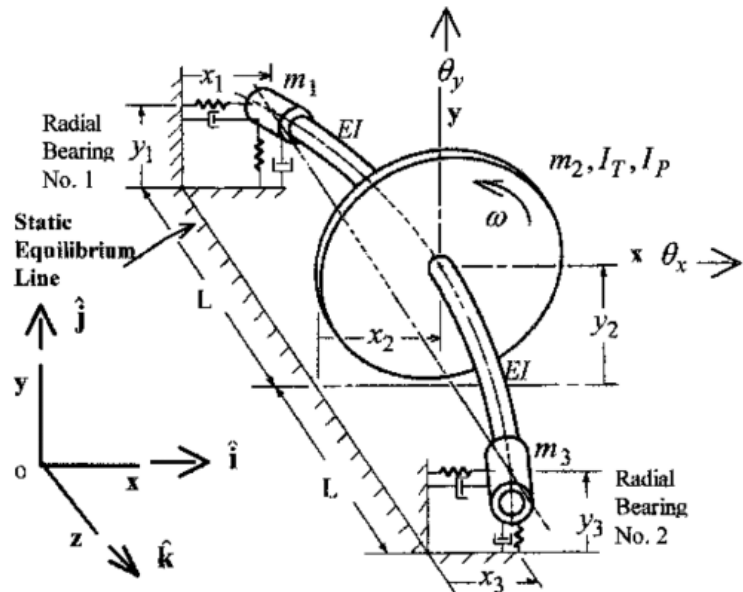


Figure 4.3 Jeffcott rotor on flexible supports [14].

Equations of motions are:

$$m_2 \ddot{x}_2 + C(\dot{x}_2 - \dot{x}_1) + K(x_2 - x_1) = f_x(t) \quad (4.7)$$

$$m_2 \ddot{y}_2 + C(\dot{y}_2 - \dot{y}_1) + K(y_2 - y_1) = f_y(t) \quad (4.8)$$

$$m_1 \ddot{x}_1 + C(\dot{x}_1 - \dot{x}_2) + K(x_1 - x_2) = -F_x \quad (4.9)$$

$$m_1 \ddot{y}_1 + C(\dot{y}_1 - \dot{y}_2) + K(y_1 - y_2) = -F_y \quad (4.10)$$

The F_x, F_y are the fluid film bearing forces applied to the journal, m_b is the effective journal mass, (generally taken $m_j = 0.25m_{shaft}$). In SFDs a squirrel cage that acts as a restoring force connects the journal to the ground. Its effect can be incorporated in journal equations by adding $K_r x_E$.and $K_r y_E$ terms to LHS. This method of deriving governing equations is useful while testing active controller schemes.

For symmetric disk position, the tilt of the disk is described by θ_x, θ_y , disks transverse inertia J_t and polar inertia J_p . This gyroscopic effect only affects disk tilt and is simplified due to symmetry. In unsymmetric disk positions additional shaft coupling occurs.

$$I_t \ddot{\theta}_x + K_\theta \theta_x + G \dot{\theta}_y = 0 \quad (4.11)$$

$$I_t \ddot{\theta}_y + K_\theta \theta_y - G \dot{\theta}_x = 0 \quad (4.12)$$

Where $G = \omega I_p$. Disk inertias and shafts resistance against disk tilt are found by the following equations. The gyroscopic effect on disk equations is achieved by adding $-G\theta_x$ and $G\theta_y$ to disks x, y equations.

$$K_\theta = \frac{3EI}{L} \quad (4.13)$$

$$J_p = \frac{3mR^2}{8} \quad (4.14)$$

$$J_t = \frac{mR^2}{8} \quad (4.15)$$

Airplane jet engines consist of multiple stages of compressor and turbine blades where a hollow shaft can connect these components in multi spool configurations supported by multiple bearings. For this reason, modelling the jet rotor as a Jeffcott rotor yields a degraded version of its actual multi critical speed complex behavior. A better approach is to model jet rotor spools using a lumped FEM model using beam elements.

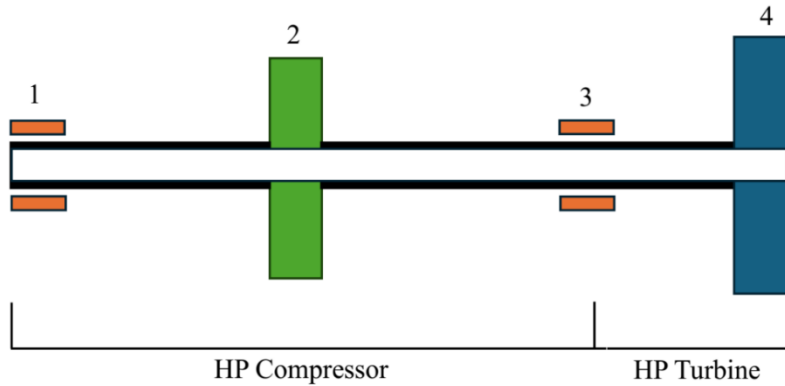


Figure 4.4 Lumped jet rotor model

The figure above shows the lumped model of the HP spool of A330 airplane. To simulate rotor behavior correctly we will develop FEM building blocks in Simulink based on the governing equations derived from the global mass, spring, and gyroscopic effect matrices of back-to-back beam elements.

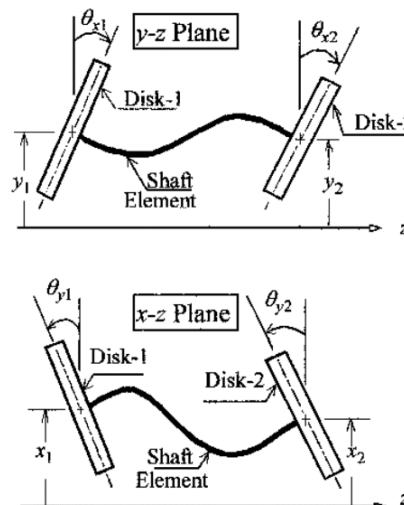


Figure 4.5 Basic FEM building block for rotor simulations [14].

Each element has 8 DOF ($x_1, y_1, \theta_{x1}, \theta_{y1}, x_2, y_2, \theta_{x2}, \theta_{y2}$) and for an N element rotor the overall DOF is $8(N+1)$. Mass, stiffness and gyroscopic matrices are built considering the coordinates shown above. The mass matrix can be modeled in 3 approaches. Namely lumped, distributed, and consistent. Since we will use Simulink for modelling, using the lumped mass matrix will be the best option. The lumped mass matrix is [14]:

$$[M]_i^{-1} = \begin{bmatrix} \frac{1}{2}M_i^{(s)} & 0 & 0 & 0 & 0 & 0 & 0 & 0 \\ 0 & \frac{1}{2}M_i^{(s)} & 0 & 0 & 0 & 0 & 0 & 0 \\ 0 & 0 & I_{Ti} & 0 & 0 & 0 & 0 & 0 \\ 0 & 0 & 0 & I_{Ti} & 0 & 0 & 0 & 0 \\ 0 & 0 & 0 & 0 & \frac{1}{2}M_i^{(s)} & 0 & 0 & 0 \\ 0 & 0 & 0 & 0 & 0 & \frac{1}{2}M_i^{(s)} & 0 & 0 \\ 0 & 0 & 0 & 0 & 0 & 0 & I_{Ti} & 0 \\ 0 & 0 & 0 & 0 & 0 & 0 & 0 & I_{Ti} \end{bmatrix} \quad (4.16)$$

Where M is the lumped mass of the element and I_{Ti} is the transverse moment of inertia lumped at disk locations using the parallel axis theorem.

$$I_{Ti} = \frac{1}{96} M^{(s)} (3(d_o^2 + d_i^2)) + \frac{M^{(s)} L^2}{32} \quad (4.17)$$

The element stiffness matrix is [14]:

$$[K]_i = K^* \begin{bmatrix} 6 & 0 & 0 & 3L_i & -6 & 0 & 0 & 3L_i \\ 0 & 6 & -3L_i & 0 & 0 & -6 & -3L_i & 0 \\ 0 & -3L_i & 2L_i^2 & 0 & 0 & 3L_i & L_i^2 & 0 \\ 3L_i & 0 & 0 & 2L_i^2 & -3L_i & 0 & 0 & L_i^2 \\ -6 & 0 & 0 & -3L_i & 6 & 0 & 0 & -3L_i \\ 0 & -6 & 3L_i & 0 & 0 & 6 & 3L_i & 0 \\ 0 & -3L_i & L_i^2 & 0 & 0 & 3L_i & 2L_i^2 & 0 \\ 3L_i & 0 & 0 & L_i^2 & -3L_i & 0 & 0 & 2L_i^2 \end{bmatrix} \quad (4.18)$$

Where L_i is element length and $K^* = 2E_i I_i / L_i^3$. For an element with length L_i the stiffness values can get quite large due to L_i^3 term especially for very small elements. In simulation we aim to model a small number of mass stations, therefore possible numerical problems that can arise from

determinant will not occur. It is important to notice that when gyroscopic effects are neglected, the mass and stiffness matrices for a 3-element system give out the Jeffcott rotor model. The gyroscopic matrix is given by [13]:

$$[G]_i^{(s)} = \begin{bmatrix} 0 & 0 & 0 & 0 & 0 & 0 & 0 \\ 0 & 0 & 0 & 0 & 0 & 0 & 0 \\ 0 & 0 & 0 & \omega I_{Pi} & 0 & 0 & 0 \\ 0 & 0 & -\omega I_{Pi} & 0 & 0 & 0 & 0 \\ 0 & 0 & 0 & 0 & 0 & 0 & 0 \\ 0 & 0 & 0 & 0 & 0 & 0 & 0 \\ 0 & 0 & 0 & 0 & 0 & 0 & \omega I_{Pi} \\ 0 & 0 & 0 & 0 & 0 & -\omega I_{Pi} & 0 \end{bmatrix} \quad (4.19)$$

Where I_{Pi} is element polar moment of inertia given by:

$$I_{Pi} = \frac{1}{16} M^{(s)} (d_o^2 + d_i^2) \quad (4.20)$$

In gyroscopic matrix $[G]$, the signs of gyroscopic inertia are opposite. This is due to the coordinate cross product when the formula for gyroscopic moment $I_p(\omega \times \dot{\theta})$ is applied for $\dot{\theta}_x$ and $\dot{\theta}_y$ with ω . The overall system of equations for unforced and unsupported shaft is given by:

$$[M]\{\ddot{q}\} + [G]\{\dot{q}\} + [K]\{q\} = 0 \quad (4.21)$$

We can also write the equations of motions for the system explicitly as (see Appendix):

$$M\ddot{x}_1 + 6K^*(x_1 - x_2) + 3K^*L(\theta_{y1} + \theta_{y2}) = 0 \quad (4.22)$$

$$M\ddot{y}_1 + 6K^*(y_1 - y_2) - 3K^*L(\theta_{x1} + \theta_{x2}) = 0 \quad (4.23)$$

$$I_t\ddot{\theta}_{x1} + K^*L^2(2\theta_{x1} + \theta_{x2}) + I_p w \dot{\theta}_{y1} - 3K^*L(y_1 - y_2) = 0 \quad (4.24)$$

$$I_t\ddot{\theta}_{y1} + K^*L^2(2\theta_{y1} + \theta_{y2}) - I_p w \dot{\theta}_{x1} + 3K^*L(x_1 - x_2) = 0 \quad (4.25)$$

$$M\ddot{x}_2 + 6K^*(x_2 - x_1) - 3K^*L(\theta_{y1} + \theta_{y2}) = 0 \quad (4.26)$$

$$M\ddot{y}_2 + 6K^*(y_2 - y_1) + 3K^*L(\theta_{x1} + \theta_{x2}) = 0 \quad (4.27)$$

$$I_t \ddot{\theta}_{x2} + K^* L^2 (2\theta_{x2} + \theta_{x1}) + I_p w \dot{\theta}_{y2} - 3K^* L (y_1 - y_2) = 0 \quad (4.28)$$

$$I_t \ddot{\theta}_{y2} + K^* L^2 (2\theta_{y2} + \theta_{y1}) - I_p w \dot{\theta}_{x2} + 3K^* L (x_1 - x_2) = 0 \quad (4.29)$$

Here $6K^*$, $3K^*L$, and K^*L^2 terms are common; thus, they can be denoted as K_1 , K_2 , and K_3 . By adding a second element to the system above we can make up a formulation for how starting, internal, and final nodes look like. Equations for the second element are:

$$M \ddot{x}_2 + 6K^*(x_2 - x_3) + 3K^*L(\theta_{y2} + \theta_{y3}) = 0 \quad (4.30)$$

$$M \ddot{y}_2 + 6K^*(y_2 - y_3) - 3K^*L(\theta_{x2} + \theta_{x3}) = 0 \quad (4.31)$$

$$I_t \ddot{\theta}_{x2} + K^* L^2 (2\theta_{x2} + \theta_{x3}) + I_p w \dot{\theta}_{y2} - 3K^* L (y_2 - y_3) = 0 \quad (4.32)$$

$$I_t \ddot{\theta}_{y2} + K^* L^2 (2\theta_{y2} + \theta_{y3}) - I_p w \dot{\theta}_{x2} + 3K^* L (x_2 - x_3) = 0 \quad (4.33)$$

$$M \ddot{x}_3 + 6K^*(x_3 - x_2) - 3K^*L(\theta_{y2} + \theta_{y3}) = 0 \quad (4.34)$$

$$M \ddot{y}_3 + 6K^*(y_3 - y_2) + 3K^*L(\theta_{x2} + \theta_{x3}) = 0 \quad (4.35)$$

$$I_t \ddot{\theta}_{x3} + K^* L^2 (2\theta_{x3} + \theta_{x2}) + I_p w \dot{\theta}_{y3} - 3K^* L (y_2 - y_3) = 0 \quad (4.36)$$

$$I_t \ddot{\theta}_{y3} + K^* L^2 (2\theta_{y3} + \theta_{y2}) - I_p w \dot{\theta}_{x3} + 3K^* L (x_2 - x_3) = 0 \quad (4.37)$$

In FE modelling element governing equations are summed to give out the global matrices. This is generally done in matrix form [14]. Here we show the longer form because the subsequent Simulink model for starting, internal, and final nodes will be developed using the governing derived here. For the starting node (node 1):

$$M \ddot{x}_1 + 6K^*(x_1 - x_2) + 3K^*L(\theta_{y1} + \theta_{y2}) = 0 \quad (4.38)$$

$$M \ddot{y}_1 + 6K^*(y_1 - y_2) - 3K^*L(\theta_{x1} + \theta_{x2}) = 0 \quad (4.39)$$

$$I_t \ddot{\theta}_{x1} + K^* L^2 (2\theta_{x1} + \theta_{x2}) + I_p w \dot{\theta}_{y1} - 3K^* L (y_1 - y_2) = 0 \quad (4.40)$$

$$I_t \ddot{\theta}_{y1} + K^* L^2 (2\theta_{y1} + \theta_{y2}) - I_p w \dot{\theta}_{x1} + 3K^* L(x_1 - x_2) = 0 \quad (4.41)$$

For an internal node (node 2):

$$2M\ddot{x}_2 + 6K^*(2x_2 - x_1 - x_3) + 3K^*L(\theta_{y3} - \theta_{y1}) = 0 \quad (4.42)$$

$$2M\ddot{y}_2 + 6K^*(2y_2 - y_1 - y_3) - 3K^*L(\theta_{x3} - \theta_{x1}) = 0 \quad (4.43)$$

$$2I_t \ddot{\theta}_{x2} + K^* L^2 (4\theta_{x1} + \theta_{x1} + \theta_{x3}) + 2I_p w \dot{\theta}_{y2} + 3K^* L(y_3 - y_1) = 0 \quad (4.44)$$

$$2I_t \ddot{\theta}_{y2} + K^* L^2 (2\theta_{y1} + \theta_{y1} + \theta_{y3}) - 2I_p w \dot{\theta}_{x2} - 3K^* L(x_3 - x_1) = 0 \quad (4.45)$$

For the final node (node 3):

$$M\ddot{x}_3 + 6K^*(x_3 - x_2) - 3K^*L(\theta_{y2} + \theta_{y3}) = 0 \quad (4.46)$$

$$M\ddot{y}_3 + 6K^*(y_3 - y_2) + 3K^*L(\theta_{x2} + \theta_{x3}) = 0 \quad (4.47)$$

$$I_t \ddot{\theta}_{x3} + K^* L^2 (2\theta_{x3} + \theta_{x3}) + I_p w \dot{\theta}_{y3} - 3K^* L(y_2 - y_3) = 0 \quad (4.48)$$

$$I_t \ddot{\theta}_{y3} + K^* L^2 (2\theta_{y3} + \theta_{y2}) - I_p w \dot{\theta}_{x3} + 3K^* L(x_2 - x_3) = 0 \quad (4.49)$$

The bearing support stiffness, damping force, and disk imbalance force can be added to the node points where they exist as forcing functions. However, disk mass and inertia effects must be lumped at node points as we used the lumped mass assumption. This must be done differently for end and internal nodes. For end nodes the lumped mass becomes $M_{lumped} = 0.5M_{element} + M_{disk}$ and for internal nodes $M_{lumped} = M_{element} + M_{disk}$ as two beam element halves are lumped at internal nodes. The procedure for lumping inertia for end and internal nodes is similar.

In summary, there are various methods to model rotors. Jeffcott and symmetrical multi mass models give good results when the center of mass of disks are close to shaft horizontal center. However, when one disk is between two bearings and one disk is outside like in the jet rotor HP spool model, it is better to use FE models for realism as FE models include more complex mass and stiffness couplings.

4.2) Bearings

4.2.1) Hydrodynamic Bearings

One of the most common bearings used in vibration attenuation is the hydrodynamic fluid film bearing. Its history, compared to others, starts from an earlier age as people have used various natural oils to lubricate their chariots and carriages for smoother operation. However, in the context of mechanical engineering the explanation of their behavior coincided with the late 19th century. In 1886 Osborne Reynolds proposed an explanation for load carrying oil film that Beauchamp Tower showcased in 1883 [16],[20].

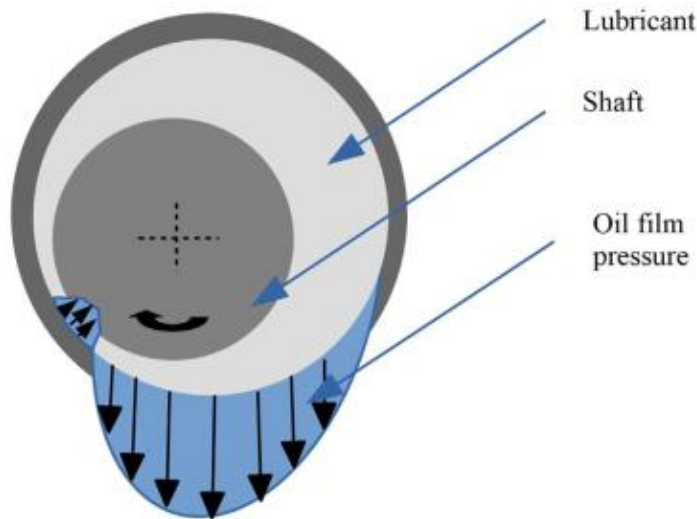


Figure 4.6 Film pressure in a hydrodynamic bearing. [20]

Figure 4.6 shows journal, housing and oil the pressure in a hydrodynamic bearing. During the rest the fluid only exerts static pressure to lift the shaft. As the rotor speeds up an additional lift force due to a wedge formed by the relative movement of the two sliding surfaces pushes the shaft to bearing center. Eventually, the forces (hydrodynamic, and load direction) balance out and an orbit form [20]. Thus, the journal shows two kinds of motions. First, it spins around the rotor axis at shaft speed. Secondly, it whirls around the orbit center. The film pressure is explained by RE.

$$\frac{\partial}{\partial x} \left[\frac{h^3}{\mu} \left(\frac{\partial p}{\partial x} \right) \right] + \frac{\partial}{\partial z} \left[\frac{h^3}{\mu} \left(\frac{\partial p}{\partial z} \right) \right] = 6U \frac{dh}{dx} + 12 \frac{dh}{dt} \quad (4.50)$$

Here $p(x,z)$ is distribution of lubricating film pressure, $h(x,z)$ is the distribution of lubricating film thickness, U is sliding film velocity, and μ is lubricant viscosity. The left-hand side of the RE is composed of axial and circumferential pressure distribution and the right-hand side contains the sliding velocity and lubricating film velocity [20].

The RE has no exact solution therefore approximations for lowering the complexity are used. Two common approximations are the short and long bearing assumptions that idealize specific bearing assemblies. These lower the 2D RE equation to 1D by neglecting variation of pressure on axial or circumferential axis. Assuming that the lubricant is incompressible further simplification can be made. From the found pressure distribution equation and its integration damping and stiffness coefficients are found. In the short bearing assumption, the circumferential pressure gradient ($\partial p / \partial z$) in equation (4.51) is taken as zero due to its effect being minute compared to axial pressure gradient as shown in equation (4.52) below.

$$\frac{\partial}{\partial x} \left[\frac{h^3}{1} \left(\frac{\partial p}{\partial x} \right) \right] = 6\mu U \frac{dh}{dx} + 12\mu \frac{dh}{dt} \quad (4.51)$$

The long bearing assumption on the other hand neglect ($\partial p / \partial x$) as $(\partial p / \partial z) \gg (\partial p / \partial x)$.

$$\frac{\partial}{\partial z} \left[\frac{h^3}{1} \left(\frac{\partial p}{\partial z} \right) \right] = 6\mu U \frac{dh}{dx} + 12\mu \frac{dh}{dt} \quad (4.52)$$

These equations are solved considering the bearing geometry and end conditions (seals). Damping generated by the short and long bearings differs as the pressure generated on each have different profiles as shown below.

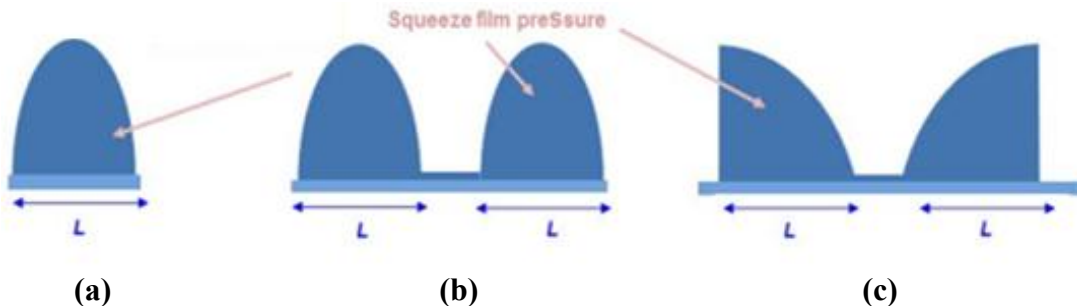


Figure 4.7 Squeeze film pressure in three configurations. (a) the lubricant is squeezed between two plates. (b) lubricant pressure in open ended bearing with a center groove. (c) lubricant pressure in sealed bearing with a center groove [11].

On short bearings ($L < D$) the lubricant circulates before high pressure builds up. For this reason, they are also referred to as open ended bearings [20]. On long bearings ($L > D$) the pressure develops further. End seals that block side leakage simulate this effect. Thus, compared to short bearings, long bearings show higher peak pressure and higher damping.

In hydrodynamic bearings the damping and friction at high speeds can lead to excessive heat generation, especially on long dampers. For this reason, lubricant circulation by external pumps is important for minimizing the viscosity change by increasing temperature which can lead to excessive orbits, higher vibration amplitude during critical speeds, and finally metal to metal contact [18]. Also, the possibility of fluid film induced instabilities like oil whip in addition to space constraints limit the application of hydrodynamic journal bearings in jet engines [23].

4.2.2 The Squeeze Film Damper

The principle behind the squeeze film damper is similar to the journal bearings such that the damping force is related to the pressure distribution in the fluid film. However, due to nonrotating journal and high operation speeds, phenomena such as air ingestion, cavitation, fluid inertia become more pronounced. Therefore, SFD models employ a modified RE.

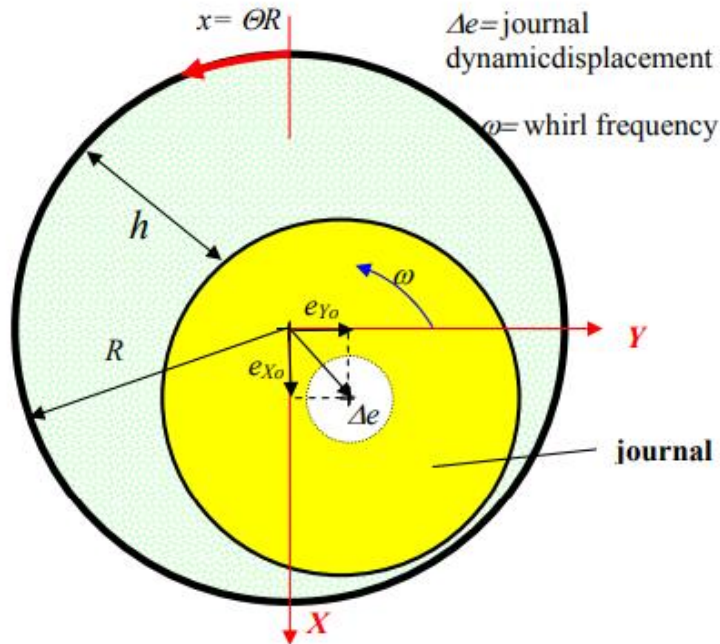


Figure 4.8 View of journal coordinates.[23].

In cylindrical coordinates the modified RE is:

$$\frac{\partial}{\partial \Theta} \left[\left(\frac{h^3 \partial p}{R \partial \Theta} \right) \right] + \frac{\partial}{\partial z} \left[\left(\frac{h^3 \partial p}{\partial z} \right) \right] = (ph^2) \frac{\partial^2 h}{\partial t^2} + 12\mu \frac{\partial h}{\partial t} \quad (4.53)$$

The film thickness depends on the movement journal and has both static (e_{X0}, e_{Y0}) and dynamic ($\Delta e_{X0}, \Delta e_{Y0}$) components. In synchronous circular centered orbits, the static part becomes zero and the film thickness only depends on the instantaneous eccentricity of the journal.

$$h = c - e \cos(\omega t) \quad (4.54)$$

Linearized damping and inertia coefficients are determined using the modified Reynolds equation. The simplest approach considers small amplitude ($e_j \rightarrow 0$) journal motions about centered position for an isoviscous lubricant. The results are applicable up to $e/c = 0.25$.[23]

$$C_{XX} = C_{YY} = C_{tt} = 12\pi \frac{\mu R^3 L}{c^3} \left[\frac{\left(\frac{L}{D}\right) - \tanh\left(\frac{L}{D}\right)}{\left(\frac{L}{D}\right)} \right] \quad (4.55)$$

$$M_{XX} = M_{YY} = M_{rr} = \pi \frac{\rho R^3 L}{c} \left[\frac{\left(\frac{L}{D}\right) - \tanh\left(\frac{L}{D}\right)}{\left(\frac{L}{D}\right)} \right] \quad (4.56)$$

Where μ is dynamic viscosity, R is bearing radius, L is film land length, ρ is lubricant density, and c is journal clearance. The hyperbolic function can further be simplified by considering the short and long damper configurations. For open ended bearings $L/D \rightarrow 0$,

$$C_{XX} = C_{YY} = C_{tt} = \frac{\pi \mu D L^3}{2c^3} \quad (4.57)$$

$$M_{XX} = M_{YY} = M_{rr} = \frac{\pi \rho D L^3}{24c} \quad (4.58)$$

For fully sealed bearings $L/D \rightarrow \infty$,

$$C_{XX} = C_{YY} = C_{tt} = \frac{3\pi\mu D^3 L}{2c^3} \quad (4.59)$$

$$M_{XX} = M_{YY} = M_{rr} = \frac{\pi\rho D^3 L}{8c} \quad (4.60)$$

The zero-amplitude solution gives us three useful insights into SFD behavior:

- 1) The damping coefficient depends on c^3 , whereas inertia coefficient depends on c .
- 2) The damping coefficient ratio between long and short bearings is $K_g = (3D^2/L^2)$ and it is a function of damper geometry. A sealed bearing provides much more damping compared to an open-ended bearing.
- 3) The ratio between the damper radial force and the tangential force quantifies the viscous vs inertia domination in SFDs (equation 28).

$$\frac{F_r}{F_t} = \frac{M^*(e\omega^2)}{C^*(e\omega)} = \frac{\rho\omega c^2}{12\mu} = \frac{Re_s}{12} \quad (4.61)$$

From equation (4.61) we see that the inertial effects become dominant when $Re_s > 12$. In actual operation, the film pressure depends on both static and dynamic eccentricity. However, their respective magnitude varies with operation regime. In active SFD the main aim is to combat rotor vibrations due to the unbalance response.

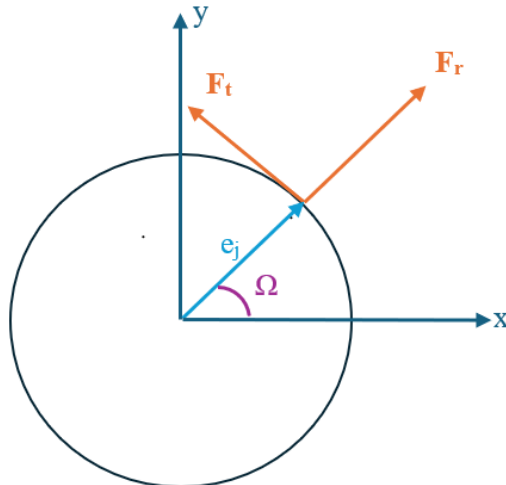


Figure 4.9 The circular centered orbit.

For this purpose, static eccentricity can be neglected and a CCO motion can be assumed [6]. The linearized coefficients for full film CCO are derived by San Andres et. al. [5]. Figure 4.9 above shows the fixed bearing coordinates and whirling coordinates for a CCO. The radial velocity is $V_t = e_j \omega$, radial acceleration is $A_r = e_j \omega^2$, and the synchronous whirl speed is $\Omega = \omega t$. The radial and tangential components of the film reaction are written using the damping and inertia coefficients as:

$$F_r = \{C_{rt}V_t + M_{rr}A_r\} \quad (4.62)$$

$$F_t = \{C_{tt}V_t + M_{tr}A_r\} \quad (4.63)$$

The whirling coordinates (r, t) is related to fixed (X, Y) coordinates using the following transform.

$$F_X = F_r \cos(\Omega) - F_t \sin(\Omega) \quad (4.64)$$

$$F_Y = F_r \sin(\Omega) + F_t \cos(\Omega) \quad (4.65)$$

$$R(\omega t) = \begin{bmatrix} \cos(\Omega) & -\sin(\Omega) \\ \sin(\Omega) & \cos(\Omega) \end{bmatrix} \quad (4.66)$$

The coefficients $\{C_{tt}, C_{rt}, M_{tr}, M_{rr}\}$ for the cavitated film for open ended SFDs are given below.

$$C_{tt} = \frac{\pi D L^3 \mu}{4 c^3 \gamma^3} \quad (4.67)$$

$$C_{rt} = \frac{\pi D L^3 \varepsilon \mu}{c^3 \gamma^4} \quad (4.68)$$

$$M_{rr} = \frac{\pi D L^3 \rho (2 \gamma - 1) (\gamma - 1)}{24 c \varepsilon^2 \gamma} \quad (4.69)$$

$$M_{tr} = \frac{27 D L^3 \rho \left(\frac{\ln(-\frac{\varepsilon-1}{\varepsilon+1})}{\varepsilon} + 2 \right)}{140 c \varepsilon} \quad (4.70)$$

Where $\varepsilon = e_j/c$ is dimensionless journal eccentricity and $\gamma = \sqrt{1 - \varepsilon^2}$. When cavitation is neglected, the cross coefficients become zero and the direct coefficients double. Thus:

$$F_r = M_{rr}e_j\omega^2 \quad (4.71)$$

$$F_t = C_{tt}e_j\omega \quad (4.72)$$

Hence, F_X, F_Y becomes:

$$F_X = M_{rr}e_j\omega^2 \cos(\Omega) - C_{tt}e_j\omega \sin(\Omega) \quad (4.73)$$

$$F_Y = M_{rr}e_j\omega^2 \sin(\Omega) + C_{tt}e_j\omega \cos(\Omega) \quad (4.74)$$

Since, $e_j\omega^2 \cos(\Omega) = \ddot{x}_J$, $-e_j\omega \sin(\Omega) = -\dot{x}_J$, $e_j\omega^2 \sin(\Omega) = \ddot{y}_J$, and $e_j\omega \cos(\Omega) = \dot{y}_J$:

$$F_X = M_{rr}\ddot{x}_J + C_{tt}\dot{x}_J \quad (4.75)$$

$$F_Y = M_{rr}\ddot{y}_J + C_{tt}\dot{y}_J \quad (4.76)$$

For the short damper, equations (4.75) and (4.76) can be directly substituted for F_X and F_Y .

$$m_1\ddot{x}_1 + C(\dot{x}_1 - \dot{x}_2) + K(x_1 - x_2) = -(M_{rr}\ddot{x}_J + C_{tt}\dot{x}_J) \quad (4.77)$$

$$m_1\ddot{y}_1 + C(\dot{y}_1 - \dot{y}_2) + K(y_1 - y_2) = -(M_{rr}\ddot{y}_J + C_{tt}\dot{y}_J) \quad (4.78)$$

In the long damper mode, gain factor of $K_g = (3D^2/L^2)$ must be added.

$$m_1\ddot{x}_1 + C(\dot{x}_1 - \dot{x}_2) + K(x_1 - x_2) = -K_g(M_{rr}\ddot{x}_J + C_{tt}\dot{x}_J) \quad (4.79)$$

$$m_1\ddot{y}_1 + C(\dot{y}_1 - \dot{y}_2) + K(y_1 - y_2) = -K_g(M_{rr}\ddot{y}_J + C_{tt}\dot{y}_J) \quad (4.80)$$

Figure 4.10 shows the variation of CCO coefficients with increasing journal eccentricity. The CCO coefficients are well represented by the small amplitude coefficients up to 0.25 eccentricity. Also, the experiments show that nonlinearity predicted at high eccentricities are not correct.

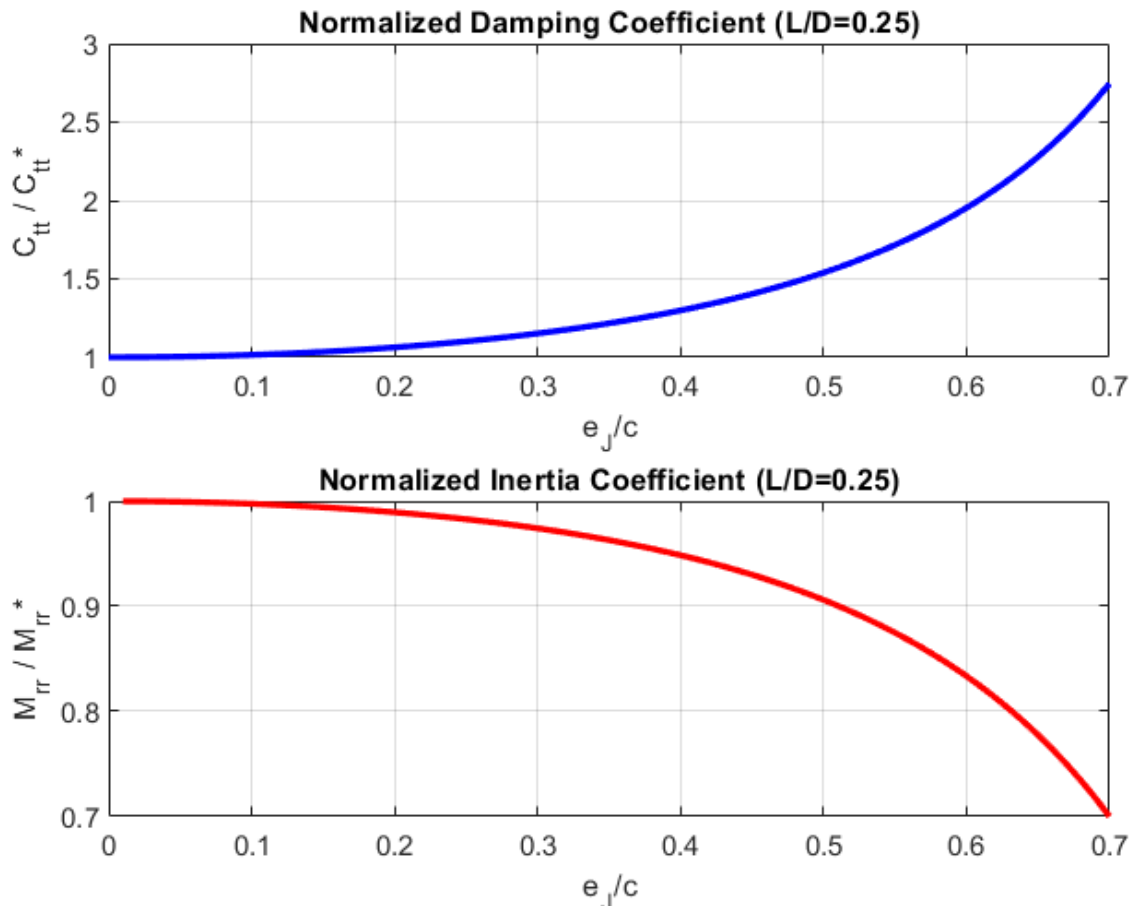


Figure 4.10 Eccentricity dependent coefficients normalized by static coefficients.

Furthermore, since the long damper mode is characterized by low eccentricity journal orbits, the coefficients in $K_g(M_{rr}\ddot{x}_J + C_{tt}\dot{x}_J)$ can be replaced by the small amplitude ($e_j \rightarrow 0$) linearized coefficients. This assumption decreases the nonlinearity in state equations.

4.3) Active Sealing Ring System

The SFD can be activated by a scheme that allows lubricant drainage in SD mode and blockage in LD mode. Considering this, force equilibrium on a piston like seal ring can be used for changing the end condition. When the pressure difference between seal ring chamber and bearing is positive the seal ring will move towards the journal end and partially seal it. The schematic in Figure 4.11 can be used for modelling this setup. A drawback of this setup is, the added nonlinearity and coupling due to seal location, lubricant pressure, and eccentricity affecting each other. However, this is the most straightforward way of enabling binary and off seal position setup.

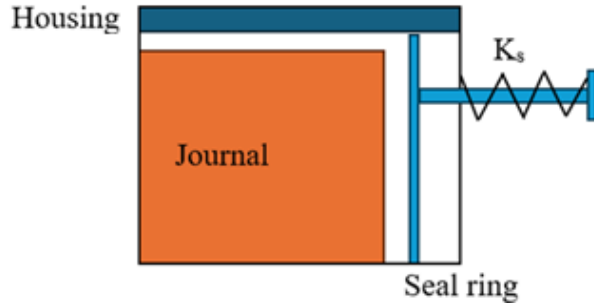


Figure 4.11 Seal ring position schematic.

The gap between the housing and the journal is the clearance c and the gap between the journal side end and the seal ring position measured from the journal is ‘ a ’. A dimensionless quantity can be defined between $(0,1)$ for specifying the seal condition as $\lambda = a/c$. When $\lambda = 0$ the bearing is fully sealed and when $\lambda = 1$ the bearing is open ended. The fluid force coefficients with varying seal position can be represented by a linear formulation depending on λ .

$$C_{tt,active} = \lambda C_{tt} + C_{tt}(1 - \lambda) \quad (4.81)$$

$$M_{rr,active} = \lambda M_{rr} + M_{rr}(1 - \lambda) \quad (4.82)$$

Experiments show that the pressure applied by squeezed film to the seal ring is comparable to the force per unit area acting on the journal ($A_j = \pi DL$) [11]. For modelling purposes, the force applied to the sealing ring can be estimated using this approach. Additionally, the force in off seal positions can be found by assuming a linear variation in the force depending seal ring position a as $F_l = F_{l,max}(1 - \lambda)$.

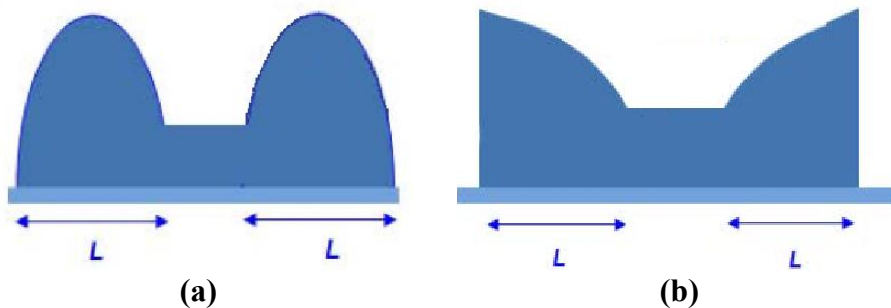


Figure 4.12 End pressure in squeeze films (a) open ended, (b) sealed [11].

Figure below shows the free body diagram of the seal ring.

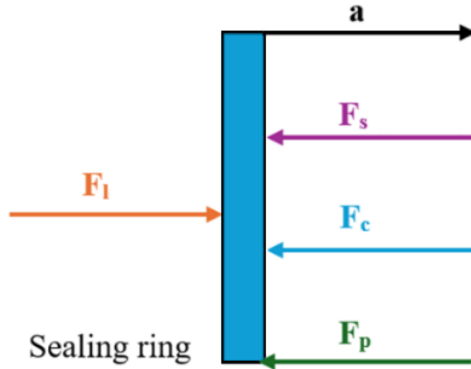


Figure 4.13 FBD of the seal ring

In the figure above, F_l is the film pressure force, F_s is seal spring force, F_c is seal damper force, F_p is the seal supply force (due to pressure), and a is the seal ring position. The equation of motion of the seal ring becomes:

$$m_s \ddot{a} + C_s \dot{a} + K_s a = F_l - F_p \quad (4.83)$$

Where m_s is seal ring mass, C_s is seal ring damping coefficient, and K_s is seal ring stiffness. The force F_p is the servo valve pressure force applied to sealing surface. The servo valve can be described using a second order differential equation as:

$$\ddot{p} + 2\zeta_p \dot{p} \omega_p + \omega_p^2 p = K_i i \quad (4.84)$$

Where p is servo valve output pressure, ω_p is valve natural frequency, ζ_p is valve damping, K_i valve static gain, and i is input current. The parameters for the valve are usually specified by the manufacturer. A suitable servo valve must allow force equilibrium in LD mode and quickly react to the control signal fast. The second condition is important for fast response to critical speeds. Fluid simulation can also be used for a more realistic approach. However, CFD is better suited to the final step of system design where the actual rotor model and film coefficients are already accounted in FEM and CFD solutions. In the initial design, the basic second-degree governing equations makes modelling much simpler without losing generality in servo valve response.

5) THE SIMULINK MODEL AND MODEL PARAMETERS

The servo valve-seal ring-bearing-rotor system that was previously described can be simulated using both the Jeffcott model and the FEM. The latter gives more realism as during operation rotor passes through multiple critical speeds. However, it is also easier to tune the controller using the Jeffcott rotor model. For this reason, we tuned the controller on a Jeffcott rotor model and then applied it to a multi mass rotor. In this chapter we will show the Simulink diagrams for both. The following assumptions are used for simplifying the model:

- The continuous shaft mass is lumped at the node locations.
- The shaft is linear, symmetrical and gyroscopic effects are negligible if symmetry exists.
- The disk center of mass lies halfway between disk ends at e away from disk center.
- The internal shaft damping is very small and negligible.
- The lubricant is isoviscous and incompressible.
- The lubricant temperature is uniform and is represented by average film temperature.
- The cross coefficients are much smaller compared to direct coefficients and are negligible.
- The damping and inertia coefficients are isotropic.
- Squirrel cage stiffness simulates soft and stiff support.
- The length of the bearing is equal to the film length and is found by the L/D ratio.
- The seal location determines the bearing mode, at $a = c$ bearing performs as open ended.
- The damping and inertia increase in LD mode is represented by K_g .
- In the SD mode lubricant pressure force to seal surface is zero. In the LD mode lubricant pressure force to seal surface is averaged between its maximum and minimum value.

5.1) Model Parameters

The parameters that we use in simulation are based on small Pratt&Whitney PW4168/4170 variants used in Airbus 330 airplanes [26][27]., engineering practice [18] and experiments on SFDs [11]. The parameters numerical values are given in Appendix The selection methodology is explained below:

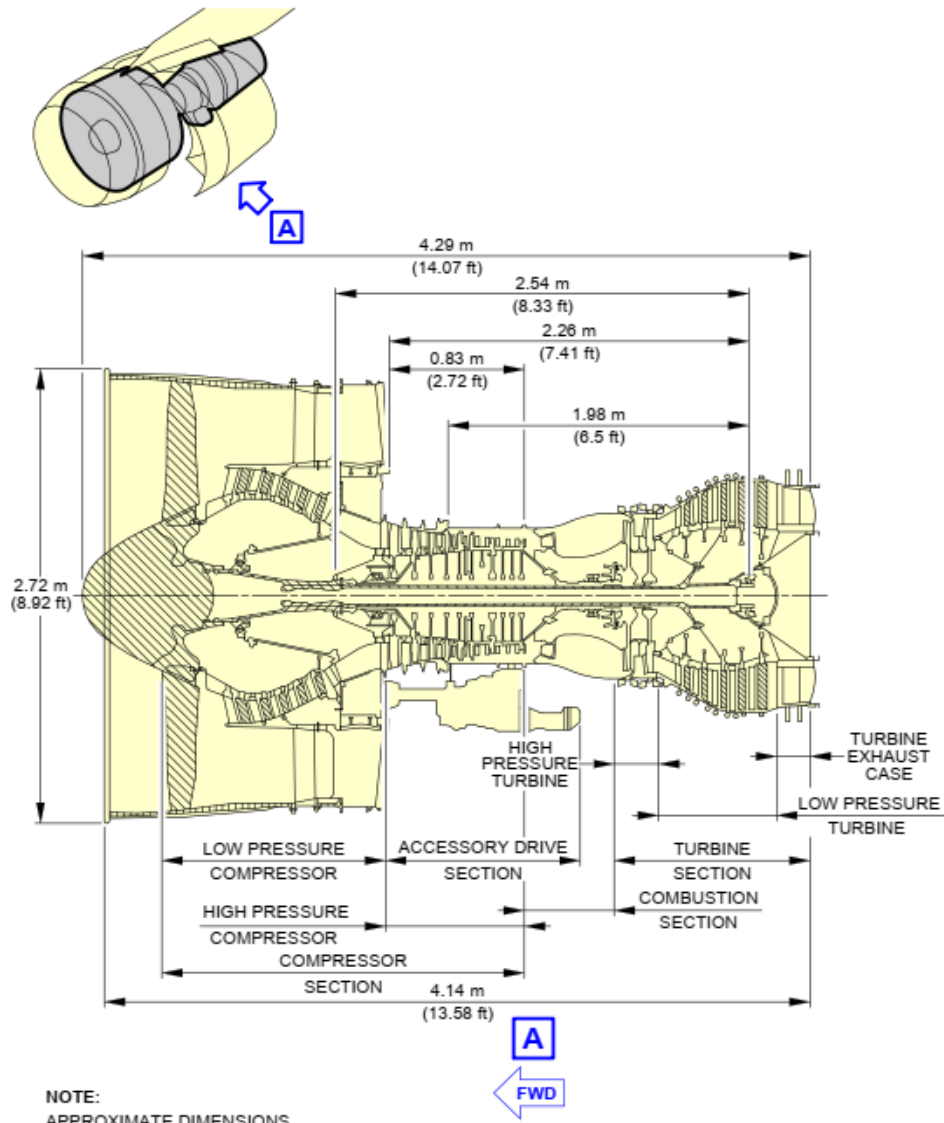
- The first critical speed of the rotor bearing assembly must be lower than the HP spool operation speed that is around 8000 rpm (N2 speed) [27].

- The ball bearing part of the SFD must be selected considering the shaft diameter. The outer diameter of the ball bearing then must be determined using ball bearing manufacturer charts.
- The lubricant properties must coincide with aircraft engine lubricant properties.

5.1.1) Rotor Dimensions

Dimensions for the HP spool are given in the figure below.

****ON A/C A330-200 A330-200F A330-300**



Engine and Nacelle
Engine Dimensions - PW 4000
FIGURE-2-12-0-991-001-A01

Figure 5.1 Pratt&Whitney PW 4000 engine dimensions [27]

Using the figure above we selected the following dimensions to use in simulations.

Table 5.1 Rotor dimensions and material properties.

Parameter	Value	Unit	Explanation
L_{shaft}	1.60	m	Shaft length.
D_{shaft}	122	mm	Shaft diameter.
t_{shaft}	14	mm	Shaft wall thickness.
$D_{disk,c}$	400	mm	Compressor disk diameter.
$t_{disk,c}$	100	mm	Compressor disk thickness.
$D_{disk,t}$	450	mm	Turbine disk diameter.
$t_{disk,t}$	100	mm	Turbine disk thickness.
ρ_{steel}	7800	kg/m^3	Assumed material density.
E	200	GPa	Assumed material elastic modulus.
e	0.25	mm	Disk center of mass eccentricity.

For the Jeffcott rotor model, stiffness is calculated as follows:

$$I = \frac{\pi(D_{shaft,o}^4 - D_{shaft,i}^4)}{64} = 7.0420 \times 10^{-6} m^4 \quad (5.1)$$

$$K = \frac{48EI}{L_{shaft}^3} = 1.733 \times 10^7 N/m \quad (5.2)$$

The shaft and disk mass are found using volume and density.

$$m_{shaft} = \frac{\rho_{steel}\pi(D_{shaft,o}^2 - D_{shaft,i}^2)L_{shaft}}{4} = 59.66 kg \quad (5.3)$$

$$m_{d,c} = \frac{\rho_{steel}\pi(D_{disk,c}^2 - D_{shaft,o}^2)t_{disk,c}}{4} = 89.5 kg \quad (5.4)$$

$$m_{d,t} = \frac{\rho_{steel}\pi(D_{disk,t}^2 - D_{shaft,o}^2)t_{disk,t}}{4} = 115.7 \text{ kg} \quad (5.5)$$

The lumped journal and disk masses are calculated as $m_d = 235 \text{ kg}$ and $m_J = 14.91 \text{ kg}$. For the FEM simulation we decided to use 10 equal beam elements. In overall the model has 11 nodes and for the first, internal, and the final nodes lumped masses and inertias differ. Also, disks mass and inertia must be lumped to the node where it is mounted. Considering the rotor dimensions, we selected node 1 and node 8 as SFD locations and node 5 and node 11 as disk locations.

For each element, mass is:

$$M_i^{(s)} = \frac{\rho_{steel}\pi(D_{shaft,o}^2 - D_{shaft,i}^2)L_i}{4} = 5.96 \text{ kg} \quad (5.6)$$

Element transverse inertia is:

$$I_{Ti} = \frac{1}{96} M^{(s)} \left(3(d_o^2 + d_i^2) \right) + \frac{M^{(s)} L^2}{32} = 0.0108 \text{ kg.m}^2 \quad (5.7)$$

Element polar moment of inertia given by:

$$I_{Pi} = \frac{1}{16} M^{(s)} (d_o^2 + d_i^2) = 0.0088 \text{ kg.m}^2 \quad (5.8)$$

Factored out stiffnesses are:

$$K_1 = 4.333 \times 10^9 \text{ N/m} \quad (5.9)$$

$$K_2 = 3.466 \times 10^9 \text{ N} \quad (5.10)$$

$$K_3 = 1.849 \times 10^7 \text{ N.m} \quad (5.11)$$

For compressor and turbine disks mass and inertia calculations are the same except one difference. The parallel axis theorem used for element transverse inertia does not apply to disk transverse inertia. The FE model is shown in the figure below.

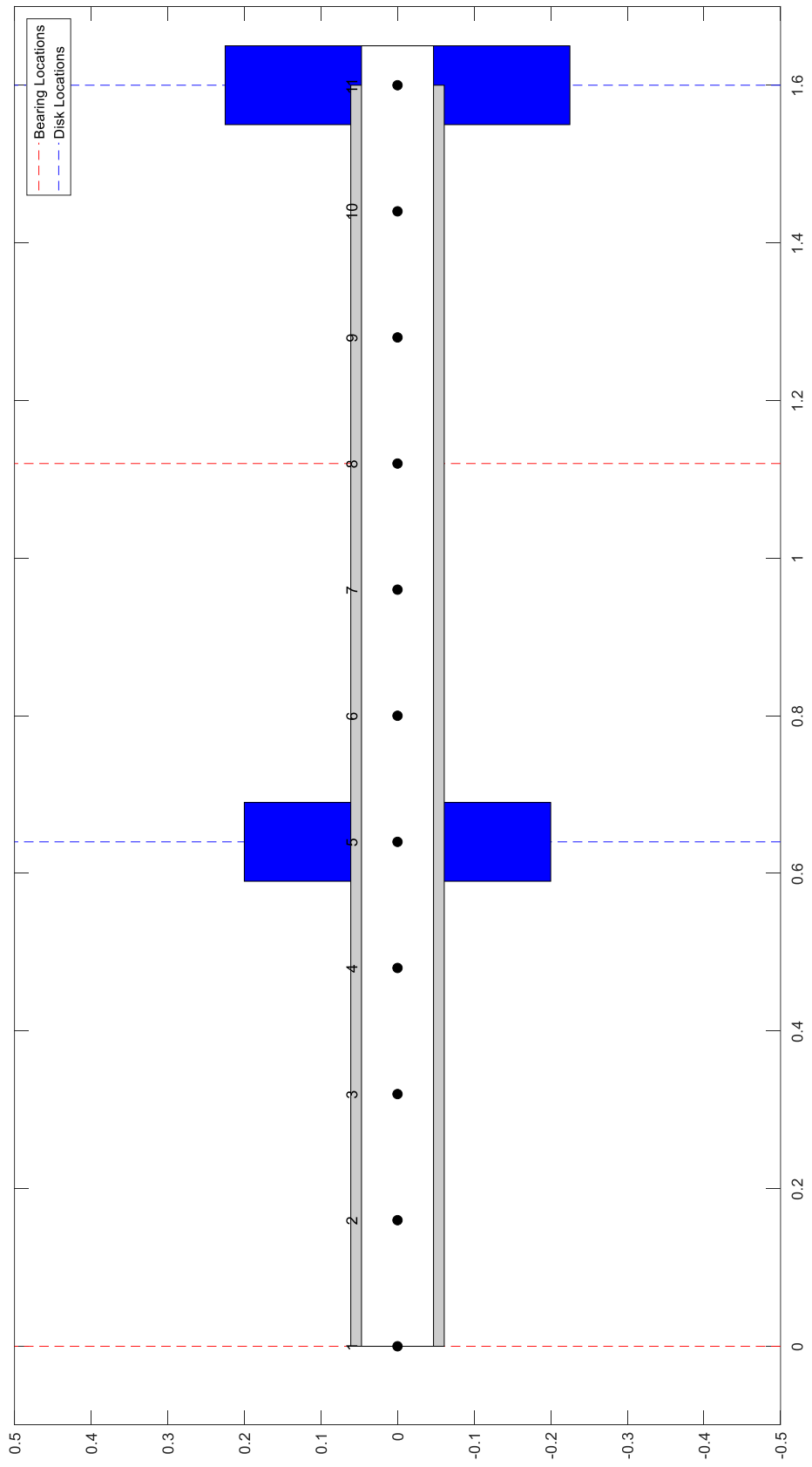


Figure 5.2 FE model with 11 elements.

5.1.2) Bearing Parameters

The SFD journal diameter must at least be as large as the outer race of the ball bearing. Since the load on the bearings is only the rotor weight, the ball bearing selection can be made using design charts found in [18]. For an outer diameter of 122 mm, recommended Single-Row 02-Series cylindrical roller bearing has an outer diameter of 215 mm. The journal surface area is $A_j = 36.3 \times 10^{-3} m^2$. Considering the dimensions of rotor and bearings we select a clearance of 0.4 mm (which is around clearances used in [11]). Sealed end gain is found from geometry as

$$K_g = 3(D/L)^2 = 3(4)^2 = 48 \quad (5.12)$$

The operating temperature of aircraft bearings is around 180°C [11] Therefore, selecting a lubricant that reproduces properties of common aircraft lubricants at room conditions is preferable. Texas A&M University SFD laboratory uses ISO VG 2 oil ($\rho = 805 \text{ kg/m}^3$, $\mu = 26.5 \text{ mPa.s}$) on their experiments, we will select the same lubricant. For $e_J \rightarrow 0$ damping and inertia coefficients on short damper found as:

$$C^* = \frac{\pi\mu DL^3}{2c^3} = 2.1715 \times 10^4 \text{ Ns/m} \quad (5.13)$$

$$M^* = \frac{\pi\rho DL^3}{24c} = 8.7953 \text{ kg} \quad (5.14)$$

The squirrel cage stiffness is an important parameter that directly affects journal vibration. However, finding an exact value for our simulation was not possible as exact dimensions are not disclosed. E.J. Gunter (2020) [28] in his conference paper on support stiffness for flexible rotors recommend a support stiffness near the shaft stiffness. Based on this , we decided to take squirrel cage stiffness as $1.733 \times 10^7 \text{ N/m}$.

5.1.3) Seal Ring and Servo Valve Parameters

Seal ring parameters are found considering seal geometry. The outer diameter of seal ring coincides with the bearing diameter, and it has a thickness of 5 mm. From these, seal ring surface area and seal ring mass are found as $A_s = 6.9 \times 10^{-3} m^2$ and $m_s = 0.2707 \text{ kg}$ respectively. The seal ring spring stiffness and inherent damping are assumed values that need validation. Their

mission is to stabilize seal movement; we believe that we can assume similar values to experiments done on active SFD [9] as $K_s = 50 \text{ N/mm}$ and $C_s = 0.007 \text{ Ns/m}$. Also, in simulations we decided to use a peak value found from the pure sealed damper force.

The servo valve must provide enough pressure force to the seal surface to enable equilibrium of forces on the LD mode where $\lambda = 0$. However, it is crucial to make sure that a pressure supply larger than the maximum LD mode pressure is not given. If this is neglected the excessive pressure will cause an unrequired load on the journal and wear contacting surfaces while making friction between seal ring and journal end significant. So, being sure that the maximum servo valve pressure sets bearing mode to quasi-LD is important. For this, the maximum input current can be constrained. The servo valve used in ref. [9] has $\omega_s = 250$, $\zeta_s = 0.7$, and $K = 0.9 \times 10^5 \text{ Pa/mA}$. It is noted that this servo valve provides fast response at rotor critical speeds.

5.2) The Open Loop System

The schematic below shows the open loop block diagram.

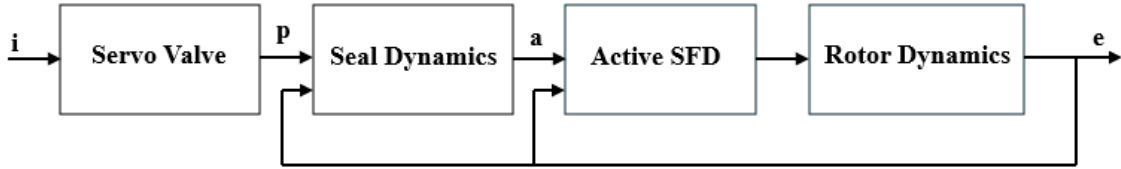


Figure 5.3 Open loop system block diagram

During steady operation, the journal whirls in a constant eccentricity orbit. When an input current i is given to the system, the force F_p moves the seal until F_l balances it at a new seal position λ . In the new seal position, the active SFD provides more damping to the rotor. This increase in damping then attenuates the vibration amplitude and decreases the journal eccentricity. The servo valve, seal dynamics and semi active SFD subsystems are common for both Jeffcott and FEM rotor models. The Jeffcott rotor open loop system and its subsystems are shown in the following pages.

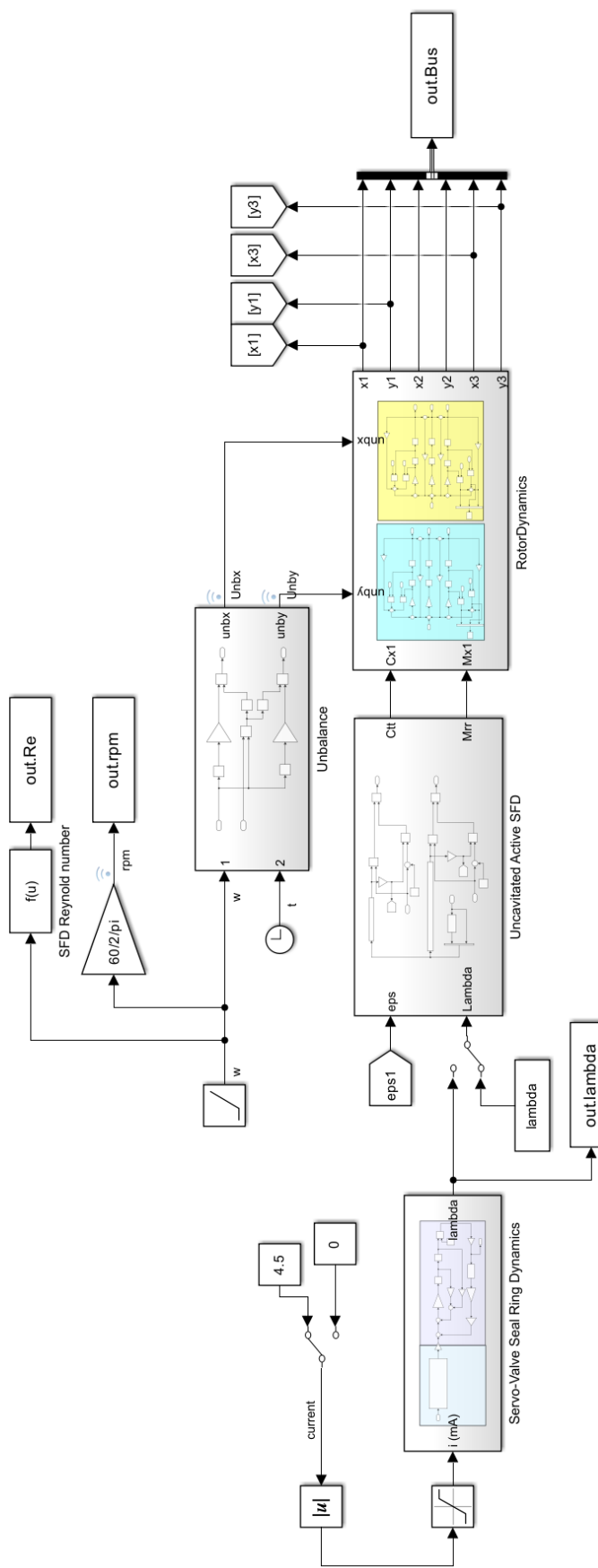


Figure 5.4 Jeffcott rotor open loop system block diagram.

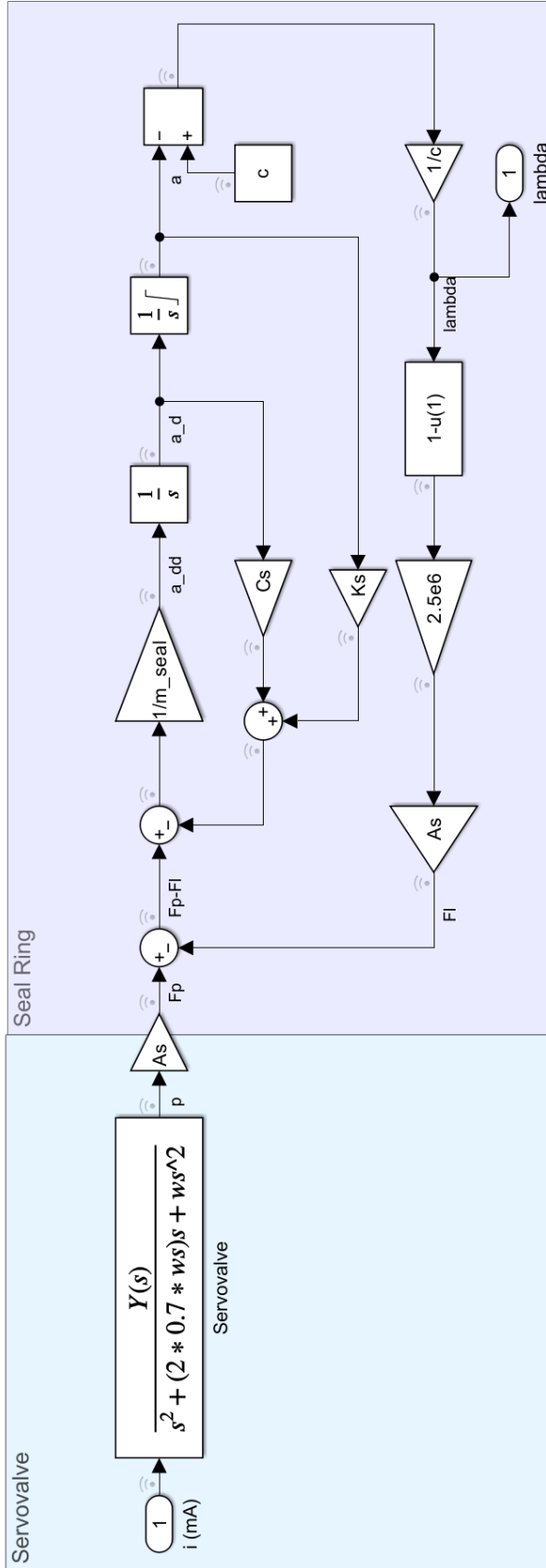


Figure 5.5 Servovalve and seal dynamics system subsystem.

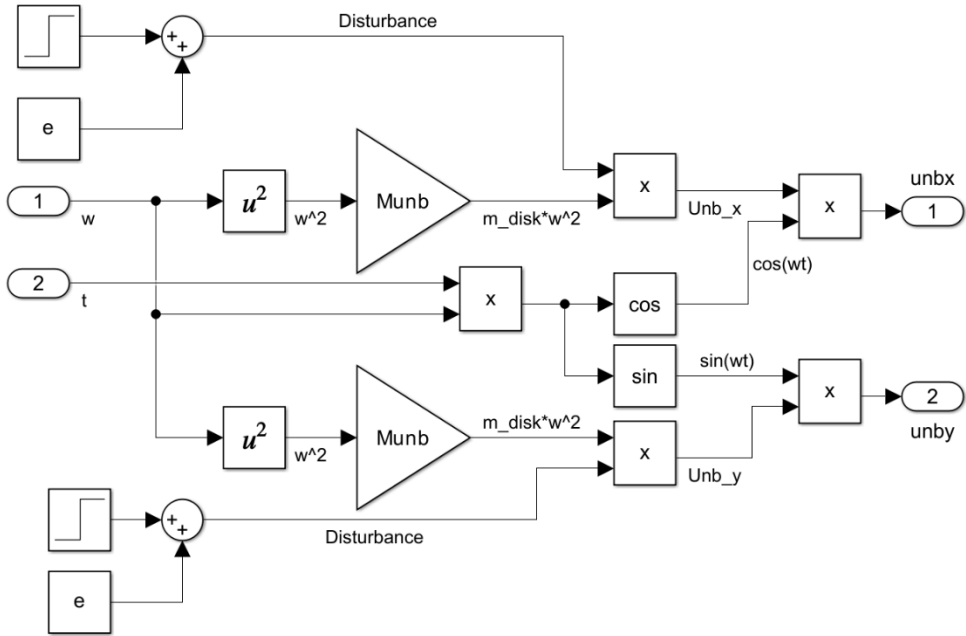


Figure 5.7. Imbalance with disturbance.

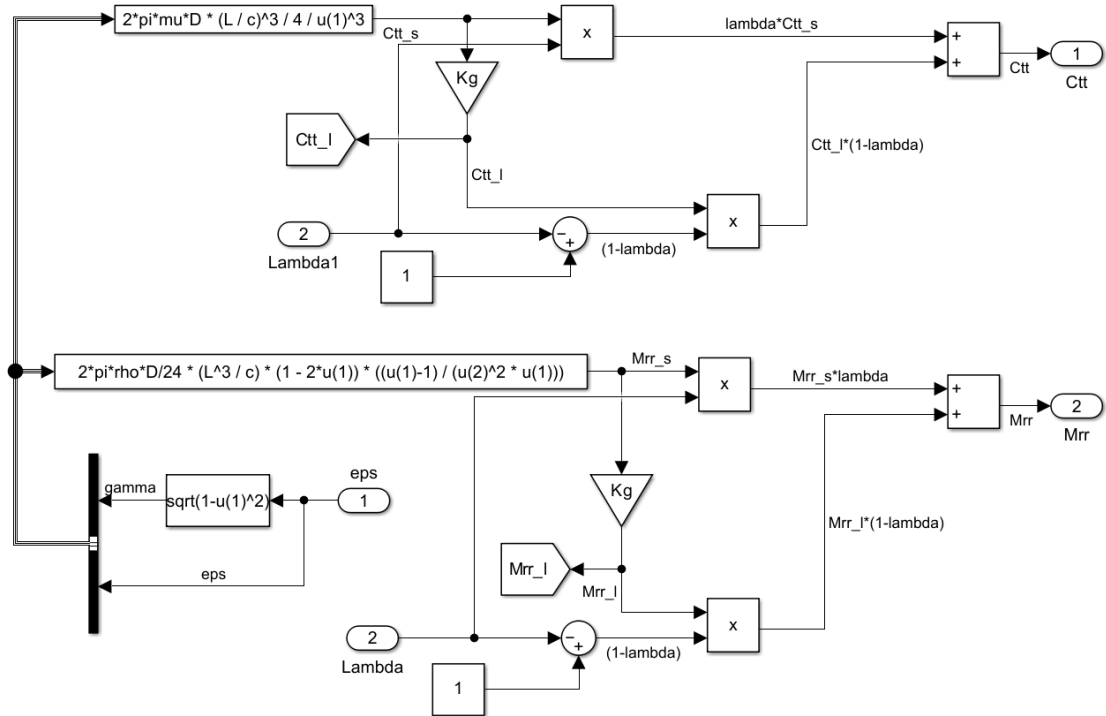


Figure 5.6 Uncavitated SFD coefficient calculation subsystem.

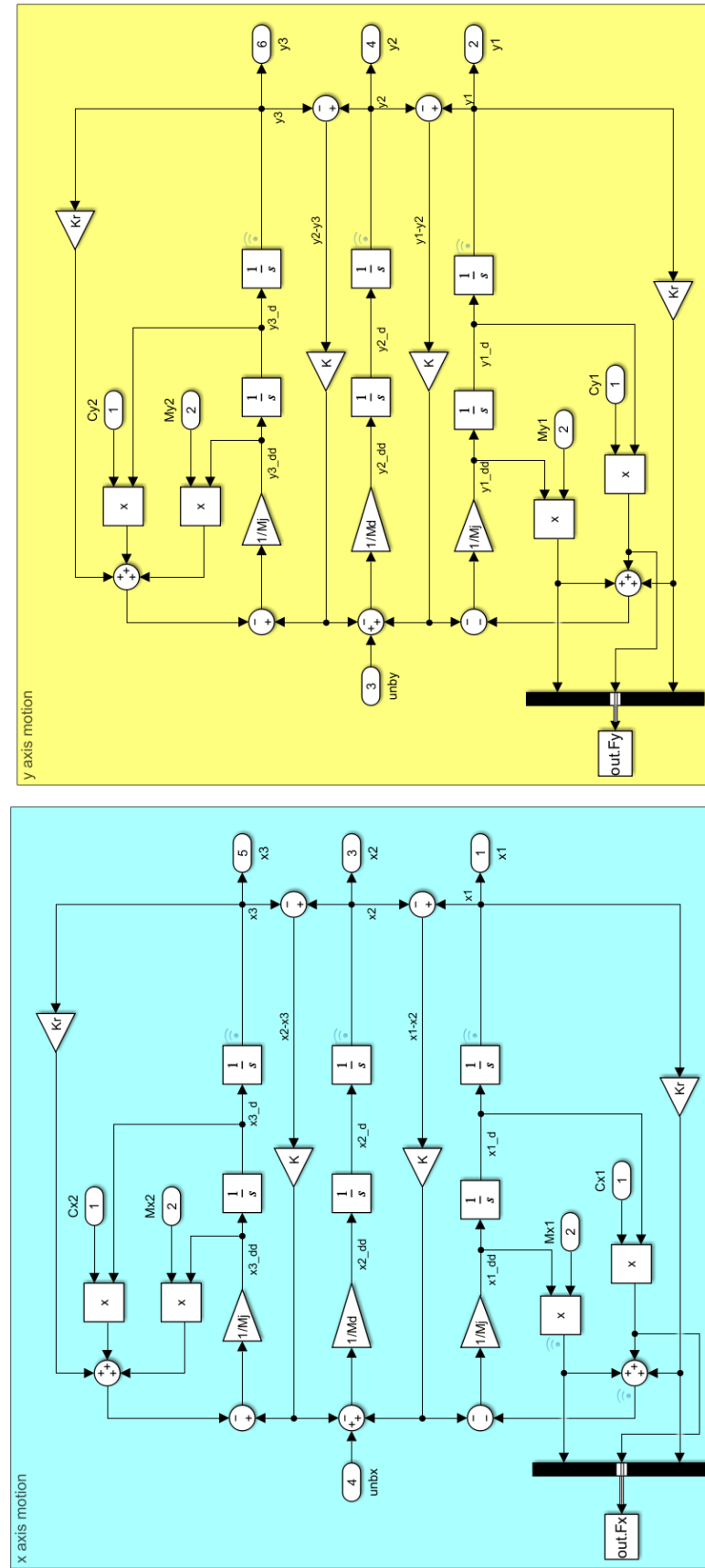


Figure 5.8 Decoupled Jeffcott rotor subsystem.

The dimensionless journal eccentricity calculation that is necessary for controller feedback and SFD subsystem is done as shown below.

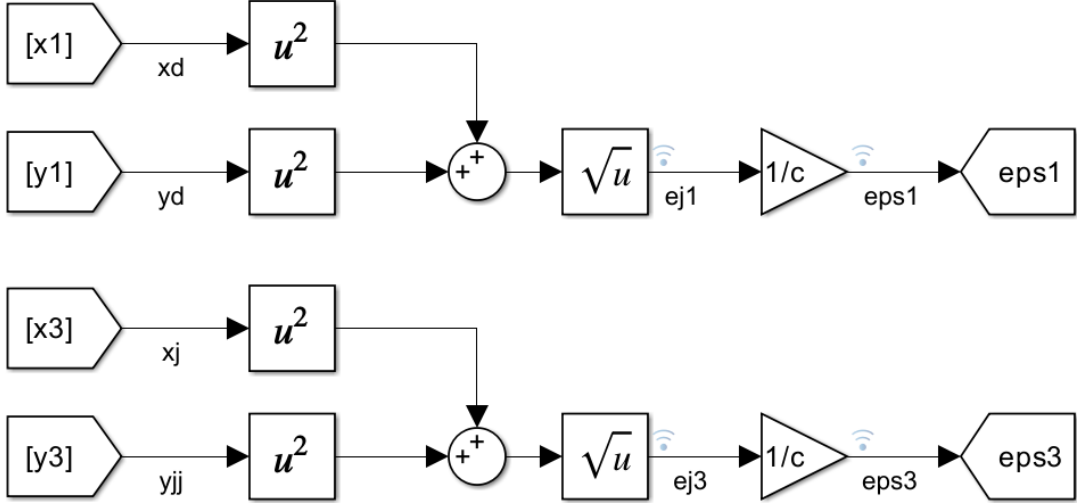


Figure 5.9 Dimensionless journal eccentricity block diagram calculation.

In the model for Jeffcott rotor, we implemented both bearings using a single SFD subsystem due to systems inherent symmetry. The FEM is different in this regard as bearings can and expectedly show different behavior. For this reason, each SFD has a dedicated controller-servo valve-seal ring-SFD system, but the blocks themselves are the same as shown above. The FE rotor model on the other hand is very different. Using the first, internal, and final node generalization derived in Chapter 3 we modelled 9 building blocks for the 3 cases as disks and bearings can be placed at any node on a rotor. For modelling the HP spool, we must have blocks for:

- Starting node with SFD
- Internal node without SFD or disk
- Internal node with compressor lumped
- Internal node with SFD
- Final node with turbine lumped

In below we show these building blocks and their block diagrams.

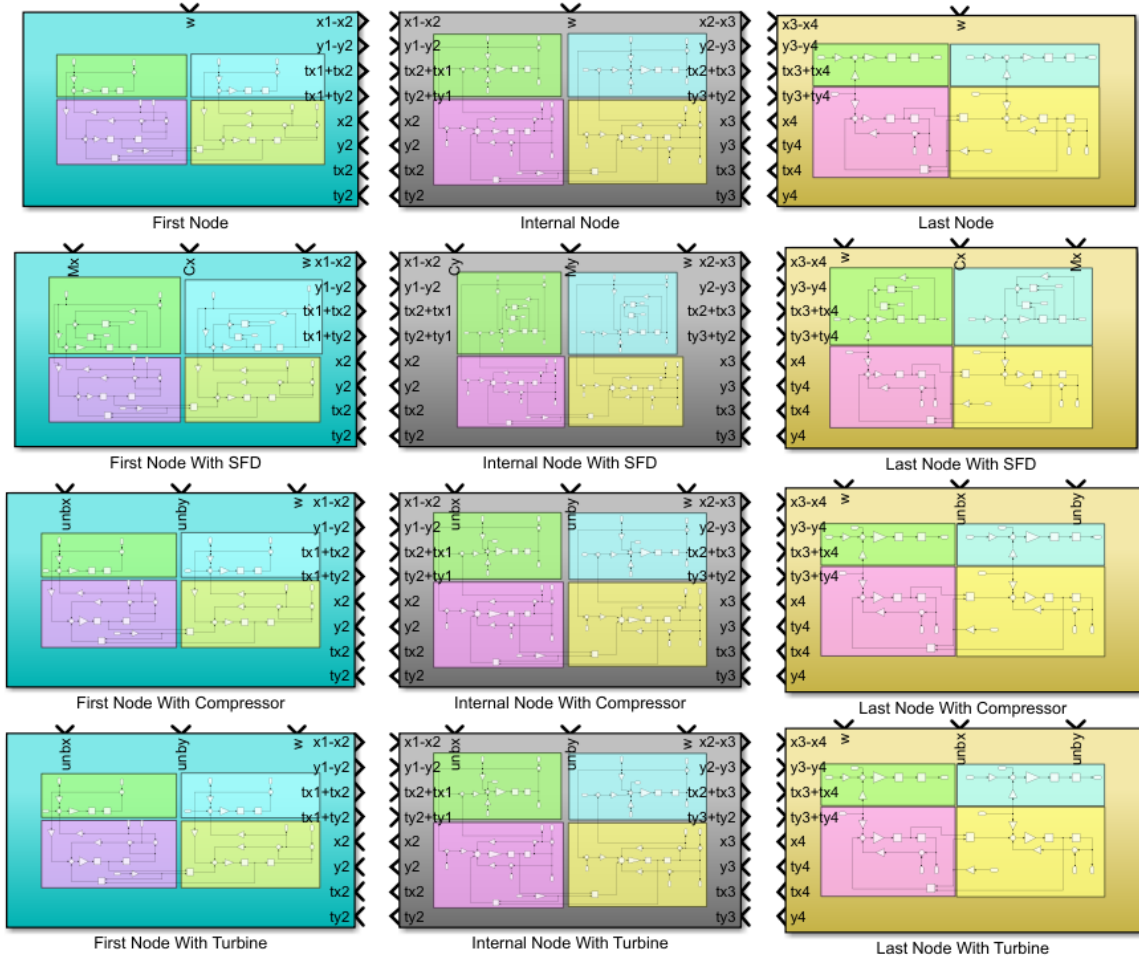


Figure 5.10 Building blocks for the FE model.

Each node has 4 DOF (x, y, θ_x, θ_y). The gyroscopic effect couple subsequent nodes on (x, θ_y) and (y, θ_x) . Connecting a first node to an internal node, and then to a final node gives out the Jeffcott rotor model with gyroscopic effects included. The block diagrams inside the subsystems are given below. The names for block inputs except the first and second node are only representative, as the number of subsystems from initial node determine the node number. Below we show 3 selected subsystems for the 3 node conditions and the 10 element HP spool model.

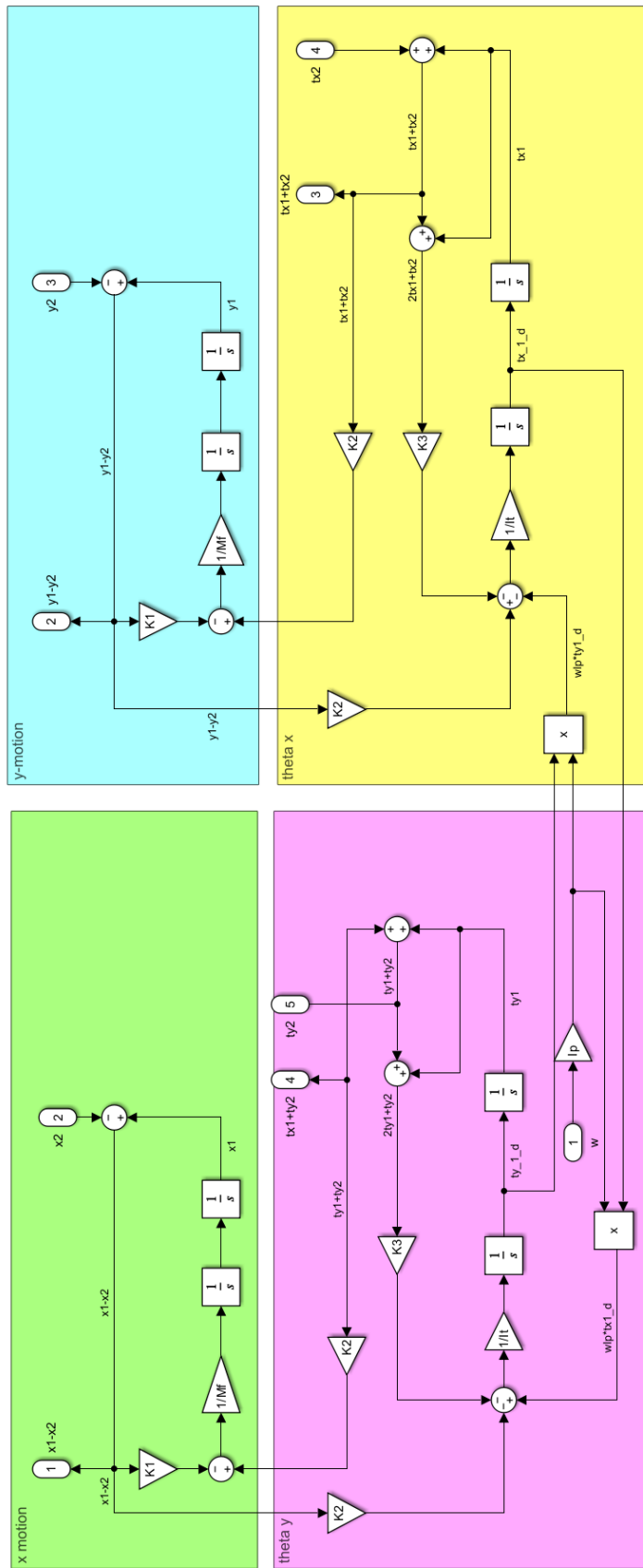
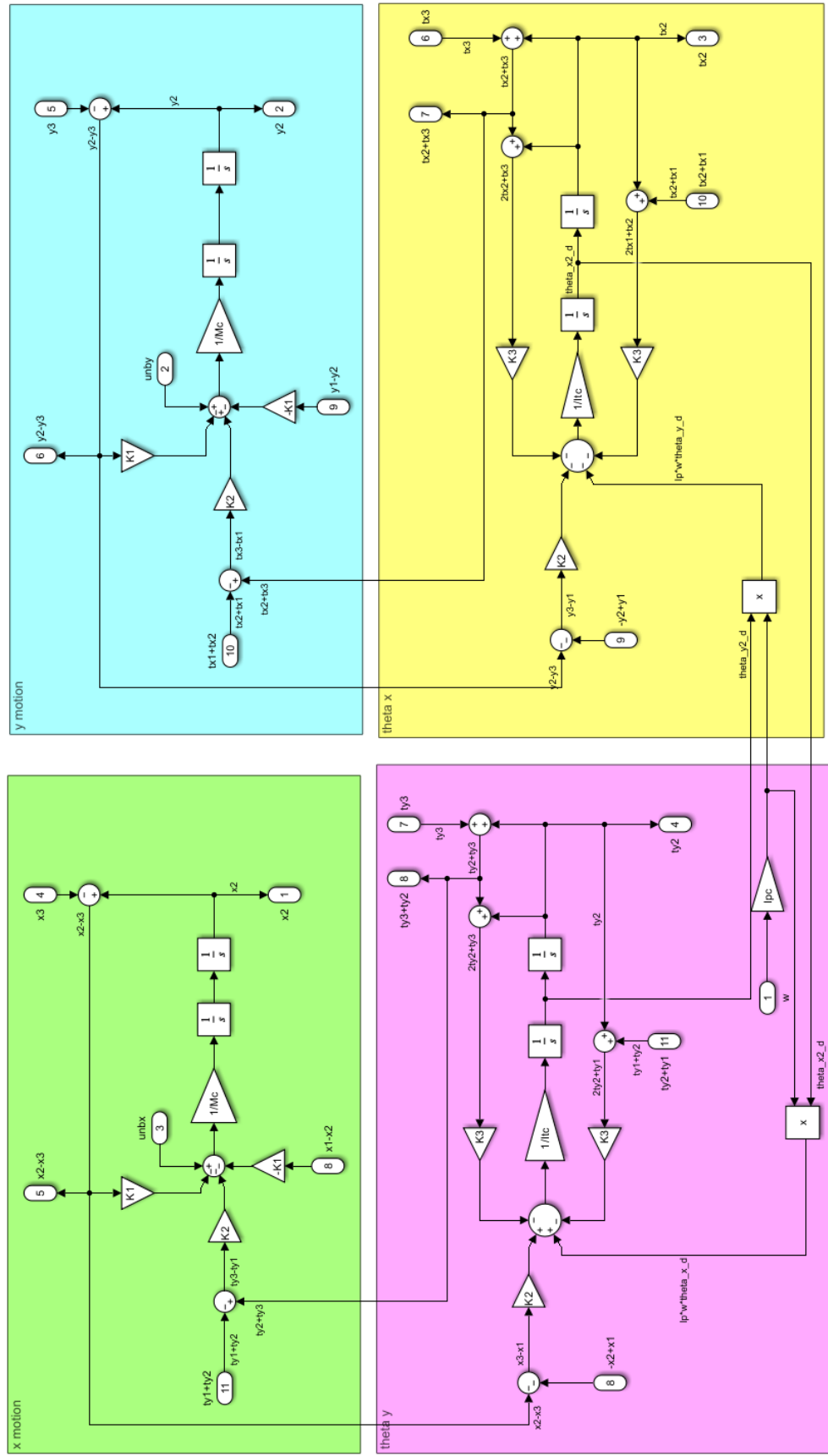


Figure 5.11 First node without disk or SFD.

Figure 5.12 Internal node with compressor.



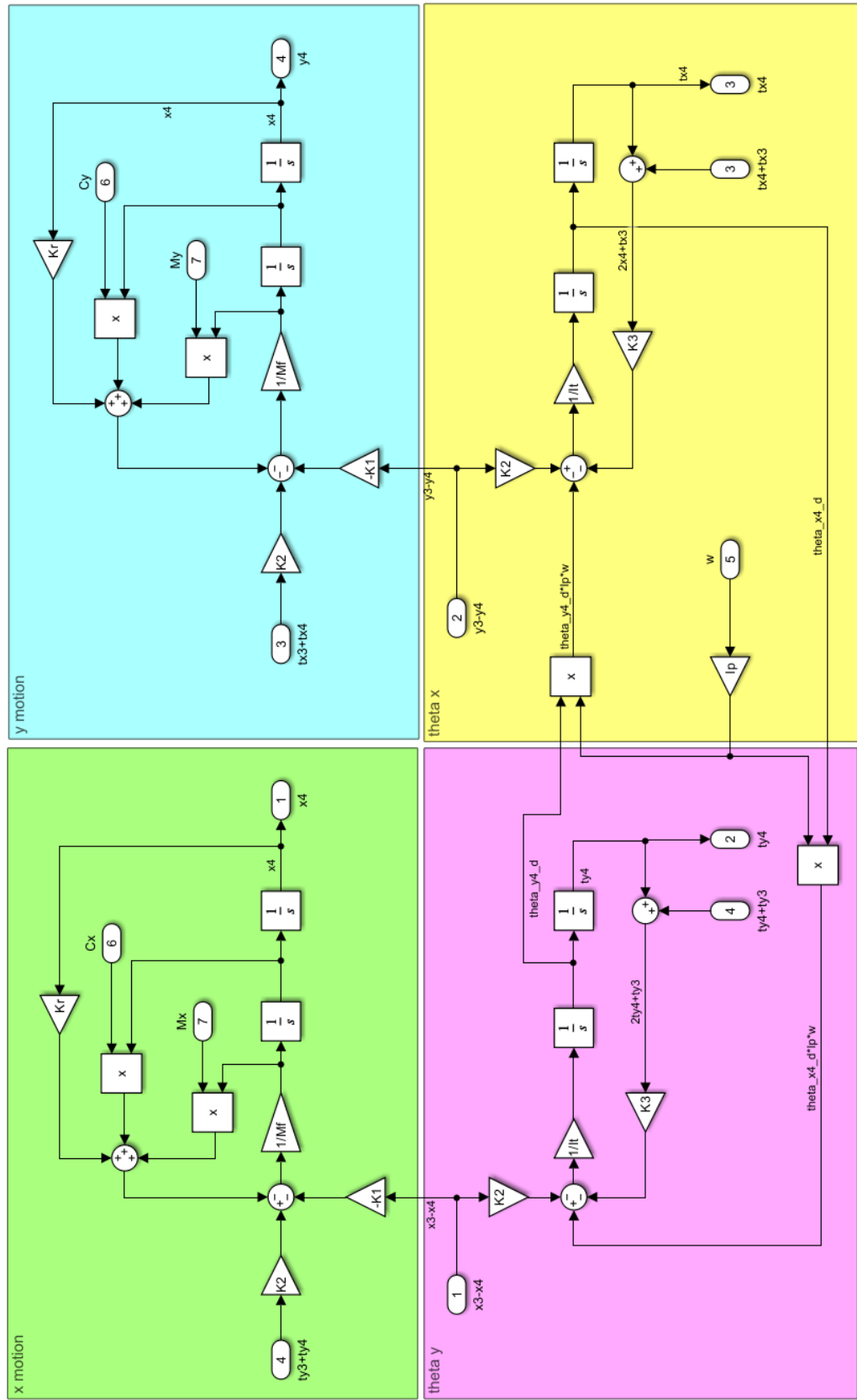


Figure 5.13 Final node with SFD

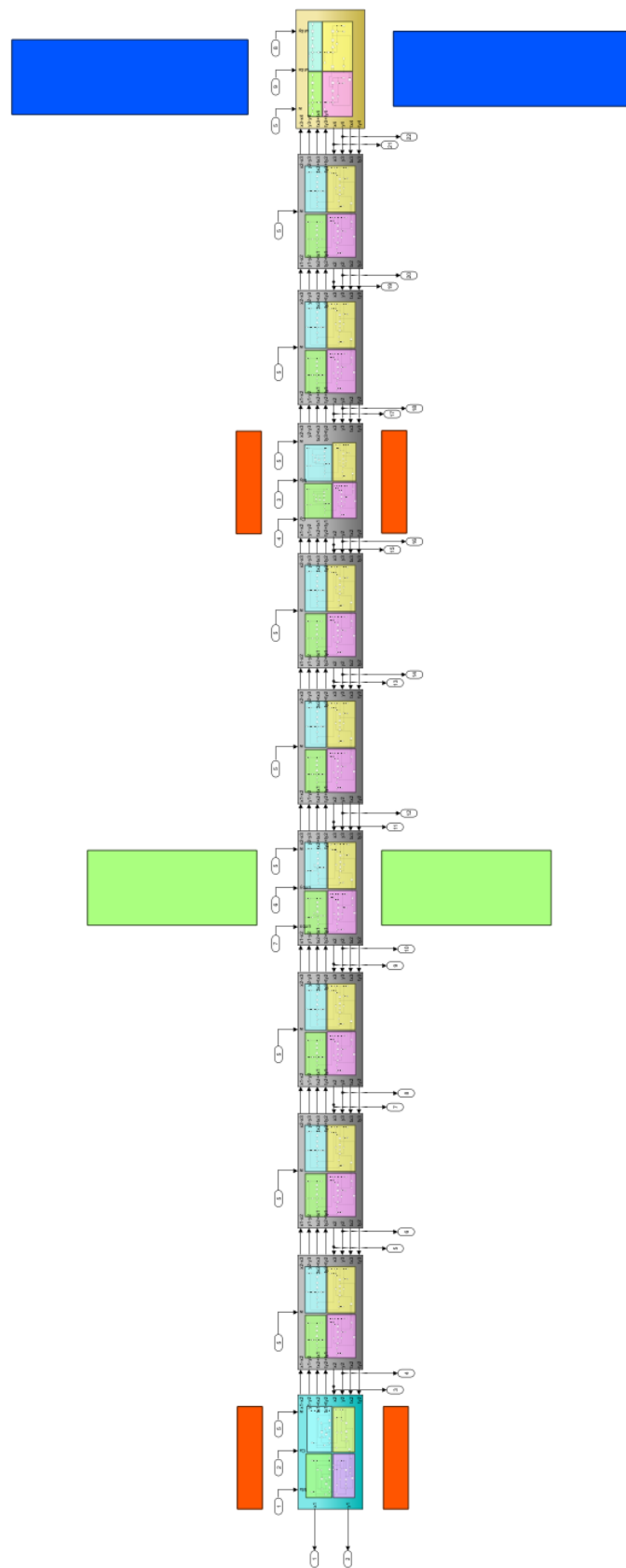


Figure 5.14 The 11 node HP spool model.

5.3) Controller Design

A controller is the machine brain of a system that governs output using actuators considering the error between measurement and reference. The most common controller type used in the industry is the proportional-integral-derivative controller and its variations. It uses the combination of the past, present and estimated future errors for changing the system dynamics. Depending on the system P, PI, PD, or PID scheme is used. The PID controller transfer function is:

$$G_c(s) = K_P + \frac{K_I}{s} + K_D s \quad (5.15)$$

The controller parameters K_P , K_I , and K_D are tuned for design specifications like reference tracking and disturbance rejection. The advantage of the PID controller is its easy implementation and easy tuning. Generally, engineering systems operate around linearized points and tuned using the most basic applicable models. The rotor-SFD-servo valve system is modelled using linearized film coefficients (up to a certain eccentricity), decoupled rotor equations (for Jeffcott rotor model), and a finiteness measure that defines a linear relationship for seal position and damper modes.

For this reason, the next step from the basic on-off controller that works in a predetermined way is implementing a PID controller scheme. In simulations we could not achieve good results when derivative control was included. For this reason, P&PI controllers were tried for implementation. Even though the plant is modelled using linearizing assumptions, the coupling between the subsystems makes linearizing full body of governing equations problematic. Also, as the controller output actuates seal ring to give a normalized (between (0,1)) output to SFD subsystem, the linearization point is not very clear. For the HP spool carried by semi active SFDs, it is a must to have stable operation in both pure SD and pure LD configurations in run up, up to 8000 rpm. Therefore, we deduced as long as the controller does not induce high frequency oscillations to seal ring, gains could be tuned by trial and error comparing lambda and journal eccentricity plots.

In overall, the tuned controller should be responsive enough to journal position so that the vibrations at critical speeds are attenuated by increased damping coming from the SFD end condition and after the rotor passes through critical speeds end condition should return to SD mode. It should be noted that it is not necessary to move seal rings all the way through journal end, as long as the amplitude of vibration at critical speeds is decreased, the semi active SFD improves the

passive SFD by keeping the advantages of both end conditions. The SFDs used in both Jeffcott model and FEM are exactly same, for this reason the gains are tuned using the Jeffcott rotor model.

For all simulations we used Simulink ode45 solver with options set auto. During parameter tuning and semi active response we used a run up ramp slope of 100 rad/s. On the figure below the PI output signal is conditioned so that the servo valve pressure is physically correct. The saturation on the current enables servo pressure to not exceed equilibrium at LD mode, can cause excessive load on the journal. Also, the error to the integral controller is limited by a dead zone (10% of clearance) so that the current output is not built up.

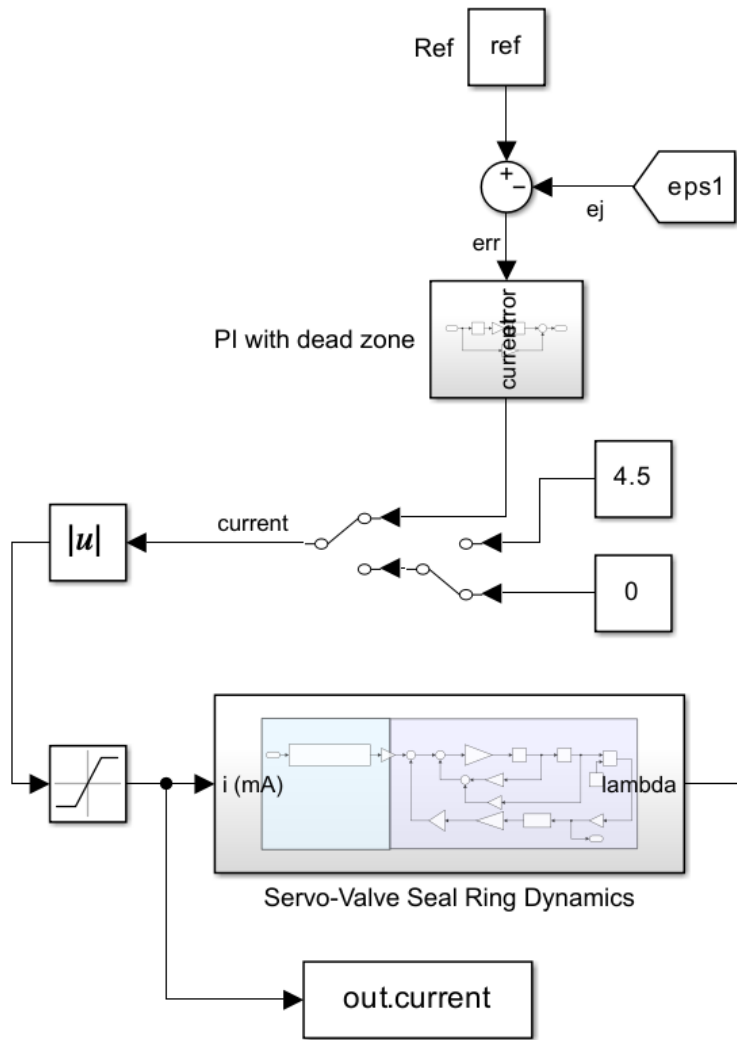


Figure 5.15 Controller implemented servo valve seal ring subsystem.

6) SIMULATION RESULTS

In this chapter simulation results for the Jeffcott rotor model and FEM rotor model are given. The results show how bearing condition affects journal critical speed, rotor modes, disk orbit, modes, and transmitted load during engine run up.

6.1) Jeffcott Rotor

6.1.1) Jeffcott Model Open Loop Simulation

The open loop system simulation includes SDF SD ($\lambda = 1$) and LD ($\lambda = 0$) conditions that can be obtained by current input or direct seal position input.

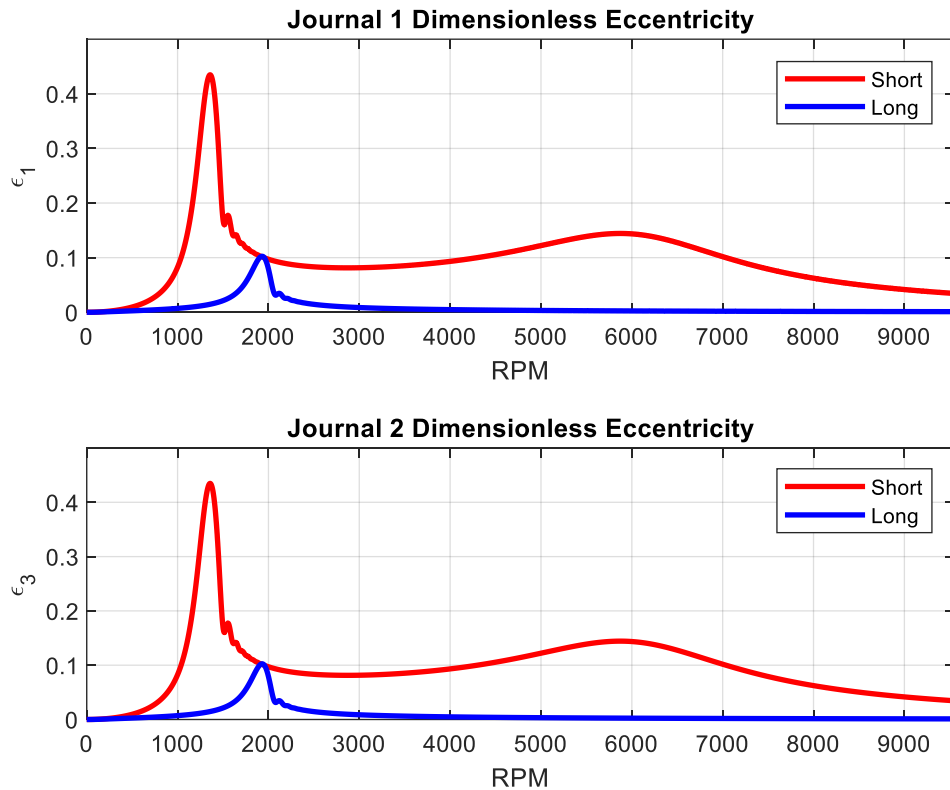


Figure 6.1 Dimensionless journal eccentricity during engine run up.

Figure 6.1 shows two critical speeds for the LD around 1200 rpm and 6000 rpm and a single critical speed for LD around 1900 rpm. As expected both journals show the same behavior as the model is symmetric. The damping provided by the SD mode causes higher orbits at critical speeds. The critical speed differ due to added fluid inertia as discussed in Chapter 2.

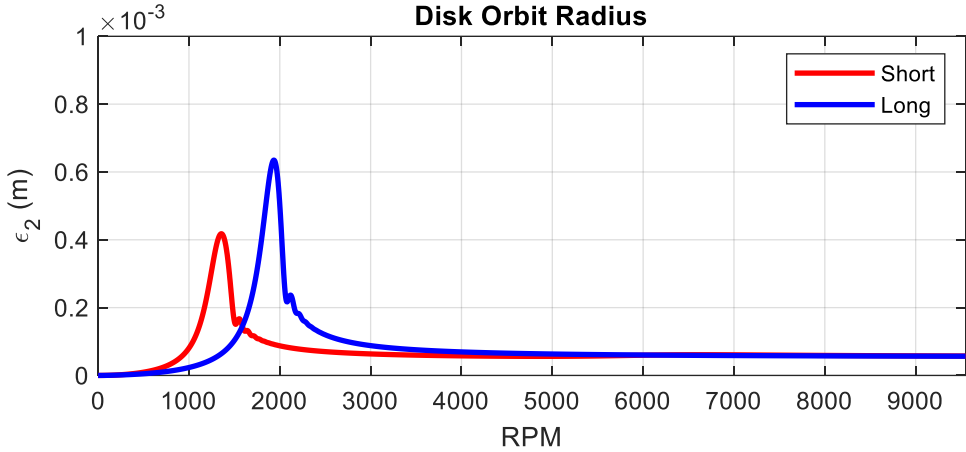


Figure 6.2 Disk orbit radius during engine run up.

Figure 6.2 shows a drawback of the LD mode. The disk orbit radius in LD mode at the critical speed is nearly 50% higher due to increased damping at the supports. Since we have the node positions over run up, we can extract modes of vibration at critical speeds as shown below.

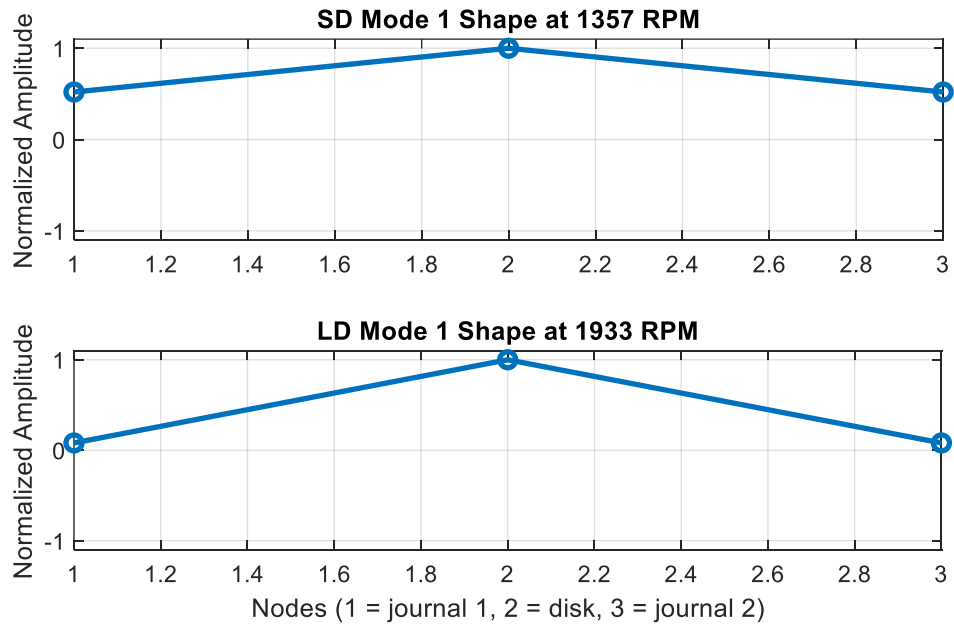


Figure 6.3 Mode shapes for SD and LD configurations.

The modes of vibration shown in Figure 6.3 coincide with symmetric Jeffcott model assumptions. The transmitted is found by summing the individual force components of the damping, inertia and stiffness at the supports. The LD mode shows a higher peak transmitted load value due to increased damping.

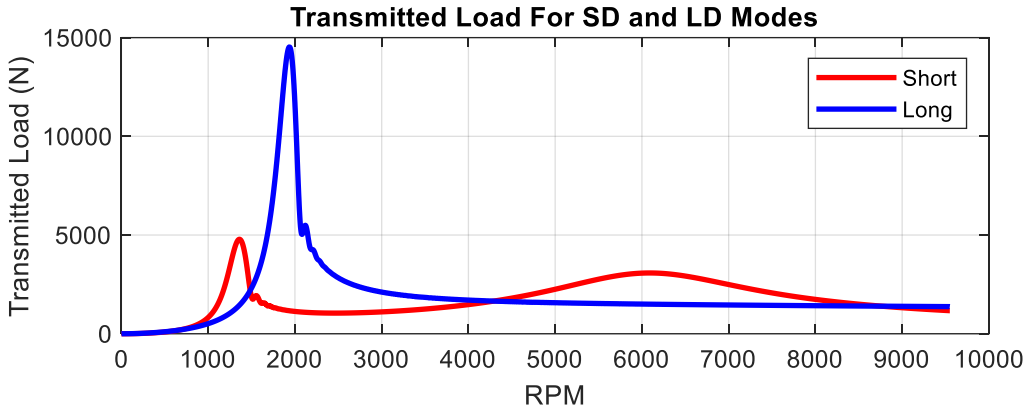


Figure 6.4 The transmitted load during run up

While run up, the simulation sweeps rotational speed values over a range of values, for this reason they don't represent the steady state response. The figures above show that at the operation speed SD mode orbit is much larger compared to LD mode but is near the limit of linearized equations. (see Chapter 2). The transmitted force on the other hand is 12% smaller, which is a great improvement.

6.1.2) Controller Tuning

The controller connected to the SFD with movable seals, does not directly affect journal position. It influences the vibration absorption capability of the bearing (i.e. damping) in accordance with the severity of vibration amplitude at that instant, from the difference between the instantaneous journal position and reference. The overall performance depends on both operating speed and reference input as the orbits would be directly influenced by damping for each steady state operation speed. For this reason, the supplied reference changes the feedback response. This is why we call the controller implemented feedback system semi active.

In our simulations we decided to keep reference 0 as we want controller to only focus on vibration attenuation. Also, as mentioned, the current to the servo valve must be limited. We selected the saturation current as 15 mA as it is common practice to limit maximum pressure when using servo valves in fluid circuits. In figures below run up sweep as K_p and K_i increase between 50 and 150, and 0 and 12 are shown.

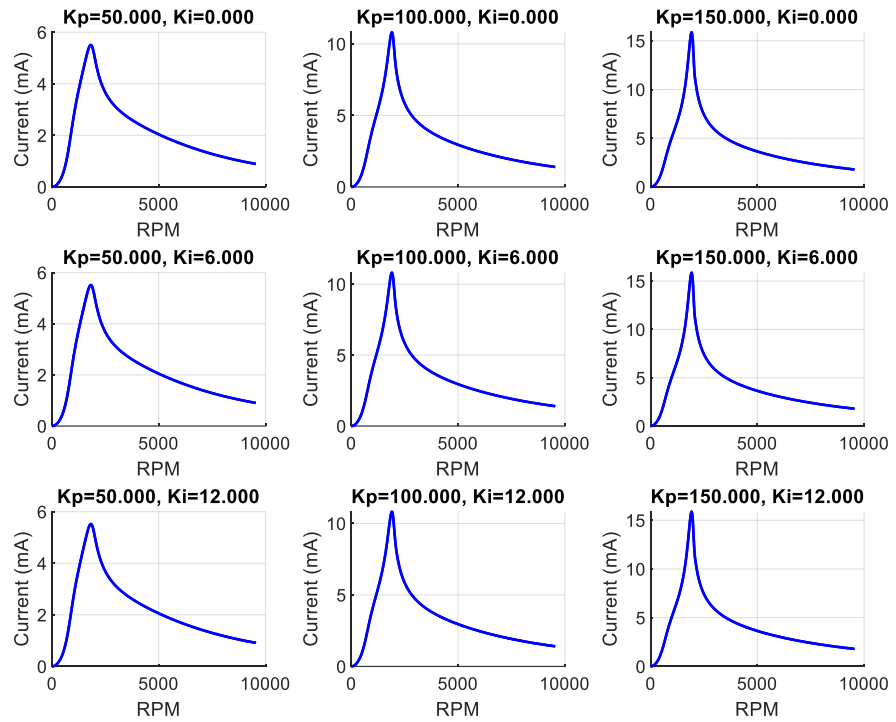


Figure 6.5 Servo-valve current for various controller gains.

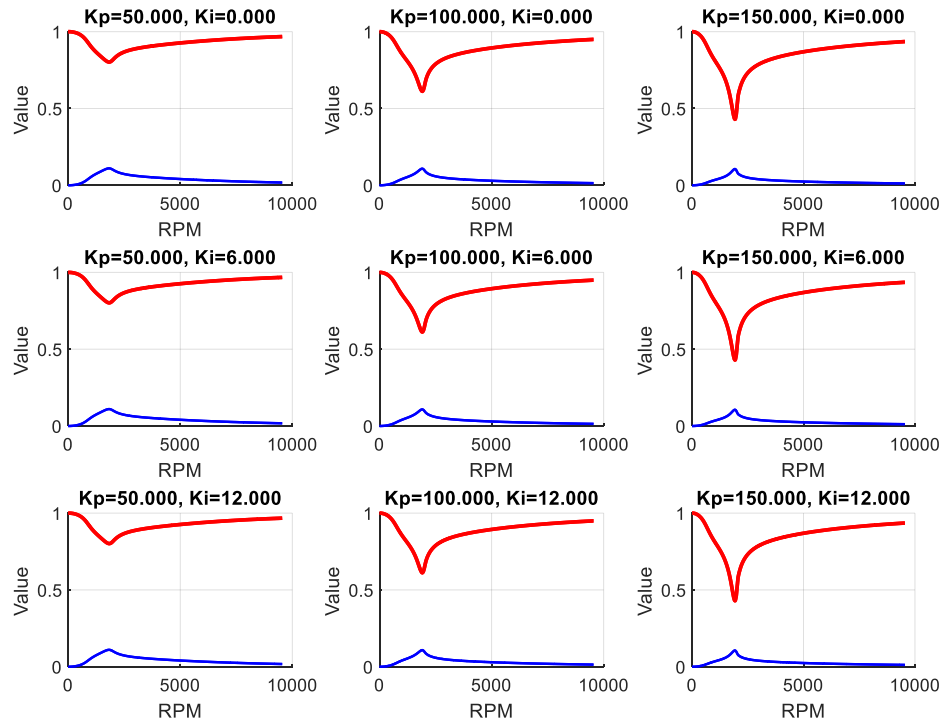


Figure 6.6 Journal and seal position over run up with control.

For testing the controller, we added disturbance event that cause the overall center of mass of the disk to shift 100% by simulating a step by setting ramp initial value and slope.

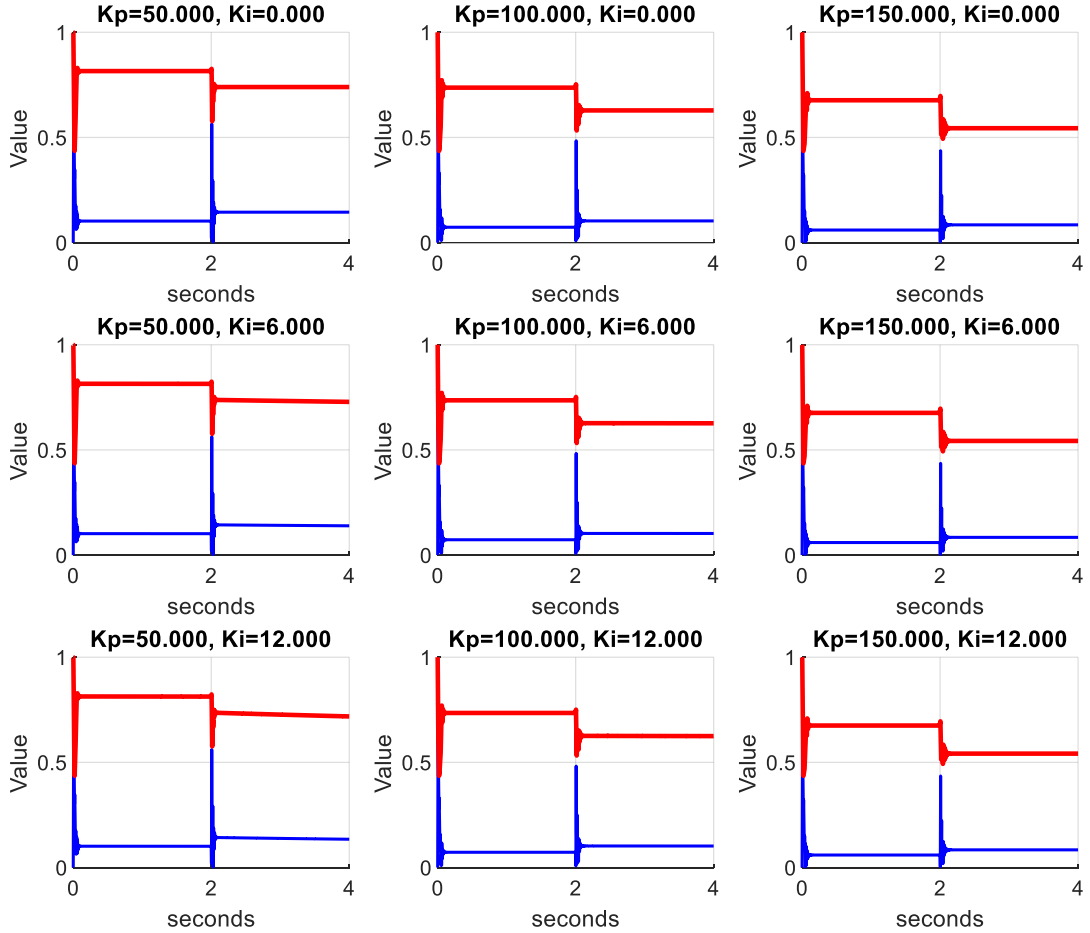


Figure 6.7 Controller disturbance reaction.

The journal position shows that all nine controllers lower the journal position from 40% of clearance to nearly 10 % of clearance. In the LD mode, the journal position was just below 10% of clearance. Therefore, even if the seal ring is further pushed on, it is improbable to further lower journal amplitude. In the Jeffcott rotor we saw that a close ended SFD leads to higher transmitted force and disk orbit. Hence, the selected controller should be able to attenuate vibration without too much damping increase. Also, it should neither saturate easily as saturation breaks the linearity of the controller, nor output too low of a current as servo valve would not be able catch on to small increases of current. The current time plot below shows the current change for a disturbance (shown above.) input.

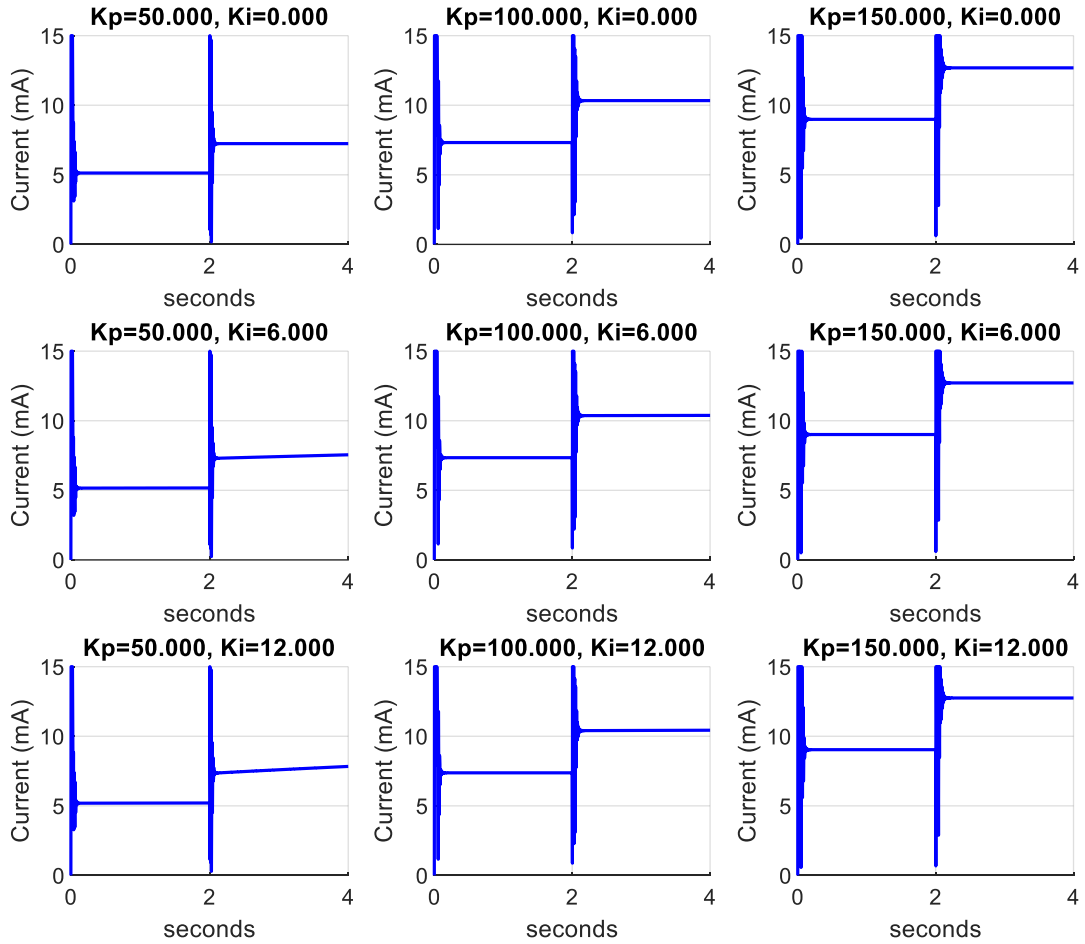


Figure 6.8 Controller output current for different gains.

For our system, the steady state error is always larger than zero. To combat integral windup, we added a dead zone below 10% eccentricity to the integral controller. This approach resulted in better steady state behavior that limited integral build up for low K values. Compared to the passive SFD both P and PI controllers show improvement. For this reason, we selected $K_p = 100$ and $K_i = 6$. The PI is used for slowly increasing damping over time so that journal eccentricity decreases to the dead zone threshold.

6.1.3) Jeffcott Model Closed Loop Simulation

In the closed loop Jeffcott rotor model journal eccentricity and dimensionless seal position below, compared to the open loop SD, the maximum eccentricity is 10% of the clearance without going fully into LD mode.

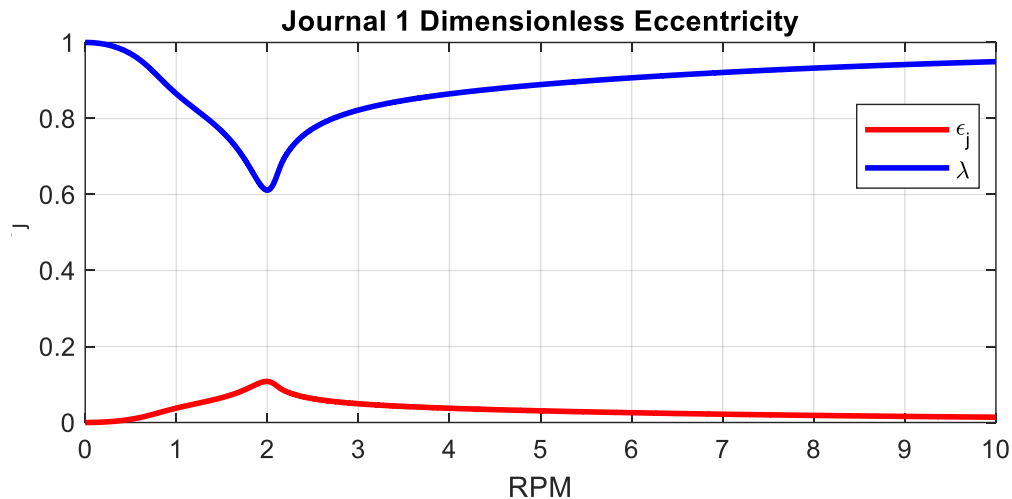


Figure 6.9 Closed loop Jeffcott rotor model journal eccentricity

An advantage of the mid-seal position can be seen below in the disk orbit radius plot. The maximum disk orbit is nearly 50% less than the LD mode, but the journal eccentricity is at a similar level.

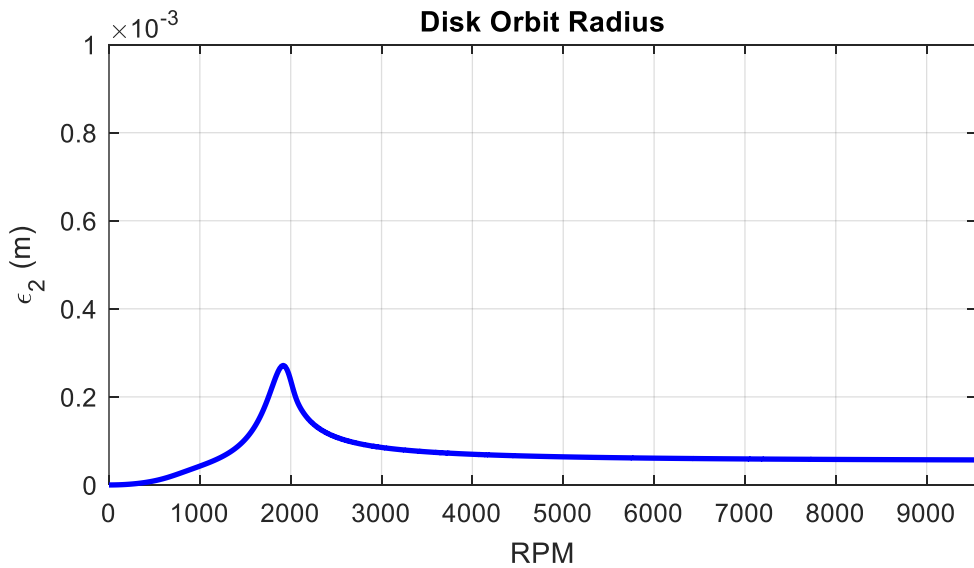


Figure 6.10 Controlled Jeffcott rotor disk radius

The close loop servo valve current plot below was already shown in Figure 6.6. Comparing the journal eccentricity with current we see that as orbit gets smaller the current slowly decreases. This is expected since the error that PI develops the current is derived from the journal position.

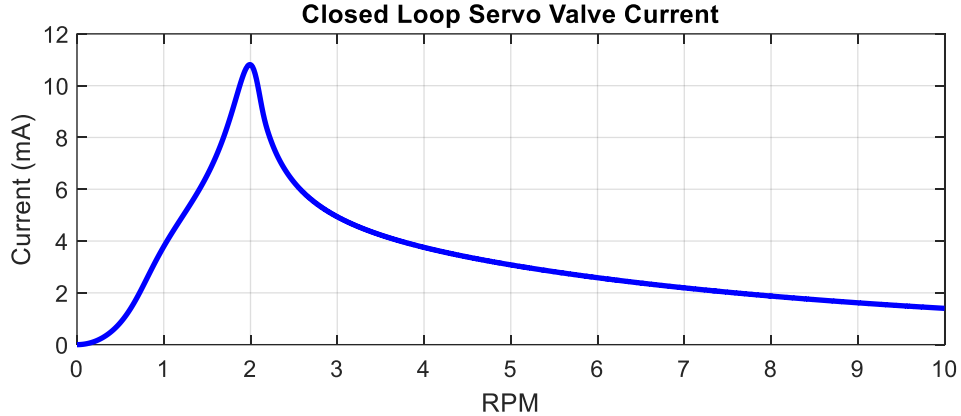


Figure 6.11 Servo valve current over run up.

Mode shape plot below shows an interesting result. The feedback system's mode shape and critical speed is very similar to the LD configuration. This result is due to the system behaving similar to a LD SFD near critical speeds. Away from the critical speeds, the orbit plot and mode will behave more like the SD SFD.

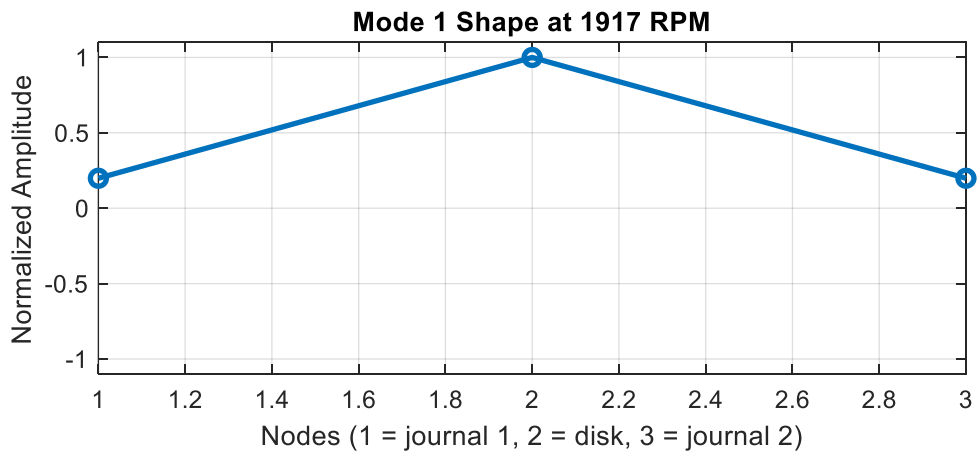


Figure 6.12 Controller rotor mode shapes.

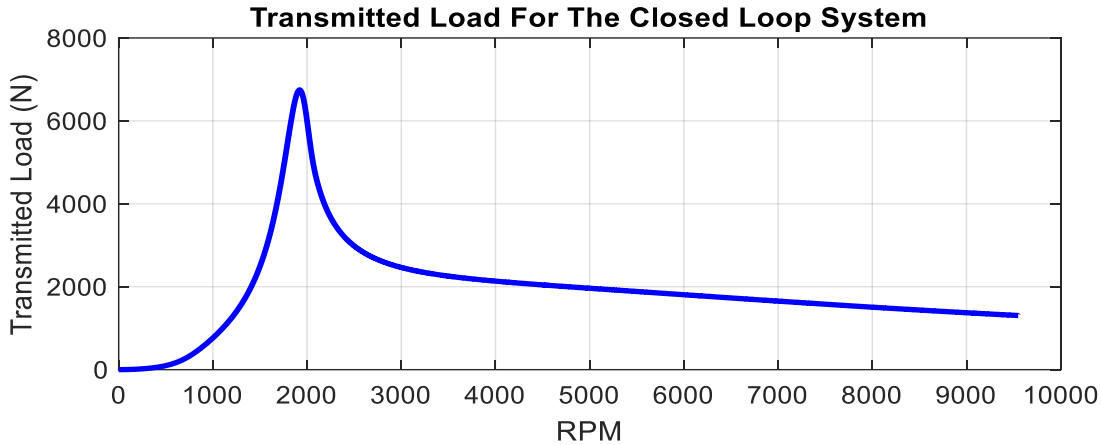


Figure 6.13 Transmitted load over run up.

The disturbance which was mentioned in the controller tuning section can be applied to the feedback system to showcase how other parameters such as transmitted load and disk orbit get affected by it. The disturbance simulates a center of mass shift at the compressor, equal to the original center of mass imbalance. Since the Jeffcott model has lumped disks, we used 50% of imbalance shift as an outside event that disturbs both turbine and compressor is improbable (aside from catastrophic failures which the controller would not help).

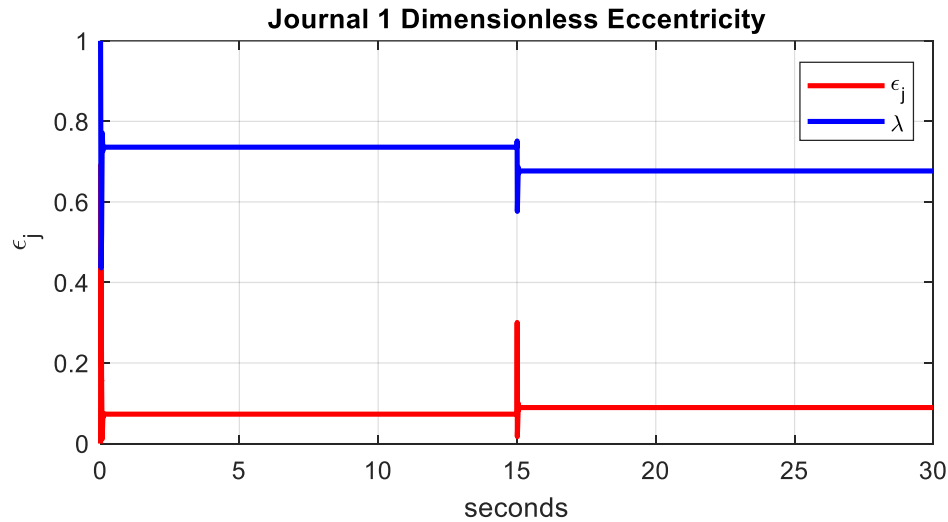


Figure 6.14 Journal eccentricity in disturbance test.

The disturbance that applies at 15 seconds is quickly attenuated and as shown above as the journal orbit increases 15% the seal ring position decreases 8% after the transient.

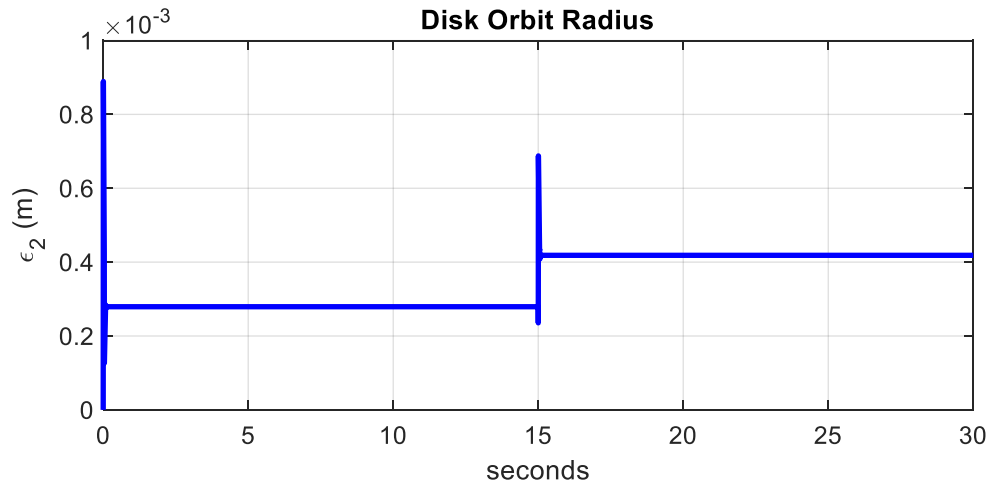


Figure 6.15 Disk orbit change after disturbance.

The disk position as shown above increases 50% caused by disturbance directly affecting it. The PI output increases 22% after hitting saturation until transients die.

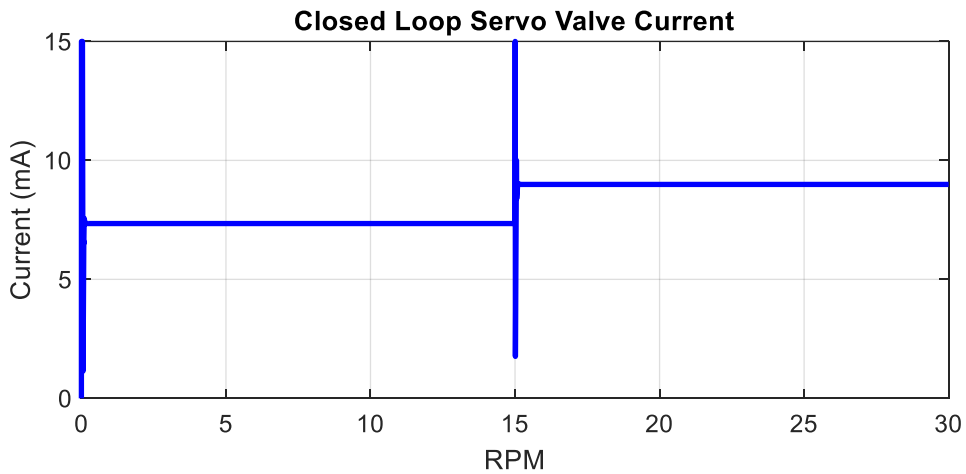


Figure 6.16 Controller output current change with disturbance

Overall, the Jeffcott rotor the journal eccentricity is below 20% of clearance, which was previously pointed out to be a region where linearized CCO equations could be safely applied. So, in, addition to having advantages of the passive SFDs (LD & SD) the semi-active SFD also makes the overall run up behavior predictable.

6.2) FE Rotor

6.2.1) FEM Model Open Loop Simulation

The open loop journal eccentricity for short and long SFD configurations is shown below. In contrast to the symmetric model, the FE model shows asymmetric journal behavior.

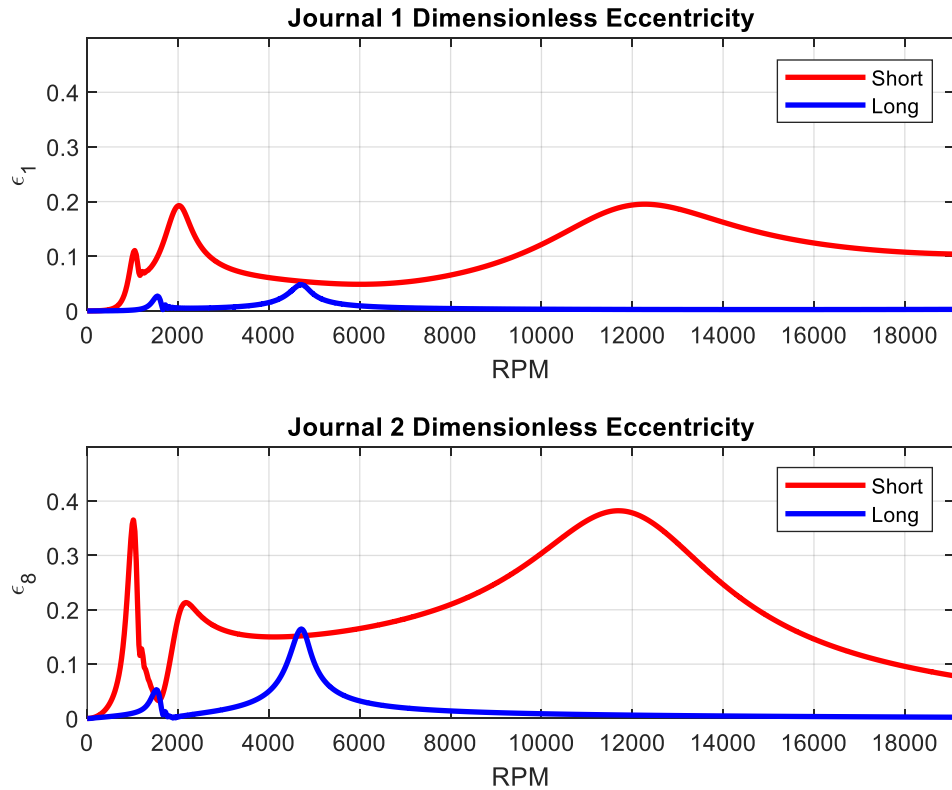


Figure 6.17 FE model open loop journal eccentricity for SD and LD modes.

In both subplots, the short damper mode has two close peaks that arise from the anisotropic stiffness applied to subsequent nodes due to the gyroscopic effect. We showed this during the derivation of the 2 element FE model in Chapter 4. Also, the system shows multiple critical speeds as expected from a two-disk model.

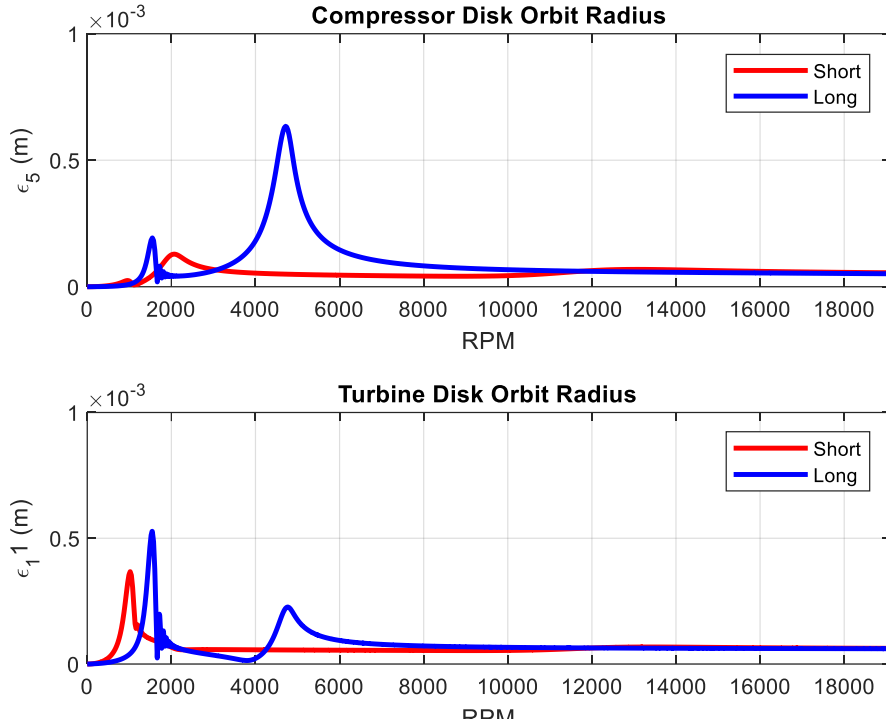


Figure 6.18 Disk orbit difference for SD and LD modes.

In the previous section we showed that the disk is expected to have a larger orbit radius in LD mode which is similarly shown in the figure above.

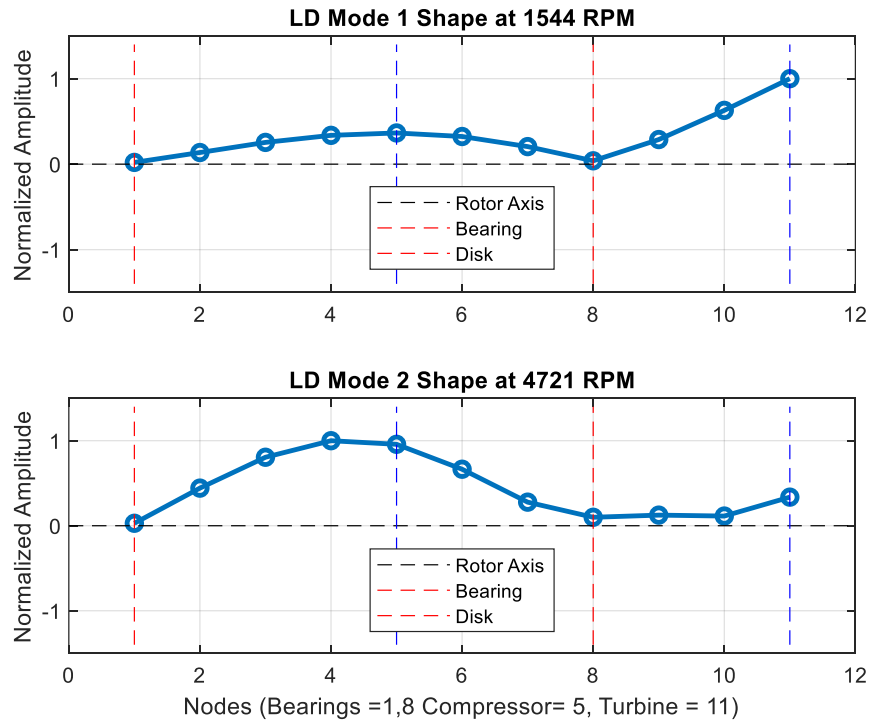


Figure 6.19 LD mode shapes.

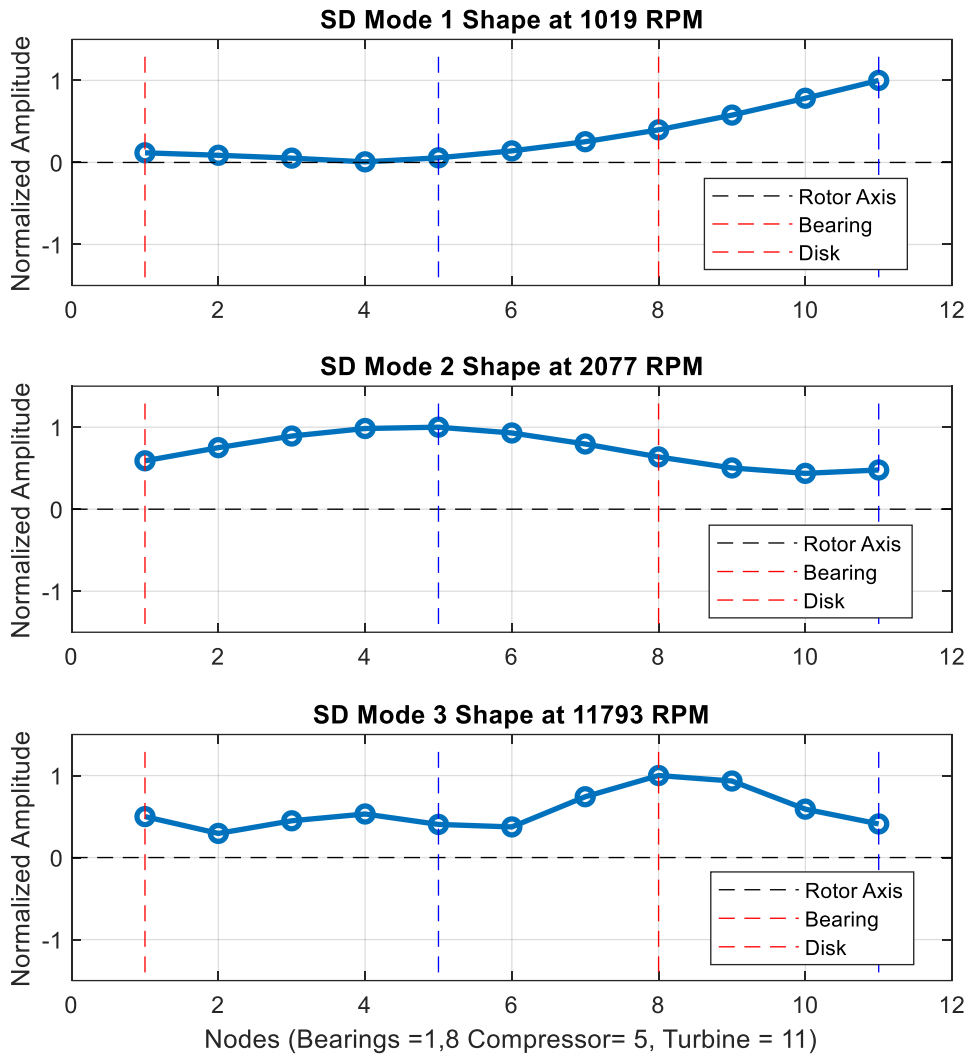


Figure 6.20 SD mode shapes

Mode shapes for the SD and LD conditions, have much richer behavior compared to the symmetric Jeffcott rotor. The peaks identified by our code show 2 critical speeds for the LD mode and 3 critical speeds for the SD mode. The Jeffcott rotor and the FE model show +300 rpm difference in critical speeds. This can be sourced from neglecting taking unsymmetrical center of mass of the turbine and compressor disks which is near to the second bearing at the center. Mode shape at the first critical shows larger turbine motion for both in both configurations as shown from the first mode shapes. Also, the third critical speed seen only in the SD bearing is a damped critical, that has been attenuated by the low SD damping coefficient.

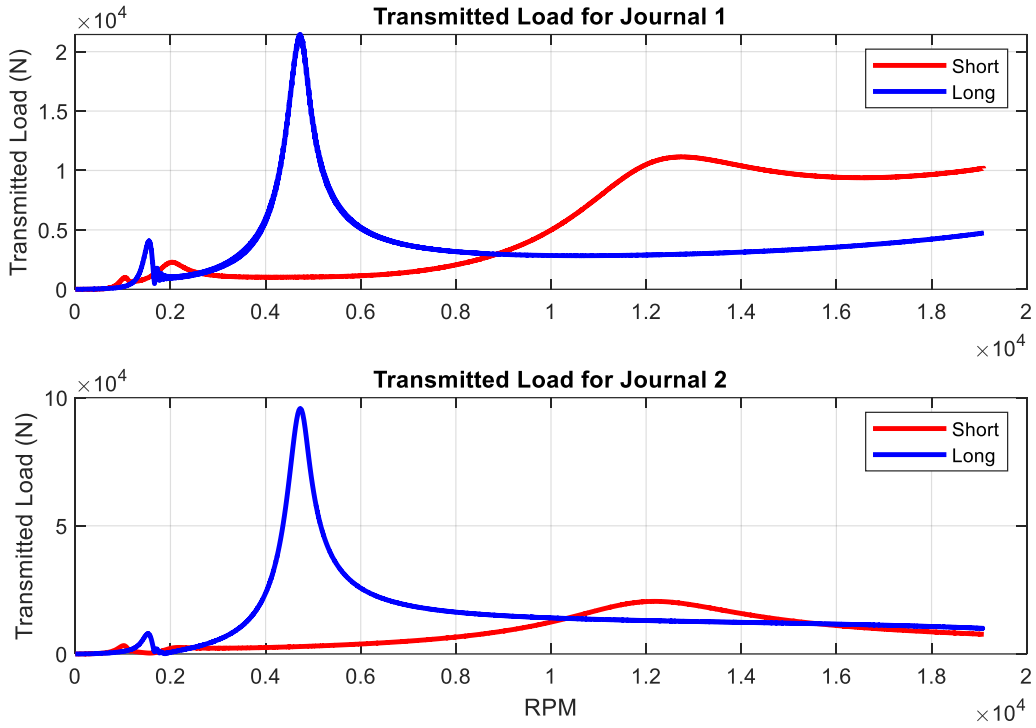


Figure 6.21 Transmitted force difference in LD an SD modes.

The transmitted force subplot for the second bearing shows nearly 100kN force applied to its housing and supporting structure. Considering that the cylindrical bearing we selected (rated 260 kN), only with this radial load, the factor of safety is 2.6, Compared to aircraft industry practice (minimum 4) this value is not acceptable. Therefore, limiting the semi-active bearings LD side by keeping controller gains low, is a good choice. Also, due to the existence of a third critical speed in SD configuration. The transmitted load in SD is much higher than compared to its LD counterpart. Indicating the importance of damping low humping critical, speeds. However, as the operation speed of the N2 spool is around 8000 rpm the third critical is not very concerning for our semi-active SFD.

Using the node position data, we can also plot LRV (node orbits) for selected speeds during engine run up as shown on the next two pages. These plots enable us to easily visualize vibration behavior at various speeds.

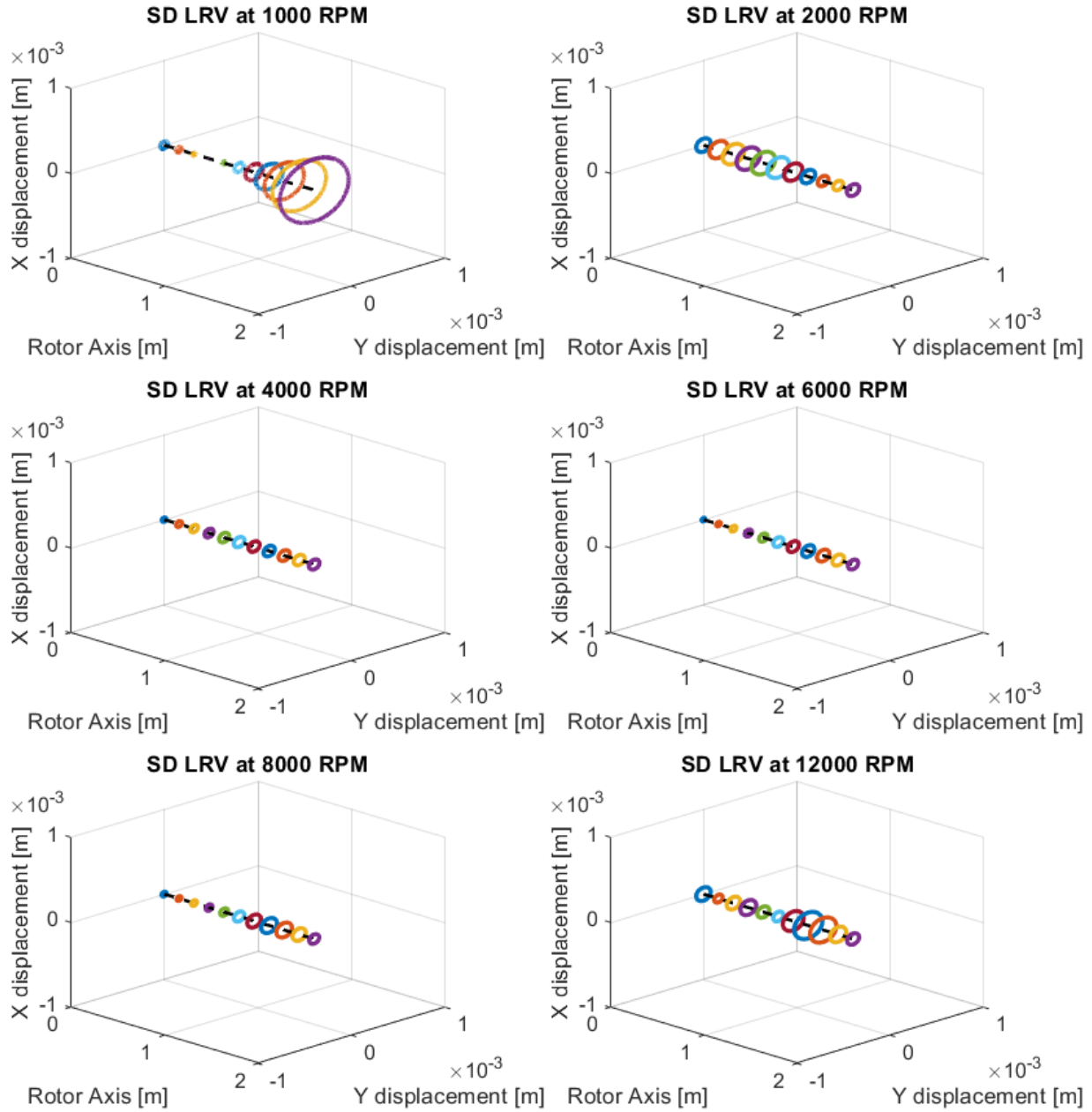


Figure 6.22 LRV plot for the SD mode.

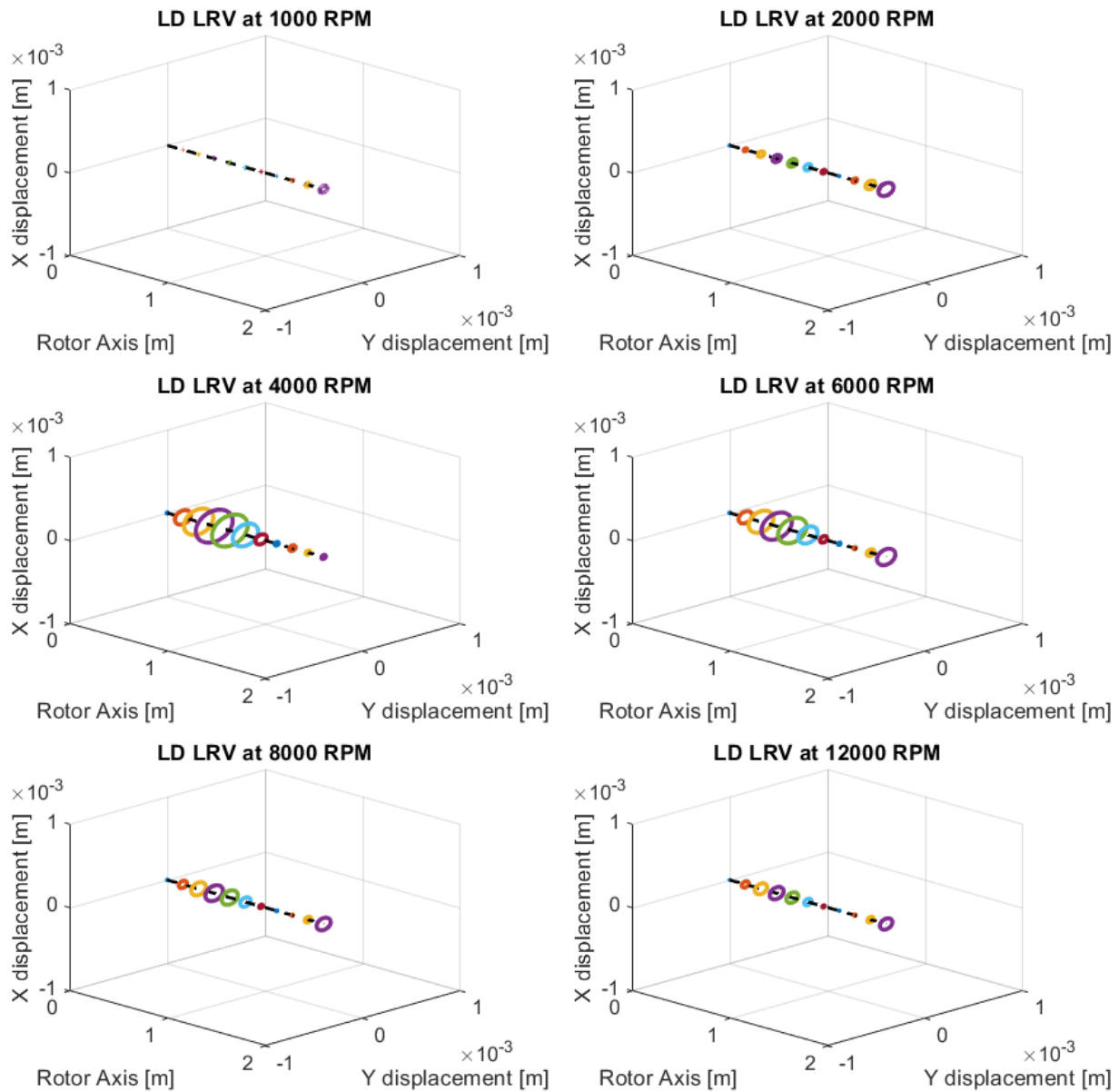


Figure 6.23 LRV plot for LD mode.

6.2.2) FEM Model Closed Loop Simulation

For PI gains of $K_p = 100$ and $K_i = 6$ the close loop dimensionless journal position is shown below. Compared to open loop plant response, the controlled response shows high degree of vibration attenuation without going full LD mode. However, as mentioned in Chapter 4, the geometric ratio for L/D equal to 0.25 is 48. Therefore, the increase is still significant. Also, the hump like critical speed at 12000 rpm is overdamped.

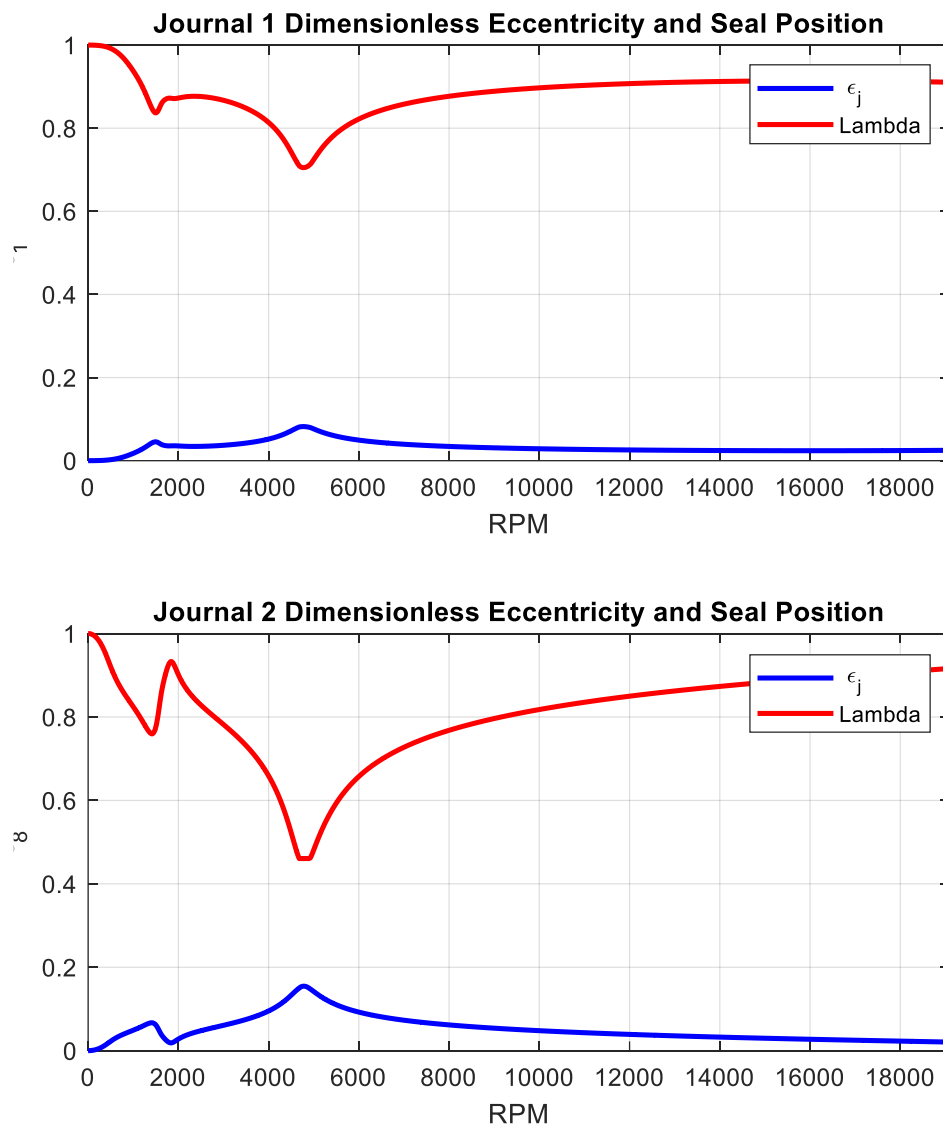


Figure 6.24 Controlled FE model rotor journal eccentricity.

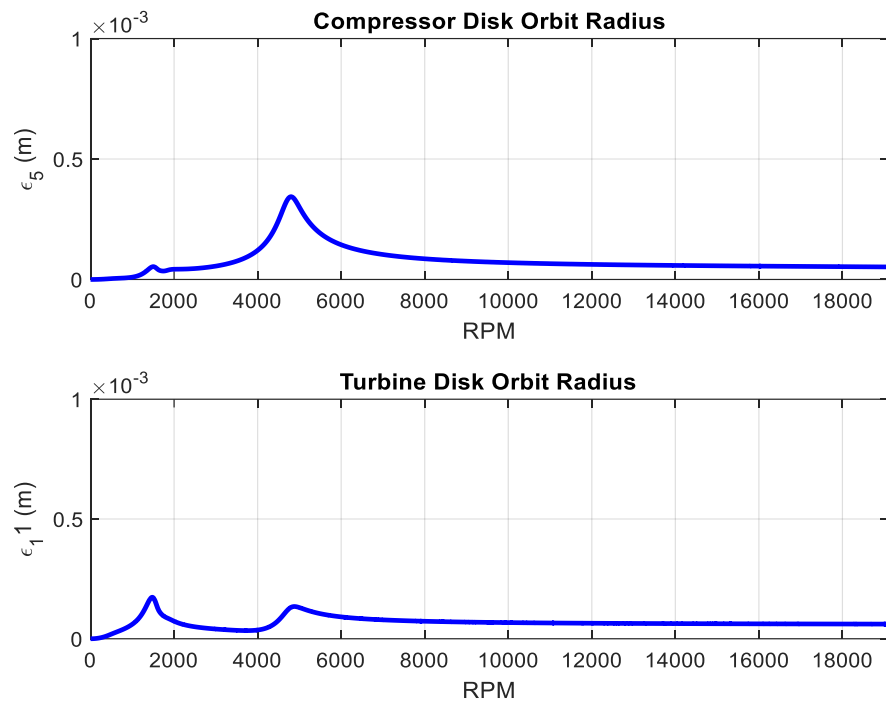


Figure 6.26 Closed loop compressor disk radius.

The figure above shows that the increased damping of the second bearing causes disk orbit to be in between the two distinct configurations. Considering the amplitude at the first critical we expect the turbine disk to whirl at a larger orbit. The mode plot at the first critical speed shows this to be true. Also, it can be noticed that the mode plot below is like the average of the open loop SD and LD modes. This is related to the linear beam theory and SFD coefficients we used.

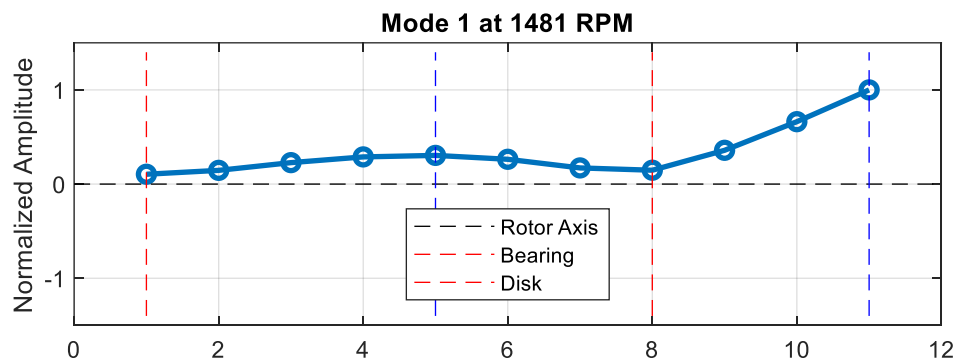


Figure 6.25 Controlled motor first mode shape.

In a similar note the mode plot below is similar to the second mode of the SD and LD configurations. The third mode of the SD is not seen in close loop results.

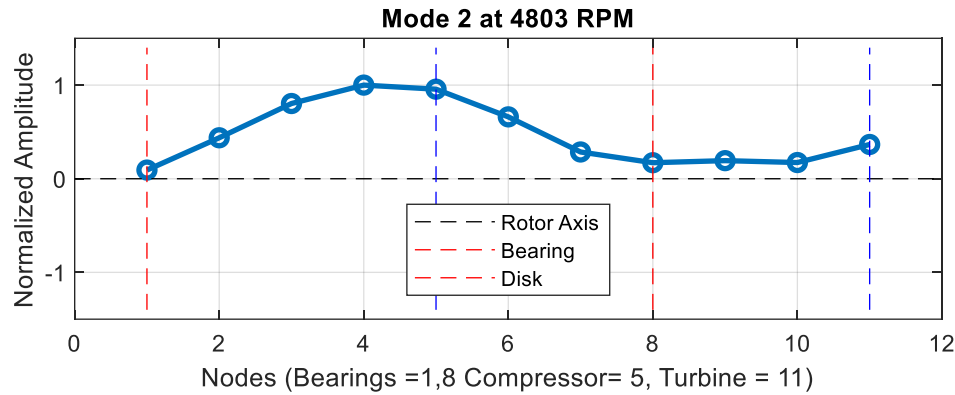


Figure 6.27 Controlled rotor second mode shape.

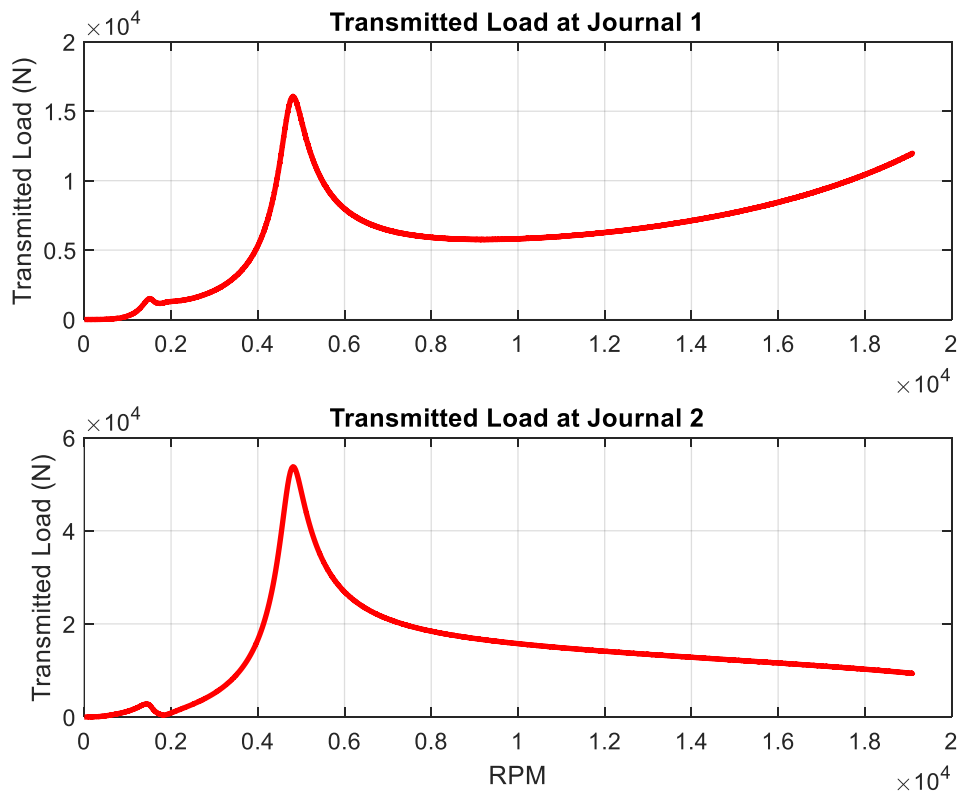


Figure 6.28 Close loop transmitted load at journals.

The peak transmitted force at both bearing nodes shows more than a 40% decrease. This is a significant result, because as previously mentioned the value 60kN gives a simplified factor of safety (radial) of 4.5.

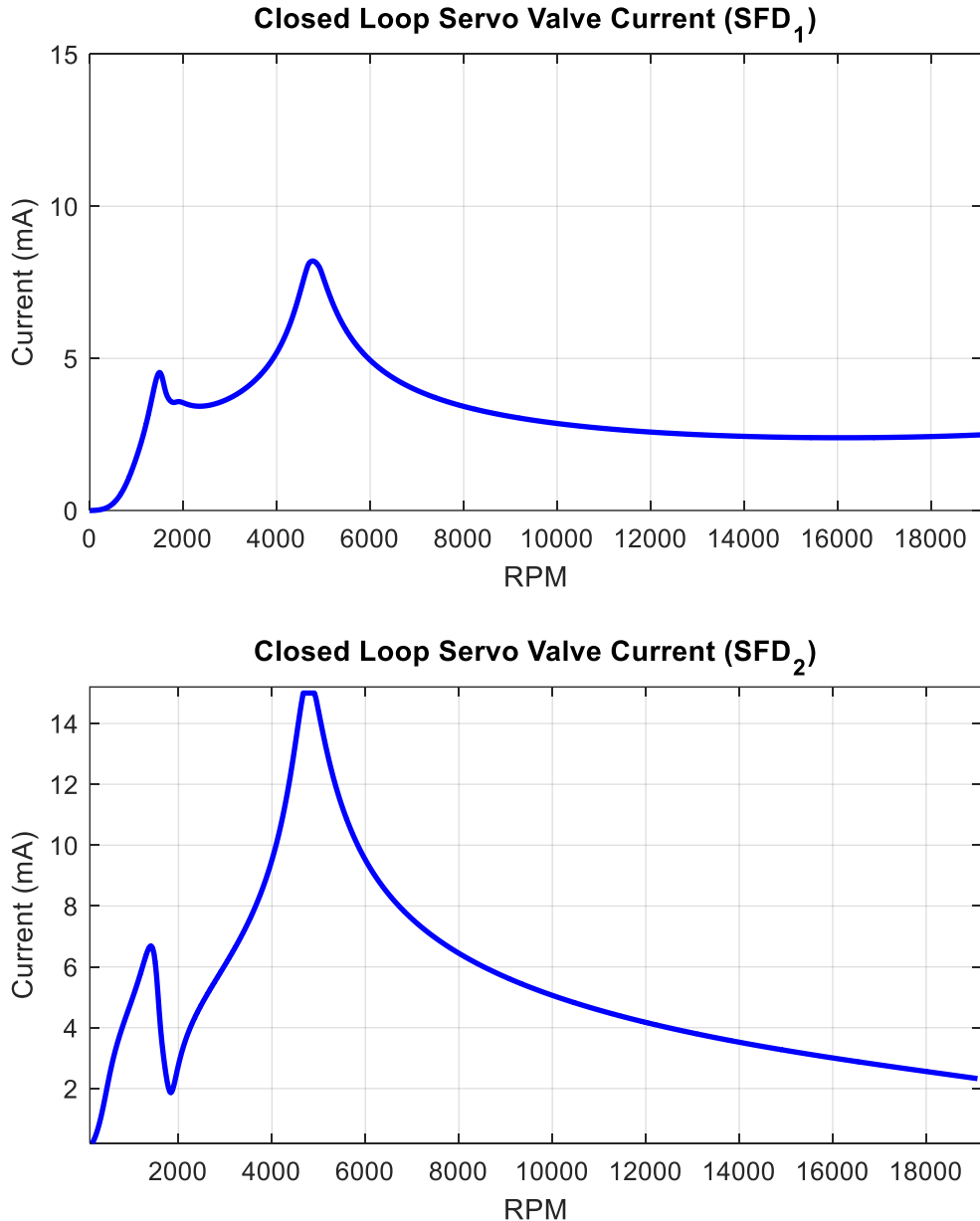


Figure 6.29 Closed loop system controller output current.

The servo valve current for the second servo is saturated at the second critical speed of the rotor. However, the saturation is just momentary and after the critical speed the servo valve current quickly gets smaller.

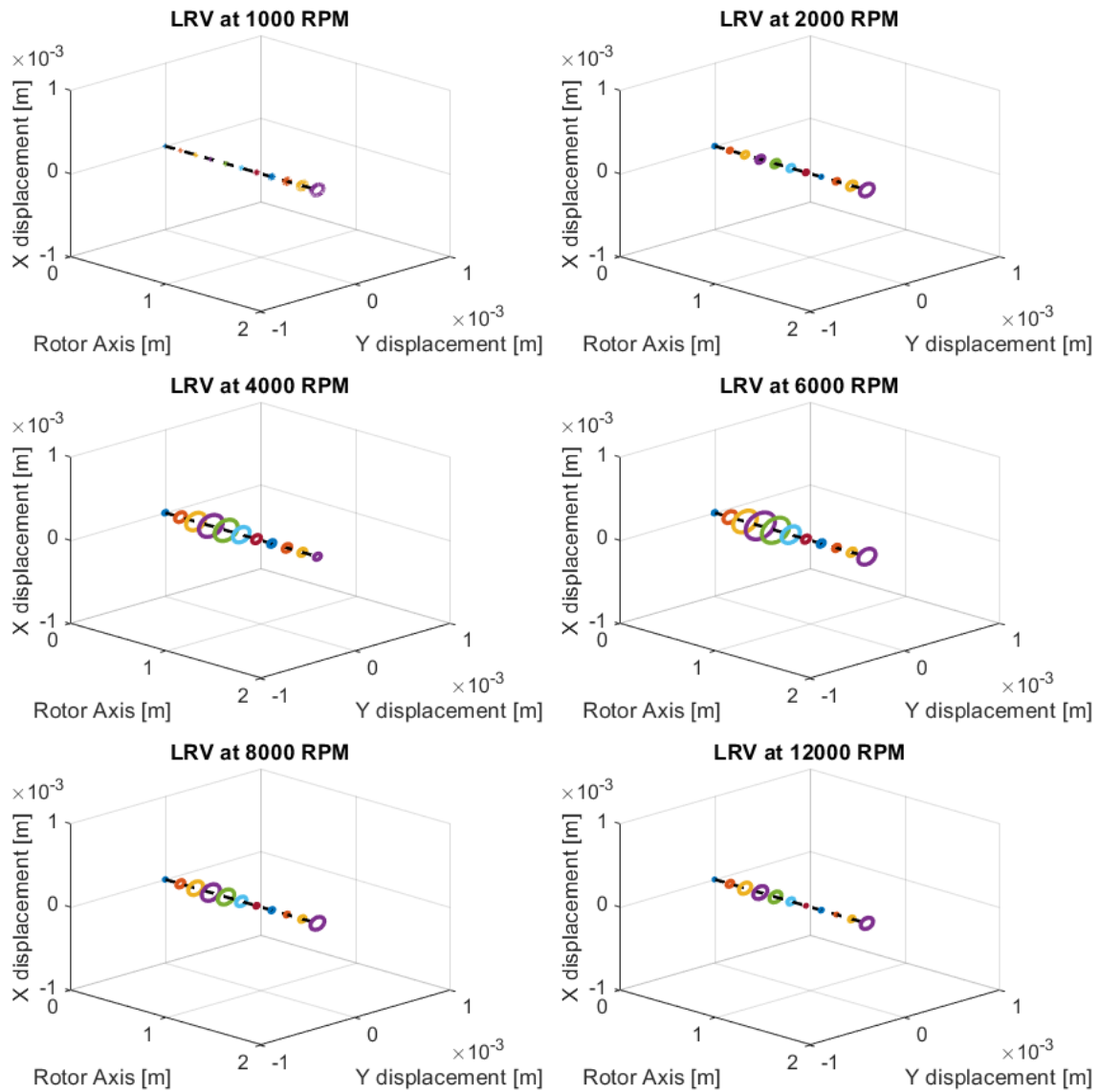


Figure 6.30 LRV plot of the closed loop system.

For disturbance rejection on the FE model, method we applied to the Jeffcott rotor did not produce a stable orbit due to initial transients. To overcome this, we added a sigmoid function (See Appendix B) that provides a smooth transformation from run up to constant velocity imbalance input. This function is shown below.

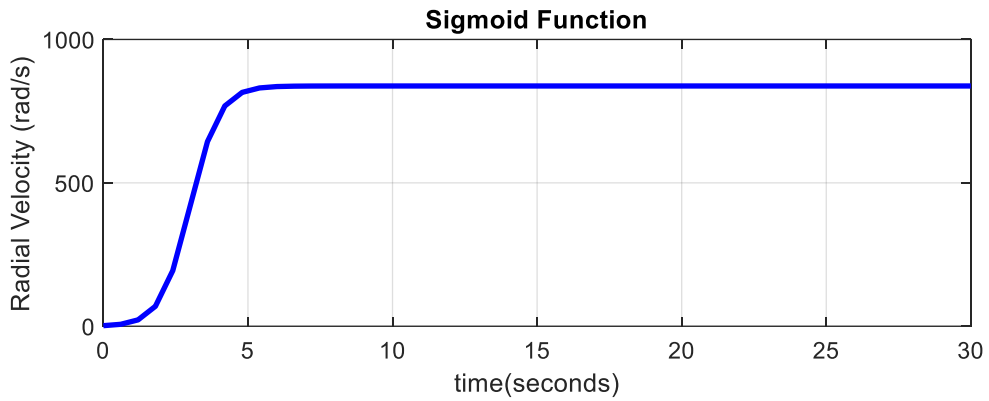


Figure 6.32 Sigmoid function for simulating deceleration and steady state.

As shown below the sigmoid function provides a steady orbit from $t = 5$ to disturbance. However, the magnitude of the disturbance itself also caused instability. For this reason, we lowered the step disturbance to 50% of its original value. In this condition, the controller was able to stabilize the system, but it also gone into saturation (due to the current saturation). But as our aim is to show that the controller can answer disturbance responses and stabilize the otherwise unstable SD orbit, we think this is sufficient.

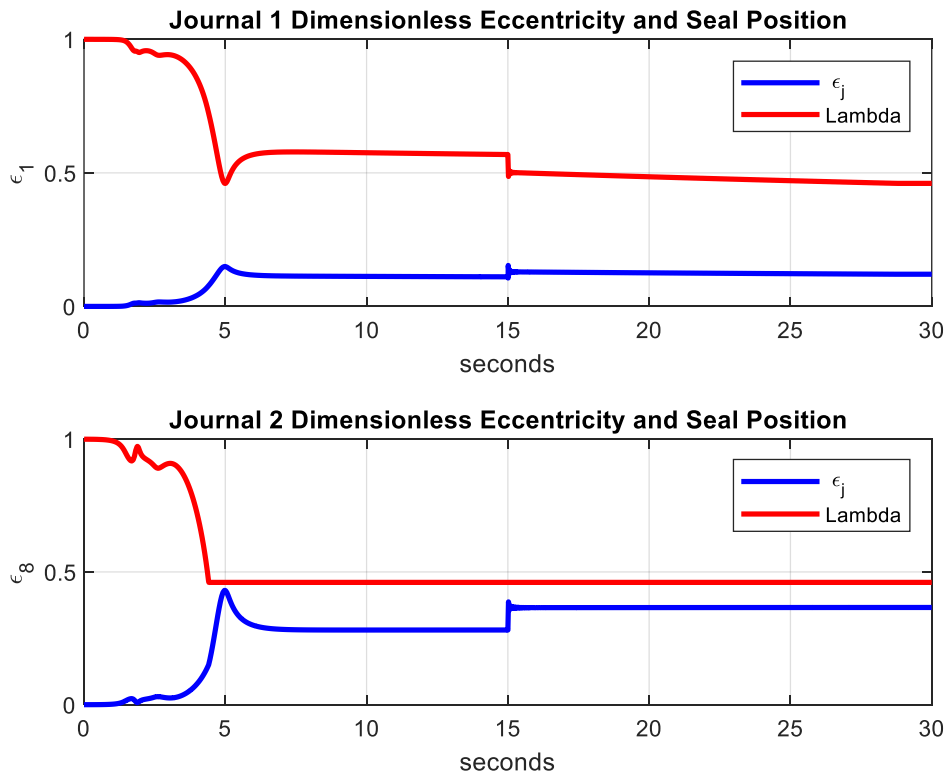


Figure 6.31 Journal position for run up and disturbance

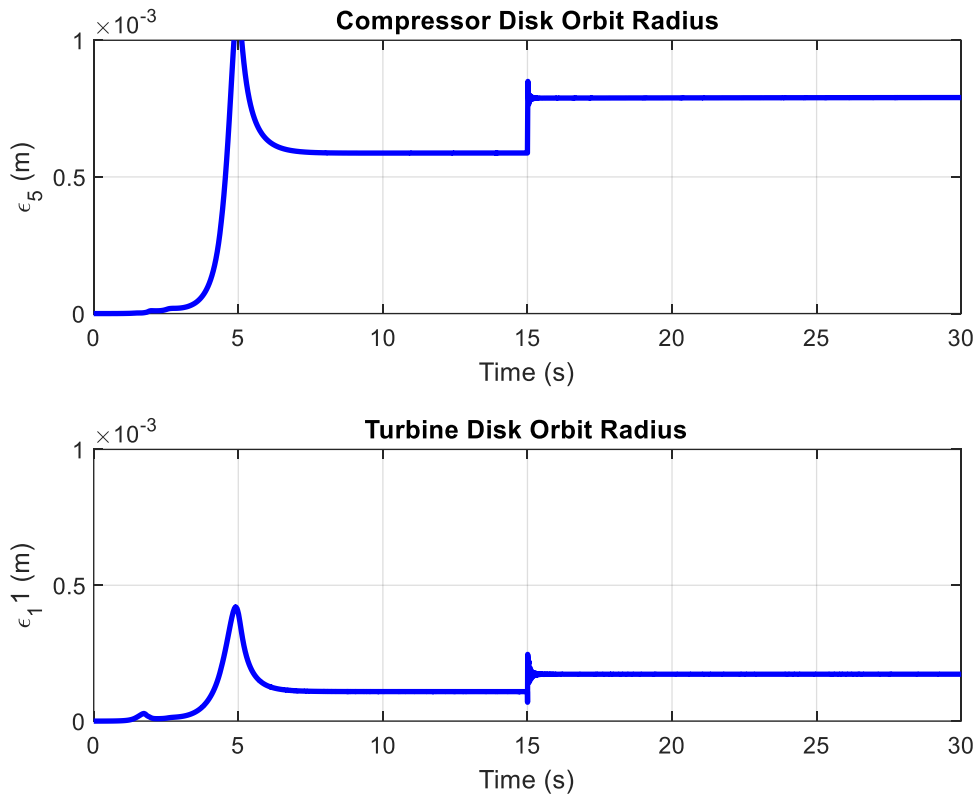


Figure 6.33 Closed loop disk radius for run up and subsequent disturbance.

At the end of the sigmoid function's deceleration, the compressor disk radius passed 1 mm then returned to a stable orbit of 0.6 mm. After the step disturbance transient, the compressor shows a %40 increase in its orbit. For the turbine, the initial stable orbit radius is 0.1 mm, after the disturbance this initial orbit increased by 70%. The disturbance responses for the FE model indicate that saturating the current at 15 mA may lead to unsatisfactory results as with more damping it is possible to lower the steady state response.

Simulations show that the semi active SFD was able to combine positive aspects of the LD and SD configurations by showing better vibration attenuation than the latter, and lower disk attenuation and force than the former.

7) RESULTS AND DISCUSSION

In this work we examined attenuation of jet rotor vibrations by semi-active squeeze film dampers that provide damping to otherwise undamped roller bearings. Furthermore, we applied two common rotor modelling approaches using MATLAB SIMULINK. The first approach considered a symmetric Jeffcott rotor consisting of a hollow shaft, disk, and two SFDs. The open loop simulation using long and short bearing solutions of the SFD gave us valuable insight on the behavior of the decoupled rotor.

The second approach considered the FEM solution by dividing rotor into beam elements. Generalizing a 2-element solution, we developed a 9-building block Simulink model that allowed us to model the P&W 4070 jet engine HP spool as a 10-element shaft with 2 disks and 2 bearings at realistic node locations. The open loop solution of this model showed us how does a model with a more complex structure with coupling (internal) and gyroscopic effects differs from a simplistic (Jeffcott in this case) model.

Using literature, we tried to come up with realistic parameters for various elements of the subsystems we had. For the most part the results show consistent interaction between elements without error. However, starting from the rotor, we sometimes neglected possible sources of flaws and sometimes had to use rough estimation on some crucial aspects of our system due the information understandably not being public. We can list some of the important assumptions we used as follows:

- Lubricant pressure inside the SFD is related to the maximum damping generated by the SFD and for small, centered orbits is constant.
- The SFD the ratio between LD and SD damping and inertia coefficients can be estimated using bearing geometry.
- Due to CCO and semi-LD behavior cross coupling coefficients can be neglected.
- The seal ring position adds a damper finiteness that linearizes the relationship between LD and SD modes.
- The servo valve can be modelled as a 2nd order standard system.
- As SFDs are identical Jeffcott rotor can be used for tuning the controller gains.
- Compared to bearings, shaft internal damping on the shaft is negligible.

Overall, both models showed success during run up simulations, as theorized, the semi active SFD was able to both attenuate vibration at critical speeds and reduce transmitted load away from critical speeds. Furthermore, steady state tests showed PI controllers were able to just enough damping to achieve a steady orbit even with disturbance. However, as we tuned our SD parameters (aside from the lubricant) to give at least one 30% clearance journal eccentricity to attenuate it later by the controller, we think this system could be improved by many additions.

Future improvements to the model, parameters, solver, and overall design can be valuable both to the researchers and to the industry. We think that the next step forward should be focusing on integrating modern approaches like CFD to the semi active system for achieving results that have more weight rather than a simplified bearing geometry. Furthermore, on rotor dynamics part of this work adding a varied shaft geometry with more nodes and disks that represent the multi-stage compressor and turbine blades can yield a more realistic outcome. A third yet also important improvement that could encompass the previous two could be building a matrix based model that is much more efficient compared to the SIMULINK FE model that we have developed for its easy accessibility.

8) REFERENCES

- [1] Thomesen K.K., and H. Andersen, "Experimental Investigation of a Simple Squeeze Film Damper," *Journal of Engineering for Industry*, Hay 1974, pp. 427-430.
- [2] Vance, J. M., & Kirton, A. J. (1975). "Experimental Measurement of the Dynamic Force Response of a Squeeze-Film Bearing Damper.", *ASME Journal of Engineering for Industry*, Nov. 1975
- [3] Gunter, E. J., Barrett, L. E., and Allaire, P. E. (1975), "Design and Application of Squeeze Film Dampers for Turbomachinery Stabilization", *Proceedings of the Fourth Turbomachinery Symposium*, Turbomachinery Laboratory, Texas A&M University, College Station, Texas, pp. 127–141.
- [4] Gunter, E. J., Barrett, L. E., and Allaire, P. E. (1977), "Design of Nonlinear Squeeze-Film Dampers for Aircraft Engines", *Journal of Lubrication Technology*, Vol 99, 1 January 1977.
- [5] San Andrés, L. and Vance, J., 1987, "Experimental Measurement of the Dynamic Pressure Distribution in a Squeeze-Film Bearing Damper Executing Circular Centered Orbits," *ASLE Transactions*, 30, pp. 373-383
- [6] San Andres, L. and Vance, J. M., "Force Coefficients for Open Ended Squeeze Film Dampers Executing Small Amplitude Motions About an Off-Center Equilibrium Position," *ASLE Transactions*, 30 (1), pp. 69-76 (1987).
- [7] El-Shafei, A., 1993, "Experimental and Analytical Investigation of Hybrid Squeeze Film Dampers", *Journal of Engineering for Gas Turbine and Power. Trans. ASME* Vol. 115, No.2, pp. 353-359.
- [8] A. El-Shafei and J. P. Hathout, 1995 "Modeling and control of HSFDs for active control of rotor-bearing systems," *ASME Journal of Engineering for Gas Turbines and Power*, vol. 117, no. 4, pp. 757–766.
- [9] A. El-Shafei, A. T. Massoud, M. El-Hakim, J. P. Hathout, and R. Youssef, 1997., "*Control of Rotor Vibrations Using Hybrid Squeeze Film Dampers*", Final Technical Report, Grant No. F49620-92-J-0512, Cairo University, Cairo, Egypt.
- [10] Diaz, S. E., & San Andrés, L. 2001. A Model for Squeeze Film Dampers Operating with Air Entrainment and Validation with Experiments. *Journal of Tribology*, Vol. 123, pp. 125–133.
- [11] San Andrés, L., Jeung, S.-H, Den, S., and Savela, G., 2016 "Squeeze Film Dampers: A Further Experimental Appraisal of their Dynamic Performance," 45th Turbomachinery Symposium, Texas A&M University, Sept 12-15, Houston, TX, <https://doi.org/10.21423/R1BC7T>
- [12] San Andrés, L., Jeung, S.-H, Den, S., and Savela, G., 2016 "Squeeze Film Dampers: An Experimental Appraisal of their Dynamic Performance," II Asia Turbomachinery and Pump Symposium, Texas A&M University, Feb 22-25, Singapore <https://doi.org/10.21423/R12Q4N>
- [13] Rolls-Royce, *The Jet Engine*, 5th ed. Derby, UK: Rolls-Royce plc, 1996

- [14] W. T. Thomson, 2010, *Theory of Vibrations with Applications*, 4th ed, Taylor & Francis, NY.Ch.3
- [15] Vance, J., Zeidan, F., and Murphy, B, 2010, *Machinery Vibration and Rotordynamics*, John Wiley and Sons, NY
- [16] Maurice R. Adams Jr, 2000, *Rotating Machinery Vibration: From Analysis to Troubleshooting*, Marcel Dekker Inc. NY
- [18] Richard G. Budynas, J. Keith Nisbett , Shigley's Mechanical Engineering Design,9th Edition, McGraw-Hill , New York, USA.
- [19] Edgar J. Gunter, 2002, "The Jeffcott Rotor", Dyrobes Inc.
- [20] Ł. Breńkacz, Ł. Witanowski, M. Drosińska-Komor, and N. Szewczuk-Krypa, "Research and applications of active bearings: A state-of-the-art review," *Mechanical Systems and Signal Processing*, vol. 151, 2021, Art. no. 107423. [Online]. Available: <https://doi.org/10.1016/j.ymssp.2020.107423>
- [21] Zeidan, F. Y., Vance, J. M., and San Andrés, L., 1996 "Design and Application of Squeeze Film Dampers in Rotating Machinery," *Proceedings of the 25th Turbomachinery Symposium*, Texas A&M University, Houston, TX, pp. 169–188
- [22] Zhou, H.; Cao, G.; Chen, X.; Zhang, Y.; Cang, Y., 2023, "A Study on the Thermal Properties of Oil-Film Viscosity in Squeeze Film Dampers". *Lubricants* 2023, 11, 163. doi.org/10.3390/lubricants11040163
- [23] San Andrés, L., 2012, "Squeeze Film Damper: Operation, Models and Technical Issues," *Modern Lubrication Theory, Notes* 13, Texas A&M University Digital Libraries https://rotorlab.tamu.edu/me626/Notes_pdf/Notes13%20Squeeze%20Film%20Dampers.pdf
- [24] Gheller, E.; Chatterton, S.; Vania, A.; Pennacchi, P. "Squeeze Film Damper Modeling: A Comprehensive Approach". *Machines* 2022, 10, 781. <https://doi.org/10.3390/machines10090781>
- [25] DyRoBeS Inc., *DyRoBeS Rotor 1800c Help Manual*, [online manual], Available at: https://dyrobes.com/help1800/Rotor_1800c.pdf
- [26] Airbus S.A.S, *A330 Aircraft Maintenance Manual (AMM)*, Ch.72, Revision 53, Jan. 2011
- [27] Airbus S.A.S., *Aircraft Characteristics – Airport and Maintenance Planning: A330 800-900, Revision 3I*, August 2022. Available at: <https://www.airbus.com/sites/g/files/jlcbta136/files/2022-08/Airbus-Commercial-Aircraft-AC-A330.pdf>
- [28] E. J. Gunter, "The Influence of Bearing Asymmetry on Rotor Stability," Conference Paper, July 2020.

APPENDIX A : ADDITIONAL DIAGRAMS

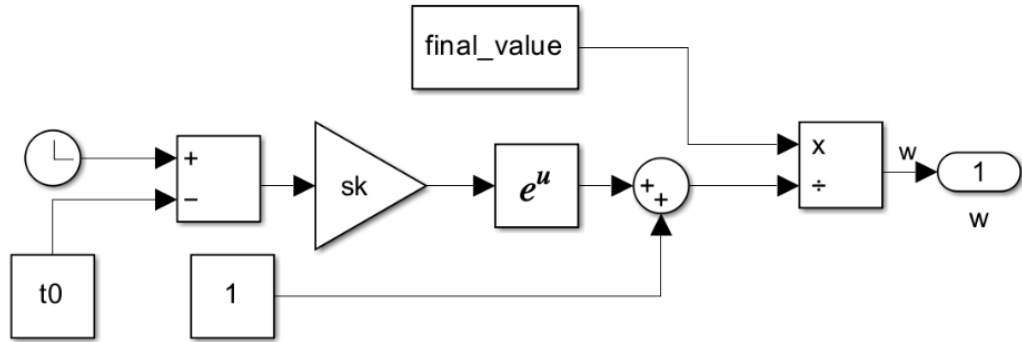


Figure A.1 Sigmoid function block diagram.

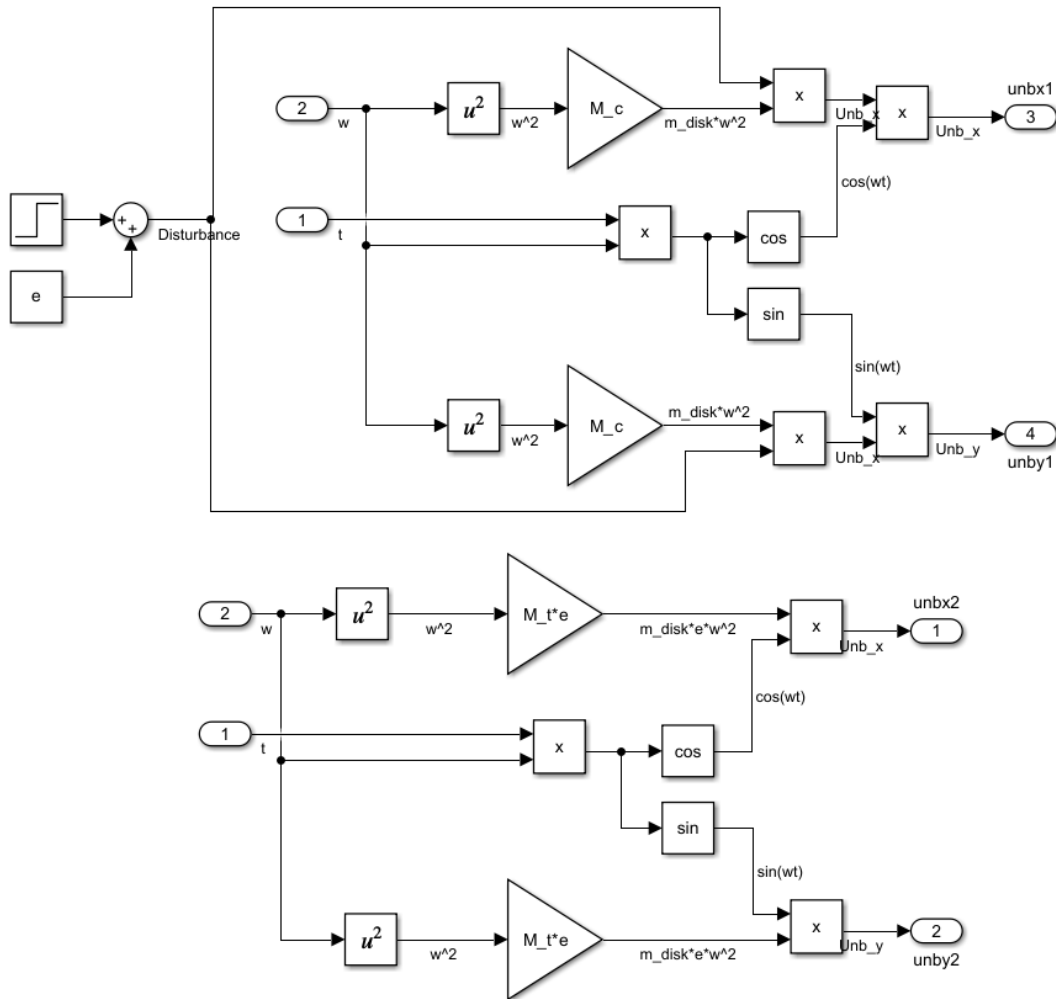


Figure A.2 Unbalance force for FE model.

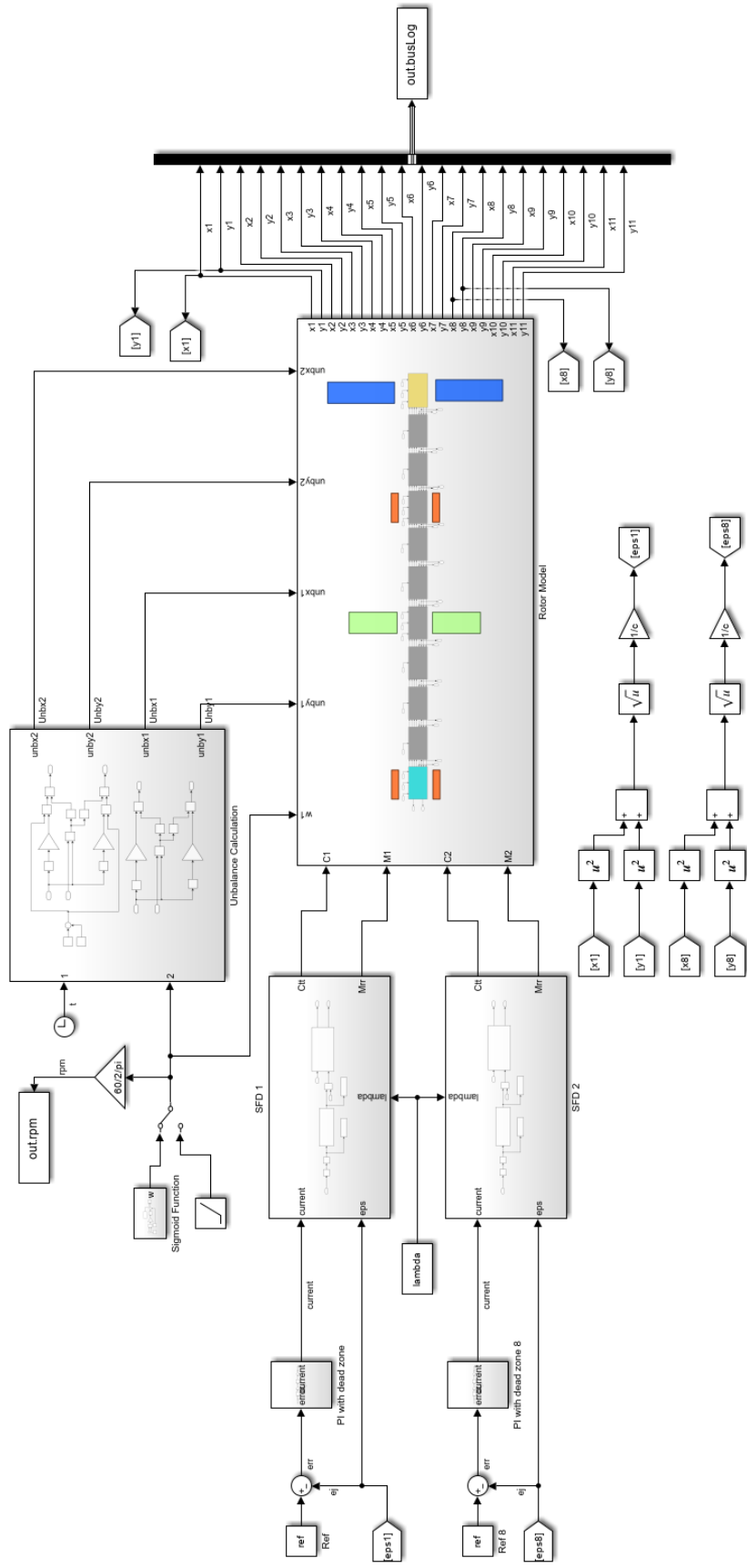


Figure A.3 FE model

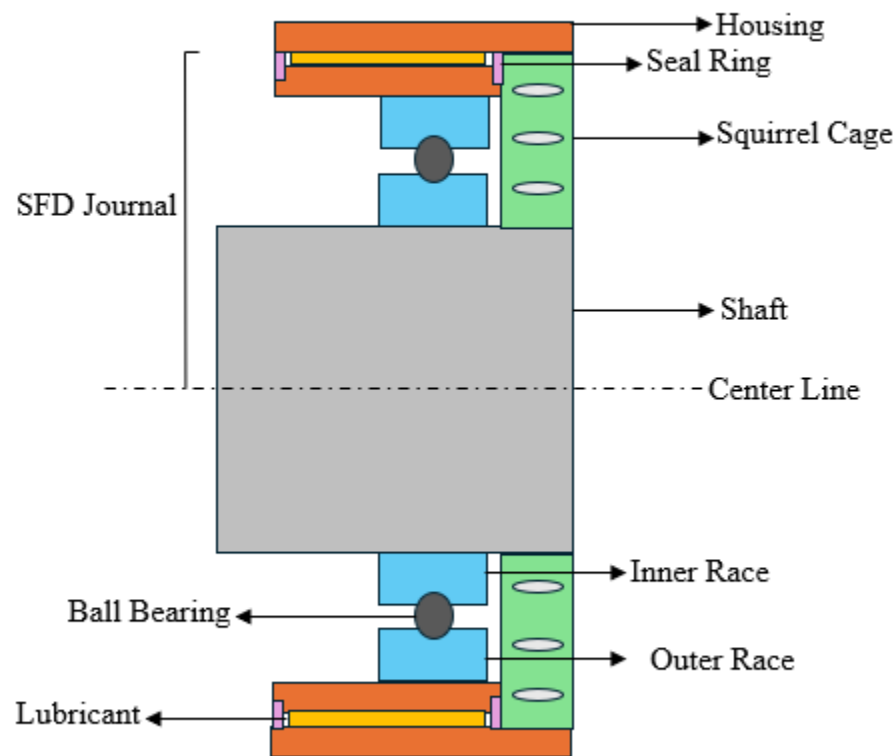


Figure A. 4 Colorized SFD schematic

APPENDIX B : MATLAB CODES

Jeffcott Rotor Parameters:

```

clear
clc
%-----
% Parameters For the Jeffcott_Model.slx file
% Written by: Ayberk Okan Acar & İsmail Hakkı Şentürk
% for ME4098.2 project
%-----
%-----Rotor Geometry and Dimensions-----
% Shaft Properties
L_full = 1.6; % Rotor length from node 1 to node end[m]
n = 3 ; % Number of nodes
L_e = L_full/(n-1); % Element length [m]
D_outer = 0.122; % Outer diameter of hollow shaft [m]
t_wall = 0.014; % Wall thickness [m]
D_inner = D_outer - 2*t_wall; % Inner diameter [m]
rho_steel = 7850; % Density of steel [kg/m^3]
E = 210e9; % Young's modulus [Pa]
% Disk Dimensions simplified as solid disks)
D_disk_c = 0.4; % Estimated diameter of compressor disk [m]
th_disk_c = 0.1; % Estimated compressor disk thickness [m]
D_disk_t = 0.45; % Estimated diameter of turbine disk [m]
th_disk_t = 0.1; % Estimated turbine disk thickness [m]
% Shaft cross-sectional properties
A = pi/4 * (D_outer^2 - D_inner^2); % Hollow cross-sectional area [m^2]
I = pi/64 * (D_outer^4 - D_inner^4); % Area moment of inertia [m^4]
%Compressor disk cross-sectional properties
A_disk_c = pi/4 * (D_disk_c^2-D_outer^2); %Compressor Disk CS [m^2]
%Turbine disk cross-sectional properties
A_disk_t = pi/4 * (D_disk_t^2-D_outer^2); %Turbine Disk CS [m^2]
%Disk Eccentricity
e = 0.25e-3; % Disk eccentricity (m)
% ----- Mass Calculations -----
% Shaft Mass
M = rho_steel*L_full*A; % Beam element disk mass [kg]
% Compressor and Turbine Disks
M_t = rho_steel*th_disk_t*A_disk_t;
M_c = rho_steel*th_disk_c*A_disk_c;
%Lumped Masses
Md = M_t+M_c+ 0.5*M;
Mj = 0.25*M;
Munb = M_t+M_c;
% ----- Stiffness Calculations -----
K = 48*E*I/L_full^3; % Shaft stiffness [N/m]

```

```

% ----- Bearing Parameters -----
% Bearing parameters
D = 0.215; % Bearing diameter (Roller part OD) [m]
L = 0.25*D; % Bearing length [m]
c = .5e-3; % Fluid film clearance [m]
%Lubricant parameters ISO VG 2 at room conditions
mu = 26.5e-3; % Lubricant dynamic viscosity [kg*m/s]
rho = 805; % Lubricant density [kg/m^3]
Kr = K; % Bearing squirrel cage stiffness [N/m]
Aj = pi*D*L; % Journal side area [m^2]
Kg = 3*(D/L)^2; % Bearing damping gain short to long damper
% Damping and inertia using zero amplitude orbit
[C_l, M_l, Cs, Ms] = SFD_eq_coeffs(L, D, c, mu, rho);
% ----- Seal Ring Parameters -----
L_seal = 5e-3; % Seal ring length [m]
D_inner_seal = 0.9*D; % Seal ring inner diameter [m]
As = pi * (D^2-D_inner_seal^2) / 4; % Seal ring surface area [m^2]
m_seal = rho_steel * As* L_seal; % Seal ring mass [kg]
Ks = 50e3; % Seal ring stiffness [N/m]
C_s = .007; % Seal ring damping [Ns/m]
% ----- Servo Valve Parameters -----
zeta_s = 0.7; % Servo valve damping ratio (0.4-0.6)
ws = 250; % Servo ring natural frequency 250 Hz
Ki = .9e5; % Servo ring pressure gain [MPa/mA]
% ----- PI Parameters -----
K_p = 100; % Proportional gain
K_i = 6; % Integral gain

```

Jeffcott Rotor Simulation:

```

% Jeffcott model parameters
run('JefcottParam mlx')
%Select similation rr = 1 if run up else if disturbance
rr = 0;
% Select Open Loop vs Close loop by sim_type == 0
sim_type = 1;
if rr==1
% Run Up
initial_ramp = 0; % rad/s
slope = 100;
disturbance = 0;
disturbance_time = 0; %5;
t_sim = 10;
ref = 0.0;
else
% Disturbance
slope = 0;
initial_ramp = 8.3775*100; % rad/s

```

```

disturbance      = e/2;
disturbance_time = 15;      % 5;
t_sim            = 30;
ref              = 0.0;
end

% Simulation
if sim_type == 0
    lmd = [0, 1];
    out_all = cell(1, length(lmd)); % preallocate a cell array
    for i = 1:length(lmd)
        lambda = lmd(i);           % update lambda
        out = sim('Jeffcott_Model.slx'); % run Simulink
        out_all{i} = out;          % store the entire out struct
    end
else
    out = sim('Jeffcott_Model.slx'); % run Simulink
end

if sim_type == 0
    out_l = out_all{1};
    out_s = out_all{2};
    % === Extraction: lambda = 0 ===
    t_l   = out_l.tout;
    rpm_l = out_l.rpm.Data;

    x1_l = out_l.Bus.x1.Data; y1_l = out_l.Bus.y1.Data;
    x2_l = out_l.Bus.x2.Data; y2_l = out_l.Bus.y2.Data;
    x3_l = out_l.Bus.x3.Data; y3_l = out_l.Bus.y3.Data;

    eps_l1 = sqrt(x1_l.^2 + y1_l.^2);
    eps_l2 = sqrt(x2_l.^2 + y2_l.^2);
    eps_l3 = sqrt(x3_l.^2 + y3_l.^2);

    F_l  = sqrt(out_l.Fx.signal1.Data.^2 + out_l.Fy.signal1.Data.^2) + ...
            sqrt(out_l.Fx.signal2.Data.^2 + out_l.Fy.signal2.Data.^2) + ...
            sqrt(out_l.Fx.signal3.Data.^2 + out_l.Fy.signal3.Data.^2);

    % === Extraction: lambda = 1 ===
    t_s   = out_s.tout;
    rpm_s = out_s.rpm.Data;

    x1_s = out_s.Bus.x1.Data; y1_s = out_s.Bus.y1.Data;
    x2_s = out_s.Bus.x2.Data; y2_s = out_s.Bus.y2.Data;

```

```

x3_s = out_s.Bus.x3.Data; y3_s = out_s.Bus.y3.Data;

eps_s1 = sqrt(x1_s.^2 + y1_s.^2);
eps_s2 = sqrt(x2_s.^2 + y2_s.^2);
eps_s3 = sqrt(x3_s.^2 + y3_s.^2);

F_s = sqrt(out_s.Fx.signal1.Data.^2 +out_s.Fy.signal1.Data.^2)+...
sqrt(out_s.Fx.signal2.Data.^2 +out_s.Fy.signal2.Data.^2)+...
sqrt(out_s.Fx.signal3.Data.^2 +out_s.Fy.signal3.Data.^2);

% === Dimensionless: multiply by 1/c (make sure c is defined!)
E_1 = [eps_11 eps_12 eps_13];
E_s = [eps_s1 eps_s2 eps_s3];
else
    % Extraction
    t = out.tout;
    rpm = out.rpm.Data;
    lambda = out.lambda.Data;
    current = out.current.Data;
    x1 = out.Bus.x1.Data; y1 = out.Bus.y1.Data;
    x2 = out.Bus.x2.Data; y2 = out.Bus.y2.Data;
    x3 = out.Bus.x3.Data; y3 = out.Bus.y3.Data;

    eps1 = sqrt(x1.^2 + y1.^2);
    eps2 = sqrt(x2.^2 + y2.^2);
    eps3 = sqrt(x3.^2 + y3.^2);

    F = sqrt(out.Fx.signal1.Data.^2 +out.Fy.signal1.Data.^2)+...
        sqrt(out.Fx.signal2.Data.^2 +out.Fy.signal2.Data.^2)+...
        sqrt(out.Fx.signal3.Data.^2 +out.Fy.signal3.Data.^2);

    E = [eps1 eps2 eps3];
end

figure(1) % Create new figure window
tiledlayout(2, 1);
if sim_type == 0 ;
    % Titles for each subplot
    labels = {'Journal 1 Dimensionless Eccentricity', ...
              'Journal 2 Dimensionless Eccentricity'};
    K=[1,3]; %nodes
    for i = 1:2
        nexttile;
        if slope == 0

```

```

plot(t_s,E_s(:,K(i))/c,'r',t_l,E_l(:,K(i))/c,'b', 'LineWidth', 2)
xlab = 'seconds';
axx = t_s(end);
axy = 1;
else
plot(rpm_s,E_s(:,K(i))/c,'r',rpm_l,E_l(:,K(i))/c,'b', 'LineWidth',2)
xlab = 'RPM'
axx = rpm_s(end);
axy = 0.5;
end
grid on;
txt = ['\epsilon_{',num2str(K(i))}'];
ylabel(txt);
title(labels{i});
xlabel(xlab);
axis([0 axx 0 axy])
legend('Short','Long')
end
else
if slope == 0
labels = {'Journal 1 Dimensionless Eccentricity'};
plot(t,E(:,1)/c,'r',t,lambda,'b', 'LineWidth', 2)
xlab = 'seconds';
axx = t(end);
axy = 1;
hold on
else
labels = {'Journal 1 Dimensionless Eccentricity'};
plot(t,E(:,1)/c,'r',t,lambda,'b', 'LineWidth', 2)
xlab = 'RPM';
axx = t(end);
axy = 1;
hold on
end
grid on;
txt = ['\epsilon_{j}'];
ylabel(txt);
title(labels{1});
xlabel(xlab);
axis([0 axx 0 axy])
legend('\epsilon_{j}', '\lambda')
hold off
end

figure(2) % Create new figure window
if sim_type == 0
if slope == 0
plot(t_s,eps_s2,'r',t_l,eps_l2,'b','LineWidth', 2)

```

```

xlab = 'seconds'
axx = t_s(end);
axy = 1e-3;
else
plot(rpm_s,eps_s2,'r',rpm_l,eps_l2,'b','LineWidth', 2)
xlab = 'RPM'
axx = rpm_s(end);
axy = 1e-3;
end
grid on;
txt = ['\epsilon_2 (m)'];
ylabel(txt);
title('Disk Orbit Radius');
xlabel(xlab)
axis([0 axx 0 axy])
legend('Short','Long')
else
if slope == 0
plot(t,eps2,'b','LineWidth', 2)
xlab = 'seconds'
axx = t(end);
axy = 1e-3;
else
plot(rpm,eps2,'b','LineWidth', 2)
xlab = 'RPM'
axx = rpm(end);
axy = 1e-3;
end
grid on;
txt = ['\epsilon_2 (m)'];
ylabel(txt);
title('Disk Orbit Radius');
xlabel(xlab)
axis([0 axx 0 axy])
end

if sim_type == 0
if slope ==0
disp('Steady state simulation')
else
% === Choose dataset ===
eps_all = {E_l,E_s};           % or E_long * c
rpmx = {rpm_l,rpm_s};          % or rpm_long
end
else
if slope ==0
disp('Steady state simulation')

```

```

else
% === Choose dataset ===
eps_all = {E};           % or E_long * c
rpmx = {rpm};             % or rpm_long
end
end
for i=1:2-sim_type
% === Smooth signals ===
eps_smooth = smoothdata(eps_all{i}, 1, 'movmean', 50);

% === Compute total RMS response across journals ===
eps_rms = vecnorm(eps_smooth, 2, 2);

% === Find peaks indicating resonances ===
[~, peak_indices] = findpeaks(eps_rms, 'MinPeakProminence', 0.2 * max(eps_rms));
speed = rpmx{i};
peak_rpms = speed(peak_indices);

% === Extract normalized mode shapes at resonances ===
mode_shapes = eps_smooth(peak_indices, :) ./ max(abs(eps_smooth(peak_indices, :)), [], 2);

% === Plot mode shapes ===
figure(2+i);

tiledlayout(size(mode_shapes, 1), 1);
x_nodes = 1:size(eps_all{i}, 2);

for k = 1:size(mode_shapes, 1)
nexttile;
plot(x_nodes, mode_shapes(k, :), '-o', 'LineWidth', 2);
ylim([-1.1, 1.1]);
ylabel('Normalized Amplitude');
if i == 1
title(sprintf('LD Mode %d Shape at %.0f RPM', k, peak_rpms(k)));
else
title(sprintf('SD Mode %d Shape at %.0f RPM', k, peak_rpms(k)));
end
grid on;
end

xlabel('Nodes (1 = journal 1, 2 = disk, 3 = journal 2)');

```

```

end

figure(4) % Create new figure window
if sim_type == 0
    if slope == 0
        plot(t_s,F_s,'r',t_l,F_l,'b','LineWidth',2)
        xlabel = 'seconds'
    else
        plot(rpm_s,F_s,'r',rpm_l,F_l,'b','LineWidth',2)
        xlabel = 'RPM'
    end
    grid on
    xlabel(xlab)
    ylabel('Transmitted Load (N)')
    legend('Short','Long')
    title('Transmitted Load For SD and LD Modes')
else
    if slope == 0
        plot(t,F,'b','LineWidth',2)
        xlabel = 'seconds'
    else
        plot(rpm,F,'b','LineWidth',2)
        xlabel = 'RPM'
    end
    grid on
    xlabel(xlab)
    ylabel('Transmitted Load (N)')
    title('Transmitted Load For The Closed Loop System')
end

% Current vs Rpm
figure()
plot(t,current,'b','LineWidth',2)
title('Closed Loop Servo Valve Current')
xlabel('RPM')
ylabel('Current (mA)')
grid on

```

Jeffcott Rotor PI Tuning:

```

% Jeffcott model parameters
run('JefcottParam mlx')

%Select simulation rr = 1 if run up else if disturbance

```

```

rr = 1;
if rr==1
% Run Up
initial_ramp      = 0; % rad/s
slope            = 100;
disturbance       = 0;
disturbance_time = 0;    %5;
t_sim            = 10;
ref              = 0.0;
else
initial_ramp      = 837.75; % rad/s
slope            = 0;
disturbance       = e;
disturbance_time = 2;    %5;
t_sim            = 4;
ref              = 0.0;
end
% Define proportional and integral gain ranges
Kp_values = [50 100 150];
Ki_values = [0  6 12];

[Kp_grid, Ki_grid] = ndgrid(Kp_values, Ki_values);
numCombos = numel(Kp_grid);
t_all = cell(1, numCombos);
rpm_all = cell(1, numCombos);
epsilon_all = cell(1, numCombos);
lambda_all = cell(1, numCombos);
legend_labels = cell(1, numCombos);
current_all= cell(1, numCombos);

for idx = 1:numCombos
model = Simulink.SimulationInput("Jeffcott_Model");
model = model.setVariable('K_p', Kp_grid(idx));
model = model.setVariable('K_i', Ki_grid(idx));
out = sim(model);

t_all{idx} = out.tout;
rpm_all{idx} = out.rpm.Data;
epsilon_all{idx} = sqrt(out.Bus.x1.Data.^2 + out.Bus.y1.Data.^2) * 1/c;
lambda_all{idx} = out.lambda.Data;
current_all{idx} = out.current.Data;

legend_labels{idx} = sprintf('Kp=% .3f, Ki=% .3f', Kp_grid(idx),
Ki_grid(idx));
end

```

```

figure(1)
num_Kp = length(Kp_values);
num_Ki = length(Ki_values);

rows = num_Ki;
cols = num_Kp;
count = 1;
for i_row = 1:rows
    for i_col = 1:cols
        subplot(rows, cols, (i_row-1)*cols + i_col);
        if slope == 0
            eps_all = epsilon_all{count};
            hold on;
            plot(t_all{count}, eps_all(:,1), 'b-', 'LineWidth', 1.2);
            plot(t_all{count}, lambda_all{count}, 'r-', 'LineWidth', 1.8);
            xlabel = 'seconds';
        else

            eps_all = epsilon_all{count};
            hold on;
            plot(rpm_all{count}, eps_all(:,1), 'b-', 'LineWidth', 1.2);
            plot(rpm_all{count}, lambda_all{count}, 'r-', 'LineWidth', 1.8);
            xlabel = 'RPM';
        end
        xlabel(xlab);
        ylabel('Value');
        ylim([0 1]);
        title(legend_labels{count});
        grid on;
        hold off
        count = count + 1;
    end
end

```

```

figure(2)
num_Kp = length(Kp_values);
num_Ki = length(Ki_values);

```

```

rows = num_Ki;
cols = num_Kp;
count = 1;
for i_row = 1:rows

```

```

for i_col = 1:cols
    subplot(rows, cols, (i_row-1)*cols + i_col);
    if slope == 0
        curr_all = current_all{count};
        hold on;
        plot(t_all{count}, curr_all(:,1), 'b-', 'LineWidth', 1.2);
        xlabel = 'seconds';
    else

        curr_all = current_all{count};
        hold on;
        plot(rpm_all{count}, curr_all(:,1), 'b-', 'LineWidth', 1.2);
        xlabel = 'RPM';
    end
    xlabel(xlab);
    ylabel('Current (mA)');
    title(legend_labels{count});
    grid on;
    hold off
    count = count + 1;
end
end

```

FE Model Parameters:

```

clear
clc
%-----
% Parameters For the FEM_Model.slx file
% Written by: Ayberk Okan Acar & İsmail Hakkı Şentürk
% for ME4098.2 project
%-----
% The parameters aim to satisfy Euler beam
% element stiffness, gyroscopic coefficients, and
% lumped mass formulations.
% The starting, internal, and ending nodes for naked,
% SFD, and Disk configurations are checked here.

%-----Rotor Geometry and Dimensions-----
% Shaft Properties
L_full = 1.6; % Rotor length from node 1 to node end[m]
n = 11; % Number of nodes
L_e = L_full/(n-1); % Element length [m]

```

```

D_outer = 0.122; % Outer diameter of hollow shaft [m]
t_wall = 0.014; % Wall thickness [m]
D_inner = D_outer - 2*t_wall; % Inner diameter [m]

rho_steel = 7850; % Density of steel [kg/m^3]
E = 210e9; % Young's modulus [Pa]

% Disk Dimensions simplified as solid disks)
D_disk_c = 0.4; % Estimated diameter of compressor disk [m]
th_disk_c = 0.1; % Estimated compressor disk thickness [m]
D_disk_t = 0.45; % Estimated diameter of turbine disk [m]
th_disk_t = 0.1; % Estimated turbine disk thickness [m]

% Shaft cross-sectional properties
A = pi/4 * (D_outer^2 - D_inner^2); % Hollow cross-sectional area [m^2]
I = pi/64 * (D_outer^4 - D_inner^4); % Area moment of inertia [m^4]

%Compressor disk cross-sectional properties
A_disk_c = pi/4 * (D_disk_c^2-D_outer^2); %Compressor Disk CS [m^2]

%Turbine disk cross-sectional properties
A_disk_t = pi/4 * (D_disk_t^2-D_outer^2); %Turbine Disk CS [m^2]

%Disk Eccentricity
e = 0.25e-3; % Disk eccentricity (m)

% ----- Mass Calculations -----
% Beam Element
M = rho_steel*L_e*A; % Beam element disk mass [kg]
Mf = M/2; % First node disk mass [kg]
Mi = M; % Internal node disk mass [kg]
Ml = M/2; % Last node disk mass [kg]

% Compressor and Turbine Disks
M_t = rho_steel*th_disk_t*A_disk_t;
M_c = rho_steel*th_disk_c*A_disk_c;

%Lumped Masses

```

```

Mt = M_t + Mf;          % Final node turbine lumped mass [kg]
Mc = M_c + Mi;          % Internal node compressor lumped mass [kg]

% ----- Inertia Calculations -----
% Tilt moment of inertia Jt = 0.25*m*(Rout^2 + Rin^2).
% Polar moment of inertia Jp = 0.5*m*(Rout^2 + Rin^2).
%Beam element
It = 1/96 * M * (3*(D_outer^2 + D_inner^2) + (L_e^2))+ M*L_e^2/32; % Element
[kg*m^2]
Ip = 1/16 * M * (D_inner^2 + D_outer^2);                                % Element
[kg*m^2]

%Disk
It_t = 0.25 * Mt * (D_disk_t^2+D_outer^2)/4;      % Turbine [kg*m^2]
Ip_t = 0.5 * Mt * (D_disk_t^2+D_outer^2)/4;      % Turbine [kg*m^2]
It_c = 0.25 * Mc * (D_disk_c^2+D_outer^2)/4;      % Compressor [kg*m^2]
Ip_c = 0.5 * Mc * (D_disk_c^2+D_outer^2)/4;       % Compressor [kg*m^2]

%Lumped Inertia
Itt=It_t+2*It;    % Final node turbine lumped inertia [kg]
Ipt=Ip_t+2*Ip;    % Final node turbine lumped inertia [kg]
Itc=It_c+2*It;    % Internal node compressor lumped inertia [kg]
Ipc=Ip_c+2*Ip;    % Internal node compressor lumped inertia [kg]

% ----- Stiffness Calculations -----
K_star = 2*E*I/L_e^3; % Stiffness coefficient that is factored
K1 = 6*K_star;        % K1 = 12 EI /L^3
K2 = 3*K_star*L_e;    % K2 = 6EI/L^2
K3 = K_star*L_e^2;    % K3 = 3EI/L

% ----- Bearing Parameters -----
% Bearing parameters
D = 0.215;           % Bearing diameter (Roller part OD) [m]
L = 0.25*D;          % Bearing length [m]
c = .4e-3;            % Fluid film clearance [m]

%Lubricant parameters ISO VG 2 at room conditions
mu = 26.5e-3;         % Lubricant dynamic viscosity [kg*m/s]
rho = 805;             % Lubricant density [kg/m^3]
Kr = 1.7330e+07;      % Bearing squirrel cage stiffness [N/m]
Aj = pi*D*L;          % Journal side area [m^2]
Kg = 3*(D/L)^2;        % Bearing damping gain short to long damper

```

```

% Damping and inertia using zero amplitude orbit
[C_1, M_1, Cs, Ms] = SFD_eq_coeffs(L, D, c, mu, rho);

% ----- Seal Ring Parameters -----
L_seal      = 5e-3;                                % Seal ring length [m]
D_inner_seal = 0.9*D;                            % Seal ring inner diameter [m]
As          = pi * (D^2-D_inner_seal^2) / 4;        % Seal ring surface area [m^2]
m_seal       = rho_steel * As* L_seal;            % Seal ring mass [kg]
Ks          = 50e3;                                % Seal ring stiffness [N/m]
Cs          = .007;                                % Seal ring damping [Ns/m]

% ----- Servo Valve Parameters -----
zeta_s = 0.7;           % Servo valve damping ratio (0.4-0.6)
ws     = 250;             % Servo ring natural frequency 250 Hz
Ki     = .9e5;            % Servo ring pressure gain [MPa/mA]

% ----- PI Parameters -----
K_p = 100;           % Proportional gain
K_i = 6;              % Integral gain

```

```

% === Bearing Locations ===
plot([0,0],[-0.5,0.5], 'r--')
hold on
plot([7*0.16,7*0.16],[-0.5,0.5], 'r--')
plot([4*0.16,4*0.16],[-0.5,0.5], 'b--')
plot([10*0.16,10*0.16],[-0.5,0.5], 'b--')

% === Node positions (11 nodes for 10 elements) ===
node_x = linspace(0, L_full, n);

% === Draw disks at nodes 5 and 11 ===
% Disk at node 5
rectangle('Position', [node_x(5) - th_disk_c/2, -D_disk_c/2, th_disk_c,
D_disk_c], ...
    'FaceColor', [0 0 1], 'EdgeColor', 'k');
% Disk at node 11
rectangle('Position', [node_x(11) - th_disk_c/2, -D_disk_t/2, th_disk_c,
D_disk_t], ...
    'FaceColor', [0 0 1], 'EdgeColor', 'k');
% === Draw shaft ===
% === Draw outer shaft as a long rectangle ===
rectangle('Position', [0, -D_outer/2, L_full, D_outer], ...

```

```

        'FaceColor', [0.8 0.8 0.8], 'EdgeColor', 'k');

% === Draw inner shaft to show hollow section ===
rectangle('Position', [0, -D_inner/2, L_full+th_disk_c/2, D_inner], ...
        'FaceColor', [1 1 1], 'EdgeColor', 'k');

% === Mark nodes and labels ===
for i = 1:length(node_x)
    plot(node_x(i), 0, 'ko', 'MarkerFaceColor', 'k');      % draw node
    text(node_x(i), 0.06, sprintf('%d', i), 'HorizontalAlignment', 'center');
end

% === Adjust plot limits ===
xlim([-0.1 L_full+0.1]);
ylim([-0.5 0.5]);
legend('Bearing Locations', '', 'Disk Locations')
hold off;

```

FE Model Simulation:

```

% ===== Simulation and Initialization =====
% Run Parameter File (.mlx or .m)
run('FemParam mlx');

%Select simulation rr = 1 if run up else if disturbance
rr = 0;
%Select simulation type 0 if open loop 1 if close loop
sim_type = 1;
if rr == 1
% Run Up
    initial_ramp      = 0;      % rad/s
    slope             = 100;
    disturbance       = 0;
    disturbance_time = 0;      %5;
    t_sim             = 20;
    ref               = 0.0;
else
% Disturbance
    slope = 0;
    final_value      = 994; % rad/s
    t0              = 3;      % midpoint
    s_k             = -2;    % sigmoid k
    disturbance_time = 8;    % 5;
    disturbance     = e*0.5;
    t_sim           = 10;

```

```

    ref          = 0.0;
end
% Run Simulation
if sim_type == 0
    lambda = 1
    out_S = sim('FEM_Model.slx'); % run Simulink
    lambda = 0;
    out_L = sim('FEM_Model.slx'); % run Simulink
else
    out = sim('FEM_Model.slx');
end

% ===== Data Setup =====
% Extracts open loop LD and SD mode data or CL
if sim_type == 0
    % Open Loop
    % Position bus
    bus_l = out_L.busLog.signals.values;
    bus_s = out_S.busLog.signals.values;

    % Time & RPM
    t_l   = out_L.tout; t_s   = out_S.tout;
    rpm_l = out_L.rpm.Data; rpm_s = out_S.rpm.Data;

    % Set Position X Y in matrix form
    Xi  =1:2:22; Yi  =2:2:22;
    X_l=zeros(length(bus_l),11); Y_l=zeros(length(bus_l),11);
    X_s=zeros(length(bus_s),11); Y_s=zeros(length(bus_s),11);

    for i=1:11
        X_l(:,i)=bus_l(:,Xi(i));
        X_s(:,i)=bus_s(:,Xi(i));
        Y_l(:,i)=bus_l(:,Yi(i));
        Y_s(:,i)=bus_s(:,Yi(i));
    end

    % Extract all X and Y nodes
    for i = 1:11
        eval(sprintf('x%d_l = X_l(:,%d);', i, i));eval(sprintf('y%d_s = Y_s(:,%d);',
i, i));
        eval(sprintf('y%d_l = Y_l(:,%d);', i, i));eval(sprintf('x%d_s = X_s(:,%d);',
i, i));
    end

```

```

% Calculate orbit radius
E_l = zeros(length(x1_l), 11); E_s = zeros(length(x1_s), 11);

% Eval loop for size
for i = 1:11
    % Compute LD
    eval(sprintf('E_l(:,%d) = sqrt(x%d_l.^2 + y%d_l.^2);', i, i, i));
    % Compute SD
    eval(sprintf('E_s(:,%d) = sqrt(x%d_s.^2 + y%d_s.^2);', i, i, i));
end
% Forces
F1_l = sqrt(out_L.F8y.signal1.Data.^2+out_L.F8x.signal1.Data.^2) + ...
        sqrt(out_L.F1y.signal2.Data.^2+out_L.F1x.signal2.Data.^2) + ...
        sqrt(out_L.F1y.signal3.Data.^2+out_L.F1x.signal3.Data.^2);
F8_l = sqrt(out_L.F8y.signal1.Data.^2+out_L.F8x.signal1.Data.^2) + ...
        sqrt(out_L.F8y.signal2.Data.^2+out_L.F8x.signal2.Data.^2) + ...
        sqrt(out_L.F8y.signal3.Data.^2+out_L.F8x.signal3.Data.^2);
% Forces for Short Simulation
F1_s = sqrt(out_S.F1y.signal1.Data.^2 + out_S.F1x.signal1.Data.^2) + ...
        sqrt(out_S.F1y.signal2.Data.^2 + out_S.F1x.signal2.Data.^2) + ...
        sqrt(out_S.F1y.signal3.Data.^2 + out_S.F1x.signal3.Data.^2);

F8_s = sqrt(out_S.F8y.signal1.Data.^2 + out_S.F8x.signal1.Data.^2) + ...
        sqrt(out_S.F8y.signal2.Data.^2 + out_S.F8x.signal2.Data.^2) + ...
        sqrt(out_S.F8y.signal3.Data.^2 + out_S.F8x.signal3.Data.^2);
else
    %Close Loop

    % Position bus
    bus = out.busLog.signals.values;
    % Time RPM Lambda and current
    t = out.tout; rpm = out.rpm.Data;
    lambda1 = out.lambda1.Data;
    lambda8 = out.lambda8.Data;
    lambda = [lambda1 lambda8];
    current1 = out.current1.Data;
    current8 = out.current8.Data;
    current = [current1 current8]
    % Set Position X Y in matrix form
    Xi = 1:2:22; Yi = 2:2:22;
    X=zeros(length(bus),11); Y=zeros(length(bus),11);

```

```

for i=1:11
    X(:,i)=bus(:,Xi(i)); Y(:,i)=bus(:,Yi(i));
end

% === Extract all X and Y nodes ===
for i = 1:11
    eval(sprintf('x%d = X(:,%d);', i, i));
    eval(sprintf('y%d = Y(:,%d);', i, i));
end

% Calculate orbit radius
E = zeros(length(x1), 11);
% Eval loop for size
for i = 1:11
    % Compute LD
    eval(sprintf('E(:,%d) = sqrt(x%d.^2 + y%d.^2);', i, i, i));
end

% Force
F1 = sqrt(out.F1y.signal1.Data.^2 + out.F1x.signal1.Data.^2) + ...
sqrt(out.F1y.signal2.Data.^2 + out.F1x.signal2.Data.^2) + ...
sqrt(out.F1y.signal3.Data.^2 + out.F1x.signal3.Data.^2);

F8 = sqrt(out.F8y.signal1.Data.^2 + out.F8x.signal1.Data.^2) + ...
sqrt(out.F8y.signal2.Data.^2 + out.F8x.signal2.Data.^2) + ...
sqrt(out.F8y.signal3.Data.^2 + out.F8x.signal3.Data.^2);
end

```

```

% ===== Journal Orbits =====
% Plots both run up or disturbance based on slope
figure(2)
tiledlayout(2, 1);
K=[1,8]; % Journal nodes

if sim_type == 0
    % Titles for each subplot
    labels = {'Journal 1 Dimensionless Eccentricity', ...
        'Journal 2 Dimensionless Eccentricity'};
for i = 1:2
    nexttile;
    if slope == 0
        plot(t_s,E_s(:,K(i))/c, 'r', t_l,E_l(:,K(i))/c, 'b', 'LineWidth', 2)
        xlabel = 'seconds';
    end
end

```

```

    axx = t_s(end);
    axy = 1;
else
    plot(rpm_s,E_s(:,K(i))/c,'r',rpm_l,E_l(:,K(i))/c,'b', 'LineWidth',2)
    xlabel = 'RPM'
    axx = rpm_s(end);
    axy = 0.5;
end
grid on;
txt = ['\epsilon',num2str(K(i))];
ylabel(txt);
title(labels{i});
xlabel(xlab);
axis([0 axx 0 axy])
legend('Short','Long')
end
else
    % Titles for each subplot
    labels = {'Journal 1 Dimensionless Eccentricity and Seal Position', ...
        'Journal 2 Dimensionless Eccentricity and Seal Position'};
for i = 1:2
    nexttile;
    if slope == 0
        plot(t,E(:,K(i))/c,'b',t,lambda(:,i),'r', 'LineWidth', 2)
        xlabel = 'seconds';
        axx = t(end);
        axy = 1;
    else
        plot(rpm,E(:,K(i))/c,'b',rpm,lambda(:,i),'r', 'LineWidth',2)
        xlabel = 'RPM';
        axx = rpm(end);
        axy = 1;
    end
    grid on;
    txt = ['\epsilon',num2str(K(i))];
    ylabel(txt);
    title(labels{i});
    xlabel(xlab);
    axis([0 axx 0 axy])
    legend(' \epsilon_{j}', 'Lambda')
end
end

```

```

% ===== Disk Orbits =====
% Plots both run up or disturbance based on slope
figure(3)

```

```

tiledlayout(2, 1);

% Nodes of interest
K = [5, 11]; % Compressor and Turbine Nodes

% Titles for each subplot
labels = {'Compressor Disk Orbit Radius', ...
    'Turbine Disk Orbit Radius'};
if sim_type == 0
    for i = 1:2
        nexttile;
        if slope == 0
            plot(t_s, E_s(:,K(i)), 'r', t_l, E_l(:,K(i)), 'b', 'LineWidth', 2);
            xlabel = 'Time (s)';
            axx = t_s(end);
        else
            plot(rpm_s, E_s(:,K(i)), 'r', rpm_l, E_l(:,K(i)), 'b', 'LineWidth', 2);
            xlabel = 'RPM';
            axx = rpm_s(end);
        end
        grid on;
        txt = ['\epsilon', num2str(K(i)), ' (m)'];
        ylabel(txt);
        title(labels{i});
        xlabel(xlab);
        axis([0 axx 0 1e-3]);
        legend('Short', 'Long');
    end
else
    for i = 1:2
        nexttile;
        if slope == 0
            plot(t, E(:,K(i)), 'b', 'LineWidth', 2);
            xlabel = 'Time (s)';
            axx = t(end);
        else
            plot(rpm, E(:,K(i)), 'b', 'LineWidth', 2);
            xlabel = 'RPM';
            axx = rpm(end);
        end
        grid on;
        txt = ['\epsilon', num2str(K(i)), ' (m)'];
        ylabel(txt);
        title(labels{i});
        xlabel(xlab);
        axis([0 axx 0 1e-3]);
    end
end

```

```

end
end

% ===== Mode Shapes =====
if sim_type == 0;
    eps_all = {E_l,E_s}; % Node positions
    rpm = {rpm_l,rpm_s}; % Rpm
else
    eps_all = {E}; % Node positions
    rpmx = {rpm}; % Rpm
    % Works on run up (slope == 100)
end
if slope ==0
    disp('Steady state simulation')
else
    for i=1:2-sim_type
        % Smooth peaks
        eps_smooth = smoothdata(eps_all{i}, 1, 'movmean', 50);

        % Compute RMS
        eps_rms = vecnorm(eps_smooth, 2, 2);

        % Find Peak Orbit for a RPM window and assign a threshold
        [~, peak_indices] = findpeaks(eps_rms, 'MinPeakProminence', 0.1 *
max(eps_rms));
        speed = rpmx{i};
        peak_rpms = speed(peak_indices);

        % Extract mode shapes and normalize
        mode_shapes = eps_smooth(peak_indices, :) ./ max(abs(eps_smooth(peak_indices,
:))), [], 2);

        % Plot mode shapes
        figure(3+i);
        tiledlayout(size(mode_shapes, 1), 1);
        x_nodes = 1:size(eps_all{i}, 2);
        for k = 1:size(mode_shapes, 1)
            nexttile;
            plot(x_nodes, mode_shapes(k, :), '-o', 'LineWidth', 2);
            ylim([-1.5, 1.5]);
            ylabel('Normalized Amplitude');
            title(sprintf('Mode %d at %.0f RPM', k, peak_rpms(k)));
            hold on
    end
end

```

```

%Plot important nodes as dashed vertical and rotor axis
plot([0 12],[0 0], 'k--'); % Rotor axis
plot([1 1],[-1.4 1.4], 'r--'); % SFD 1
plot([8 8],[-1.4 1.4], 'r--'); % SFD 2
plot([5 5],[-1.4 1.4], 'b--'); % SFD 1
plot([11 11],[-1.4 1.4], 'b--'); % SFD 2
grid on;
legend('','Rotor Axis','','Bearing','Disk','Location','best')
end
hold off
xlabel('Nodes (Bearings =1,8 Compressor= 5, Turbine = 11)');
end
end

```

```

figure(); % Create new figure window

if sim_type == 0
    % Open Loop
    if slope == 0
        x_var_s = t_s; x_var_l = t_l; xlabel = 'seconds';
    else
        x_var_s = rpm_s; x_var_l = rpm_l; xlabel = 'RPM';
    end

    forces_s = {F1_s, F8_s}; % short
    forces_l = {F1_l, F8_l}; % long
    node_labels = {'Journal 1', 'Journal 2'};

    for i = 1:2
        subplot(2,1,i);
        plot(x_var_s, forces_s{i}, 'r', x_var_l, forces_l{i}, 'b', 'LineWidth',
2);
        grid on;
        ylabel('Transmitted Load (N)');
        title(sprintf('Transmitted Load at %s', node_labels{i}));
        if i == 2
            xlabel(xlab);
        end
        legend('Short', 'Long');
    end

else
    % Close Loop

```

```

if slope == 0
    x_var = t; xlab = 'seconds';
else
    x_var = rpm; xlab = 'RPM';
end

forces = [F1, F8];
node_labels = {'Journal 1', 'Journal 2'};

for i = 1:2
    subplot(2,1,i);
    plot(x_var, forces(:,i), 'r', 'LineWidth', 2);
    grid on;
    ylabel('Transmitted Load (N)');
    title(sprintf('Transmitted Load at %s', node_labels{i}));
    if i == 2
        xlabel(xlab);
    end
end
end

```

```

% ===== LRV plot =====

% Define multiple target RPMs
target_rpms = [1000 2000 4000 6000 8000 12000];
n_rpms = length(target_rpms);
rpm_tolerance = 30;
cycles = 0.6;
% Node Positions (Normalized to [0 1.6])
N_nodes = 11;
elem_length = 0.16;
z_nodes = (0:N_nodes-1) * elem_length;

if sim_type == 0
    % SD Mode
    figure(1);
    tiledlayout(ceil(n_rpms/2), 2); % Tile Arrangement

    for k = 1:n_rpms
        target_rpm = target_rpms(k);
        idx_rpm_s = find(abs(rpm_s - target_rpm) < rpm_tolerance);
        if isempty(idx_rpm_s)

```

```

        warning('RPM %.0f not found in short simulation data.', target_rpm);
        continue;
    end
    center_idx_s = round(median(idx_rpm_s));
    f_rpm = target_rpm / 60;
    T_cycle = 1 / f_rpm;
    duration = cycles * T_cycle;
    t_start_s = t_s(center_idx_s);
    t_end_s = t_start_s + duration;
    time_mask_s = (t_s >= t_start_s) & (t_s <= t_end_s);
    X_Seg = X_s(time_mask_s, :);
    Y_Seg = Y_s(time_mask_s, :);

    nexttile;
    hold on;
    for i = 1:N_nodes
        Z = z_nodes(i) * ones(size(X_Seg(:,i)));
        plot3(Z, X_Seg(:,i), Y_Seg(:,i), '-', 'LineWidth', 2);
    end
    plot3(z_nodes, zeros(1,N_nodes), zeros(1,N_nodes), 'k--', 'LineWidth', 1.5);
    xlabel('Rotor Axis [m]');
    ylabel('Y displacement [m]');
    zlabel('X displacement [m]');
    title(sprintf('SD LRV at %.0f RPM', target_rpm), 'FontWeight', 'bold');
    grid on;
    % View and axes
    view(45, 25);
    ylim([-1e-3, 1e-3]);
    zlim([-1e-3, 1e-3]);
end

% LD Mode
figure(2);
tiledlayout(ceil(n_rpms/2), 2); % same arrangement

for k = 1:n_rpms
    target_rpm = target_rpms(k);
    idx_rpm_l = find(abs(rpm_l - target_rpm) < rpm_tolerance);
    if isempty(idx_rpm_l)
        warning('RPM %.0f not found in long simulation data.', target_rpm);
        continue;
    end
    center_idx_l = round(median(idx_rpm_l));
    f_rpm = target_rpm / 60;
    T_cycle = 1 / f_rpm;

```

```

duration = cycles * T_cycle;
t_start_l = t_l(center_idx_l);
t_end_l = t_start_l + duration;
time_mask_l = (t_l >= t_start_l) & (t_l <= t_end_l);
X_Seg = X_l(time_mask_l, :);
Y_Seg = Y_l(time_mask_l, :);

nexttile;
hold on;
for i = 1:N_nodes
    Z = z_nodes(i) * ones(size(X_Seg(:,i)));
    plot3(Z, X_Seg(:,i), Y_Seg(:,i), ' - ', 'LineWidth', 2);
end
plot3(z_nodes, zeros(1,N_nodes), zeros(1,N_nodes), 'k--', 'LineWidth', 1.5);
xlabel('Rotor Axis [m]');
ylabel('Y displacement [m]');
zlabel('X displacement [m]');
title(sprintf('LD LRV at %.0f RPM', target_rpm), 'FontWeight', 'bold');
grid on;
% View and axes
view(45, 25);
ylim([-1e-3, 1e-3]);
zlim([-1e-3, 1e-3]);
end
else
    % Close Loop
    figure(2);
    tiledlayout(ceil(n_rpms/2), 2); % same arrangement

    for k = 1:n_rpms
        target_rpm = target_rpms(k);
        idx_rpm = find(abs(out.rpm.Data - target_rpm) < rpm_tolerance);
        if isempty(idx_rpm)
            warning('RPM %.0f not found in long simulation data.', target_rpm);
            continue;
        end
        center_idx = round(median(idx_rpm));
        f_rpm = target_rpm / 60;
        T_cycle = 1 / f_rpm;
        duration = cycles * T_cycle;
        t_start = t(center_idx);
        t_end_l = t_start + duration;
        time_mask = (t >= t_start) & (t <= t_end_l);
        X_Seg = X(time_mask, :);
        Y_Seg = Y(time_mask, :);
    end
end

```

```

nexttile;
hold on;
for i = 1:N_nodes
    Z = z_nodes(i) * ones(size(X_Seg(:,i)));
    plot3(Z, X_Seg(:,i), Y_Seg(:,i), ' - ', 'LineWidth', 2);
end
plot3(z_nodes, zeros(1,N_nodes), zeros(1,N_nodes), 'k--', 'LineWidth', 1.5);
xlabel('Rotor Axis [m]');
ylabel('Y displacement [m]');
zlabel('X displacement [m]');
title(sprintf('LRV at %.0f RPM', target_rpm), 'FontWeight', 'bold');
grid on;
% View and axes
view(45, 25);
ylim([-1e-3, 1e-3]);
zlim([-1e-3, 1e-3]);
end
end

% Current vs Rpm
figure();

if rr == 1
    for i = 1:2
        subplot(2,1,i)
        plot(rpm, current(:,i), 'b', 'LineWidth', 2)
        title(['Closed Loop Servo Valve Current (SFD_{' num2str(i), '})'])
        xlabel('RPM')
        ylabel('Current (mA)')
        grid on
        axis([0 rpm(end) 0 15])
    end
else
    for i = 1:2
        subplot(2,1,i)
        plot(t, current(:,i), 'b', 'LineWidth', 2)
        title(['Closed Loop Servo Valve Current (SFD_{' num2str(i), '})'])
        xlabel('Time (s)')
        ylabel('Current (mA)')
        grid on
    end
end

```